ICE ACCRETION ON SMALL UNMANNED AIRCRAFT

By

Alyssa Shearon Avery

Bachelor of Science in Mechanical and Aerospace
Engineering
Oklahoma State University
Stillwater, OK
2013

Master of Science in Aerospace Engineering
Oklahoma State University
Stillwater, OK
2015

Submitted to the Faculty of the
Graduate College of
Oklahoma State University
in partial fulfillment of
the requirements for
the Degree of
DOCTOR OF PHILOSOPHY
JULY, 2019

ICE ACCRETION ON SMALL UNMANNED AIRCRAFT

Dissertation Approved:

Dr. Jamey Jacob
_____
Dissertation Advisor

Dr. James Kidd
_____

Dr. Brian Elbing
_____

Dr. Alyson Greiner
_____

ACKNOWLEDGMENTS

First and foremost I would like to thank my family. The limit does not exist for your continuous support and encouragement. Also, I have incredible gratitude for the patience of my advisor in the face of never ending questions.

Name: ALYSSA SHEARON AVERY

Date of Degree: JULY, 2019

Title of Study: ICE ACCRETION ON SMALL UNMANNED AIRCRAFT

Major Field: Mechanical and Aerospace Engineering

Aircraft icing is an important and complex problem. Small unmanned aerial systems are becoming increasingly common in high quality operations. The hazards of icing on these smaller aircraft are significant and primarily unexplored. The need for greater understanding of accretion physics at low speeds and low altitudes is obvious when considering the ways in which icing models for manned aircraft are unsuited for small UAS. Cylinder models are incredibly useful in that the stagnation region has the highest amount of geometry change due to ice and has the highest rate of heat transfer. Current numerical tools are not verified under low velocities. The icing model developed is be suited for UAS using analytic methods suited for low velocities and empirically derived heat flux relations. Experimental heat transfer tests were done to support accretion model. Flight testing was used to gather atmospheric data in low altitude icing conditions, gain qualitative data on ice accretion, and to investigate heat flux at the low velocity range.

TABLE OF CONTENTS

LIST OF TABLES

LIST OF FIGURES

xii

CHAPTER 1

Introduction

Aircraft icing is a significant hazard for manned aircraft. Between 1998 and 2009, more than 510 icing accidents were reported. [6] In regions with supercooled large droplet (SLD) conditions, the hazards are more significant. In the more severe cases lift has been shown to decrease 35% and drag increase up to 230%, resulting in severe L/D degradation. [7] As unmanned aircraft begin to fill the roles for many flight needs, the impact of icing on unmanned aircraft (UA) needs to be explored. Balloons (both tethered and untethered) have been the primary tool for studying weather systems. Stationary towers, radar, and manned aircraft are also utilized for weather sensing. Each of these systems have their drawbacks, however. More recently, unmanned aircraft systems (UAS) have been used for weather research in a few different capacities. In this and other roles, UAS and their smaller counterparts, SUAS or small unmanned aircraft systems, are much more likely to encounter icing conditions.

While the icing problem has been considered extensively for manned aircraft, the key physical parameters that define ice accretion are vastly different in the UAS realm. The trajectory of droplets are moving in a significantly lower velocity, the wing is at a smaller scale, and the heat flux properties do not follow the assumptions in established icing models. The need for greater understanding of accretion physics at low speeds and low altitudes is obvious when considering the ways in which icing models for manned aircraft are unsuited for small UAS. Cylinder models are incredibly useful in that the stagnation region has the highest amount of geometry change due to ice and

Figure 1.1: Ice accreted on one of Oklahoma State's UAS on a routine test flight.

has the highest rate of heat transfer.

An example of an unexpected icing event on a small research UA is shown in Figure 1.1. This occurred on a routine flight test at OSU in VFR (visual flight rules) or VMC (visual meteorological conditions) near freezing, but with a low ceiling. SUAS are usually incapable of supporting anti-icing systems and may be required to fly in hazardous icing regions. This presents a straightforward subject for investigation. Ice accretion prediction for UAS scale airfoil and UAS flight conditions. In order to further focus the problem, the icing problem considered here will be limited to the stagnation region.

Numerical tools for icing research are vastly important, simply because of the fact that icing conditions are difficult to reproduce experimentally. Simulation methods contribute to icing knowledge as well as aid in test design and experimental validation. Continuing with the focus of the other methods, the simulation algorithms will generate ice accretion predictions. Icing accretion codes developed at NASA Lewis consider environmental conditions that may be experienced in flight and attempt to predict the growth of ice on aerodynamic surfaces. Current numerical tools are

not verified under low velocities. The icing model developed is be suited for UAS using analytical methods suited for low velocities and empirically derived heat flux relations. Computational fluid dynamics codes have been used moderately in icing studies. However, in most cases these are limited to effects of aircraft performance after ice growth. Accretion codes in which the physics models are able to explored and edited are optimal for this study.

Flight testing was used to gather atmospheric data in low altitude icing conditions, gain qualitative data on ice accretion, and to investigate heat flux at the low velocity range. The sensor suite includes instrumentation that can be easily used for the UAS. This remains along the lines of a variety of systems used to monitor weather and sample the atmosphere. These measurements build atmospheric knowledge and allow for aircraft icing studies.

1.1 Goals and Objectives

1.1.1 Goals

The primary goal of this research is to accurately model ice accretion on a cylinder under expected SUAS conditions. The smaller goals within this statement are identifying SUAS icing conditions and building the accretion model. These goals can be examined within the existing breadth of icing prediction capability. The composition of goals is described in Figure 1.2. The atmospheric condition identification correspond best with forecasting research on winter weather and icing flight test studies. This will take the form of an Observing System Simulation Experiment, OSSE. Model development corresponds with a vast body of knowledge on accretion models, the items on the right in blue. This second goal is responsible for the most complex and significant work done in this study.

The chord length and velocity are both well below what has been seen in past icing studies. The impact of low Reynolds on the icing flow field will be investigated
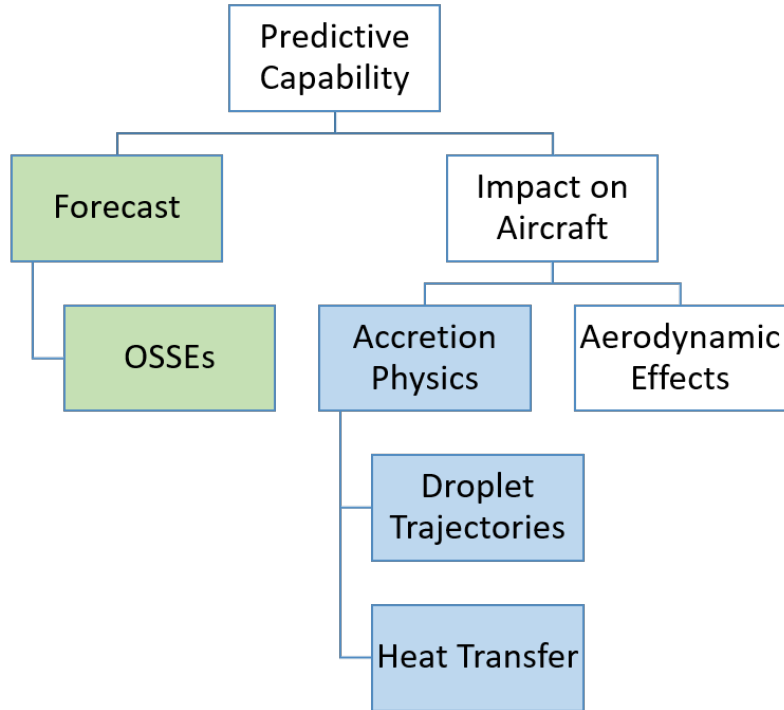
Figure 1.2: Goals identified in the larger spectrum of icing research.

with a range of temperatures, and liquid water content values, especially those that correspond with results from simulations used for forecasting or OSSEs.

1.1.2 Objectives

The first set of objectives contribute to identifying atmospheric conditions. These are: 1)Investigate the use of CM1, an atmospheric numerical model, for icing conditions in weather systems, and 2)Complete a SUAS flight test campaign to get environmental data at times of ice accretion. The main foray into simulating SUAS icing at low altitude will use the parameters of the test vehicle at cruise conditions and the icing times indicated by the CM1 investigation.

The second set of objectives all lead to building an accretion model capable of predicting SUAS icing conditions on a cylinder, Figure 1.3. These are 1)Evaluate NASA's LEWICE model for SUAS parameters with both cylinder and airfoil geome-
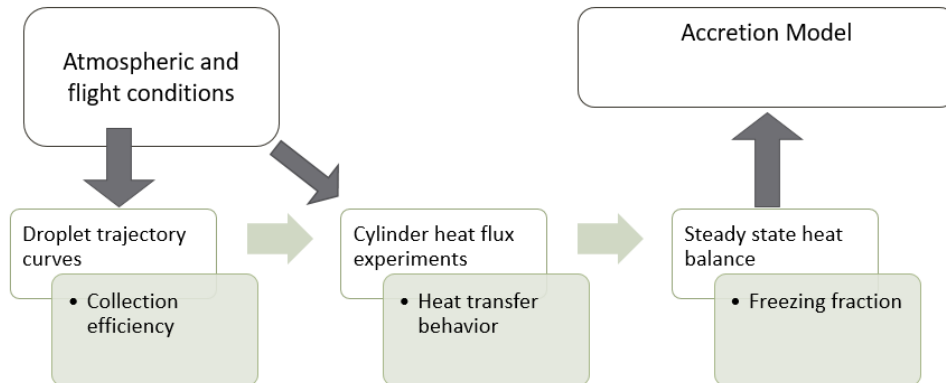
Figure 1.3: Model objectives and logical flow.

try, 2)Model droplet trajectories for low velocities, 3) Experimentally determine cylinder heat flux under the study's parameters, 4) Build accretion model using droplet trajectories, heat flux behavior, and the system's heat balance.

1.2   Outline

This paper will first review the extensive past research on aircraft icing including icing research systems, icing cloud environments, aerodynamic impacts of icing, NASA's LEWICE, cylinder icing models, cylindrical heat transfer studies, and icing flight tests. The analytic and numerical methodology of the cylinder accretion model and CM1 will be explained. Then, the experimental methods are reviewed for the heat transfer experiment and the flight campaign. The next two sections present the results for the experiments and the numerical model. Lastly conclusions will be drawn from behavioral trends and physical realizations, and recommendations will made for future research.

5

center
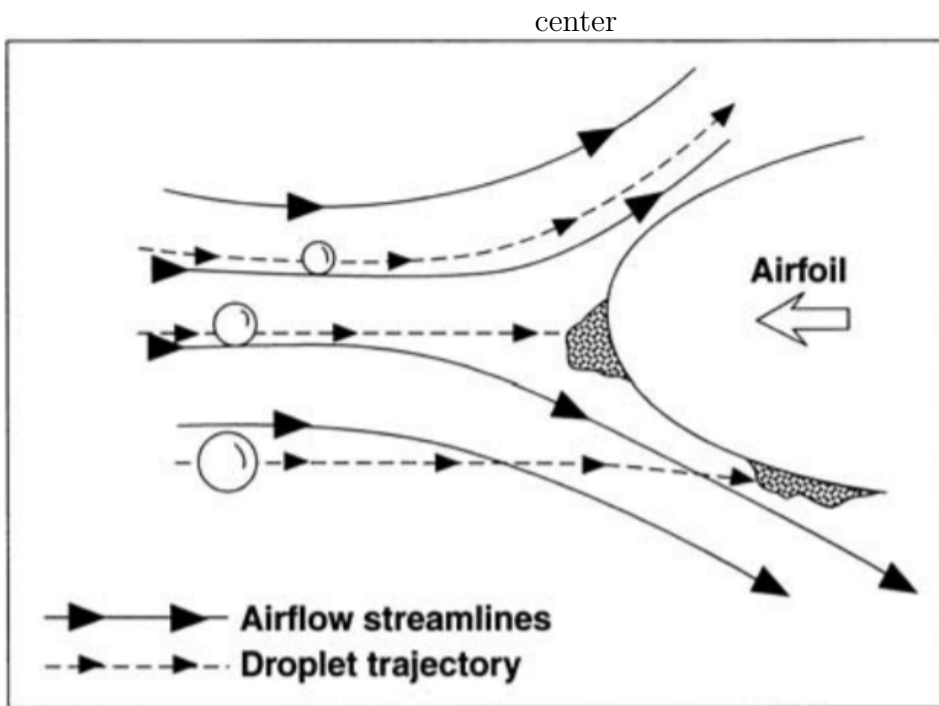
Figure 1.4: T physical phenomena occurring during icing makes it a difficult problem to solve [4]

CHAPTER 2

Previous Work

This literature review first investigates the broad aspects of the icing problem before focusing on the specific research leading to cylinder icing models.

2.1 Icing Cloud Environment

Thunderstorms and their associated weather are one of the most dangerous aviation hazards for aircraft. [11] Regulations currently require aircraft to be capable safe flight in an icing envelope defined in Appendix C of FAR 25. Aircraft must be certified to fly in stratus clouds with droplet diameters up to 40 micrometers and cumulus-type clouds with droplet diameters up to 50 micrometers. Stratus clouds have icing layers only in vertical thickness of 3,000 ft. Lake-effect stratus clouds have high LWC and are most common above the Great Lakes region. Cumulus clouds have horizontally narrow but vertically long icing regions. Figure 2.1 shows a representation of the clouds described.

Thunderstorms are also classified under the cumulus categories and can have extreme icing hazards in the thunderhead anvils. Orographic and wave clouds may have high LWC and can result in icing events with high exposure times. Cirrus clouds at high cold altitudes consist of ice particles but may be dangerous if ice particles melt and refreeze on aerodynamic surfaces.

Generally, the average size of cloud water droplets is 20 micrometers and are small enough to maintain altitude from small air currents. The tops of clouds often have the most LWC and therefore are most likely to incur significant icing. [15] In cloud icing
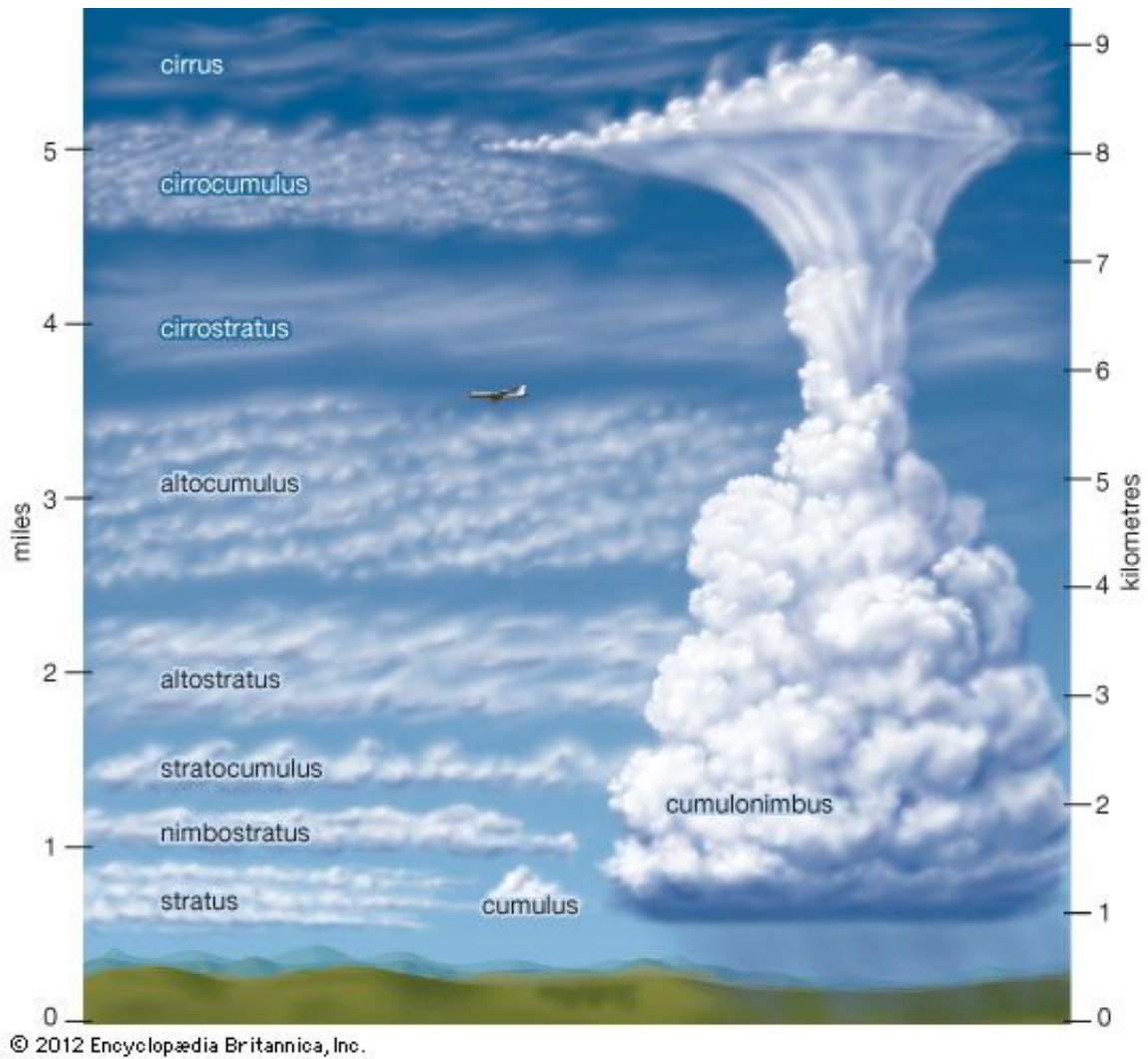
Figure 2.1: Stratus and cumulus cloud forms where stratus forms are on the left and cumulus are represented on the right. [5]

is the common form of aircraft icing though advancing fronts can generate enough moisture to create an icing hazard. Supercooled large drops make up about 5% of the drop found in the atmospheric layer between 10 m and 200 m. For this level of study, it will be assumed that the icing clouds maintain the average droplet size of 20 micrometers.

Accretion characteristics are driven by particle impingement and fluid flow around the airfoil. Two dimensionless parameters, Weber number and Reynolds number, help focus these factors for the chosen environment.

$$We = (\rho_w V^2 l_d)/\sigma \tag{2.1}$$

$$Re = (\rho_a V l_c)/\mu \tag{2.2}$$

Experimental data from past studies will be used to help verify the simulations. The experimental studies chosen have characteristics closest to the range of Weber and Reynolds numbers expected in UAS icing, $0.2(10^6)$- $0.5(10^6)$ and $0.3 (10^6)$- 0 $0.8(10^6)$ respectively.

2.1.1   Icing research systems

Icing forecasts have become increasingly sophisticated in the recent years with cloud microphysics models. These aim to predict the probability of icing occurrences and the resultant icing severity. The forecast icing potential (FIP) algorithm, originally developed by NCAR under the FAA, uses decision trees and fuzzy logic to integrate variables. Most commonly, the primary variable is liquid water content (LWC); other variants of the algorithm use temperature (T) and relative humidity (RH). [6] The models predict icing severity over geographically large areas and icing in levels of severity rather than icing conditions in specific weather systems. An example is shown in Figure 2.2. NCAR's CM1 program is a numerical model that simulates specific

weather systems. This will provide the atmospheric conditions that the aircraft will see in its flight through the system.

A number of systems have been proposed to use both manned and unmanned aircraft for atmospheric measurements.Balloons (both tethered and untethered) have been the primary tool for studying these systems. Stationary towers, radar, and manned aircraft are also utilized for weather sensing. Each of these systems have their drawbacks, however. More recently, UAS have been used for weather research in a few different capacities. The University of Colorado at Boulder has characterized the guidance for a storm penetrating UAS. They used grids of storm data and created guidance profiles and mission profiles to create safe routes for significant data acquisition.

2.1.2 Flight Test Studies

There have been a set of significant icing flight test studies that have been able to gain insight into the conditions that create ice accretion on manned aircraft. The flight test campaigns let by Politovich were able to characterize a range of icing conditions as well as examine for the resultant performance degradation effects [7] [16].

Table 2.1 lists the required atmospheric data and the instrumentation usually found on manned icing research aircraft.[7] Heated wires are often used to derive LWC values. The King probe is a commonly used hot wire for icing and LWC measurements; it maintains a constant temperature and the liquid content is determined from the amount of current needed. Upon investigation of the optical probe, a hot wire LWC sensor may be added to the aircraft's sensor suite.

2.2   Aerodynamic Impact of Icing

There has been a substantial amount of work done in studying the impact of icing on manned aircraft. As icing accumulates on a wing, the airfoil shape is altered and the
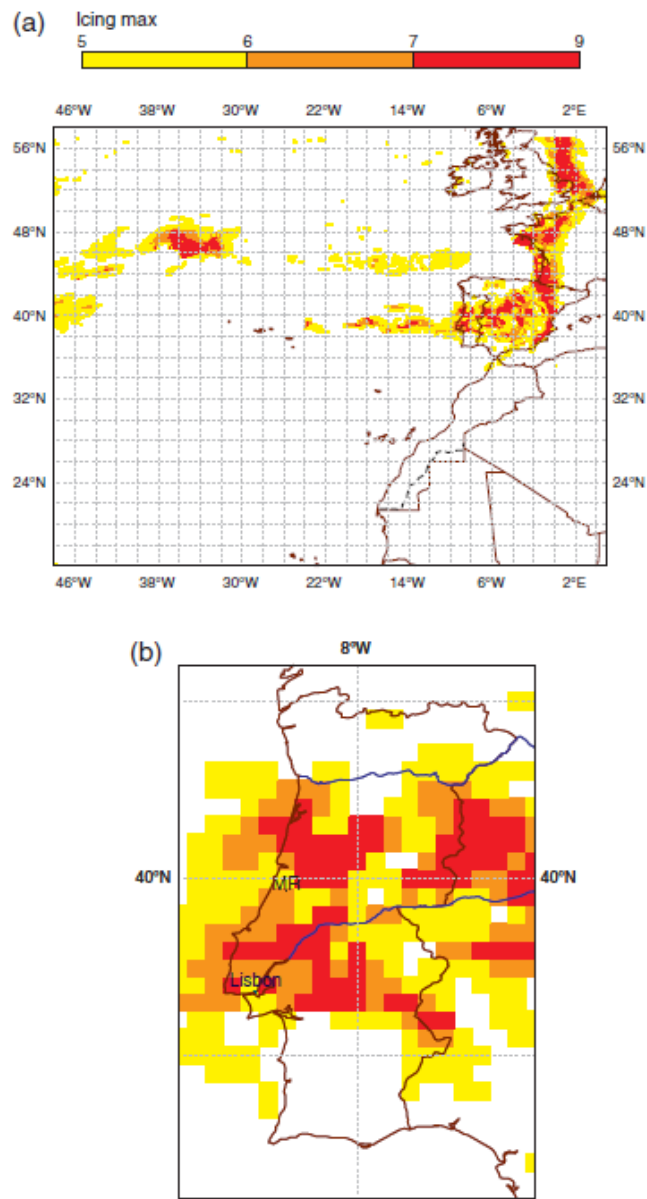
Figure 2.2: Icing severity from a simplified version of the FIP [6].

CLEAR

1915 agg, Plc, Pla, MR   Pla, MR   Pla, MR   Pla   Pla, MR   .05−.50gm^{-3}
700mb −7°C   .10−.30gm^{-3} −7°C agg   −6°C 2005 Pla, Nla, Cle
                                                                              −5°C

2405 ← .05−.20gm^{-3} → ← .15−.30gm^{-3} → 2345   .25−.50gm^{-3}
      −6.5°C water, few irr.   irr, Cle, MR−HR −4.5°C   Cle LR−MR
                                                              water
      .05−.40gm^{-3} .20−.35gm^{-3} large agg
        some ice
         & water   CLEAR
800mb   −2°C   −1°C 2332   0°C
      2420 all water irr, LR−MR 2435   .20−.25gm^{-3} water .20−.30gm^{-3} 2320
      −2.5°C   2440 irr (graupel or water)   .10−.25gm^{-3}
               −1.5°C   .20−.30gm^{-3} .05−.15gm^{-3} 1.5°C 1.5°C
                                                          2°C   2513 2025
                                                              drizzle

900mb | | | | | | | | | | | | | | | |
        200   100   AMA

Distance N of AMA (km)

Figure 2.3: Sketch of an icing flight including atmospheric condition. [7]

Table 2.1: Data Requirements

Data	Standard Sensors
Pressure Altitude	Rosemount pressure sensor
Airspeed	Pitot
Temperature	Reverse-flow temperature probe
Dew Point	Cooled mirror
LWC	Hot Wire or FSSP
MVD	PMS or FSSP
Video of Wing	Camera
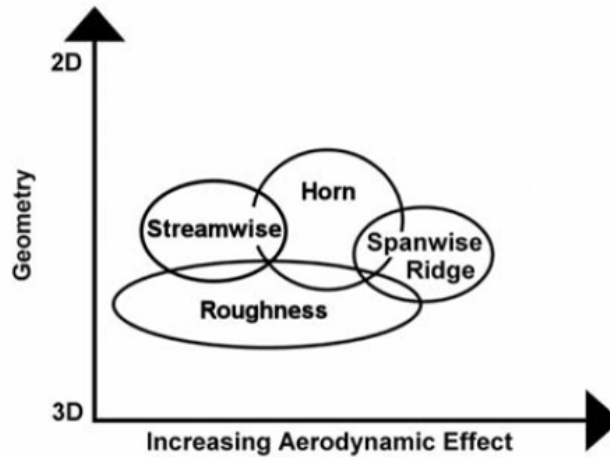
Figure 2.4: Aerodynamic effects for different icing classifications. [2]

aerodynamic properties are changed. Though ice accretion can form in a variety of locations, shapes, and volumes, most may be roughly classified as one of the following categories: roughness ice, horn ice, streamwise ice, and spanwise ridge ice. Each of these classifications has a different geometric pattern and aerodynamic impact. [17] Figure 2.4 provides a map of the geometric footprint and resulting aerodynamic effect and of these various classifications.

Each icing encounter has a unique resultant structure based on exposure time, flight characteristics, and meteorological environment. The classifications attempt to group similar base geometric patterns and formation characteristics. Roughness icing occurs under low exposure times and consists of rough ice coating along the leading edge of the wing without significantly changing the airfoil shape. It may be characterized by height, density, and location on the airfoil. Figure 2.5 shows in example of roughness icing produced in NASA's Icing Research Tunnel (IRT). [8] The rough structure is larger than the local boundary layer and creates separated flow regions. The scale of the roughness elements is such that the flow separation is 3-D and is dependent on each roughness element. The roughness icing group results
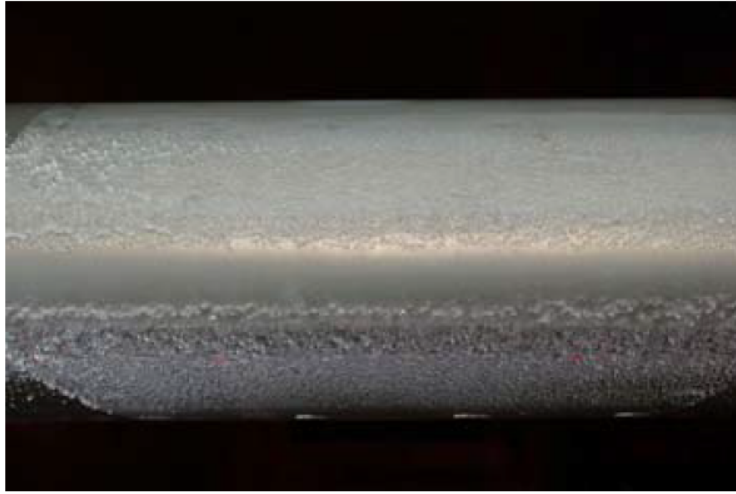
Figure 2.5: Airfoil section with an example of roughness icing. [8]

in increased skin friction and early trailing edge separation.

Horn ice occurs under glaze ice conditions which occurs at temperatures near freezing, high flight velocity, and high water content. [2] This will often will result after roughness icing if the aircraft continues to be exposed to the icing environment. [8] The horn ice accumulates on the upper and lower surfaces of the leading edge and can be characterized by height, location, length, and the angle with respect to chord. Figure 2.6 shows an example of horn ice accumulation. The horn ice changes the airfoil shape severely enough to move the stagnation point onto the ice shape. A large separation bubble forms downstream of the horn. The transitioned turbulent flow usually reattaches to the surface of the airfoil. The separation bubble changes the pressure distribution and results in decreased lift, altered pitching moment and stall characteristics, and significant increase in drag.

Rime ice, an opaque ice that forms at low temperatures and low water content, results in streamwise ice geometry. The accretion volume is usually slight with the ice forming along the contour, though in some large accretion volumes a structure like the horn ice may occur. Streamwise ice has the smallest aerodynamic effect after
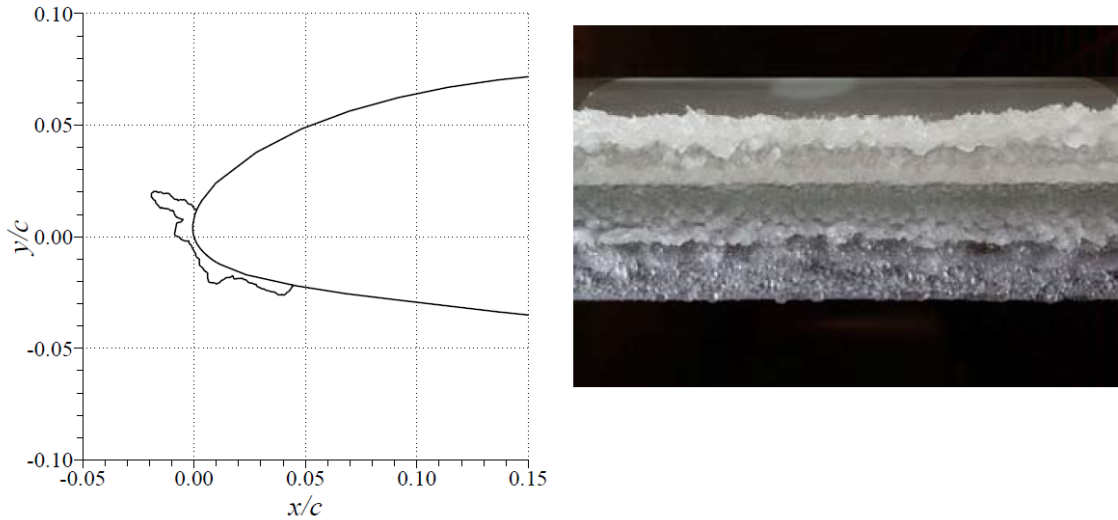
Figure 2.6: Airfoil section with an example of horn icing and the corresponding 2D crosssection. [8]

minor roughness icing cases. Even when horn-like structures occurs, the separation bubbles tend to be much smaller than horn ice. The aerodynamic effects are similar to that of roughness ice. Figure 2.7 shows streamwise ice formed in the IRT.

Spanwise-ridge ice has the most significant aerodynamic effect of the four groups. These tend to occur when de-icing mechanisms cannot cope with large volumes of ice. The structures form downstream of the leading edge, further back than streamwise or horn ice. The ice structure may be characterized by size, location, and geometry. A large separation bubble forms downstream of the ridge as well as an additional bubble upstream of the ridge. The separated flow results in lift degradation, increased drag, and altered stall effects. Fig 2.8 shows icing characteristic of spanwise ridge icing. The leading edge was heated during the accretion run.

Spanwise-ridge icing may occur in icing clouds of all droplet sizes, but is usually associated with SLD icing conditions. As discussed earlier, the dangers of SLD lie in large accretion amounts. The volume tends to be large a result of droplet volume and the relatively high temperatures. Unlike rime icing, the droplets to not freeze on

15
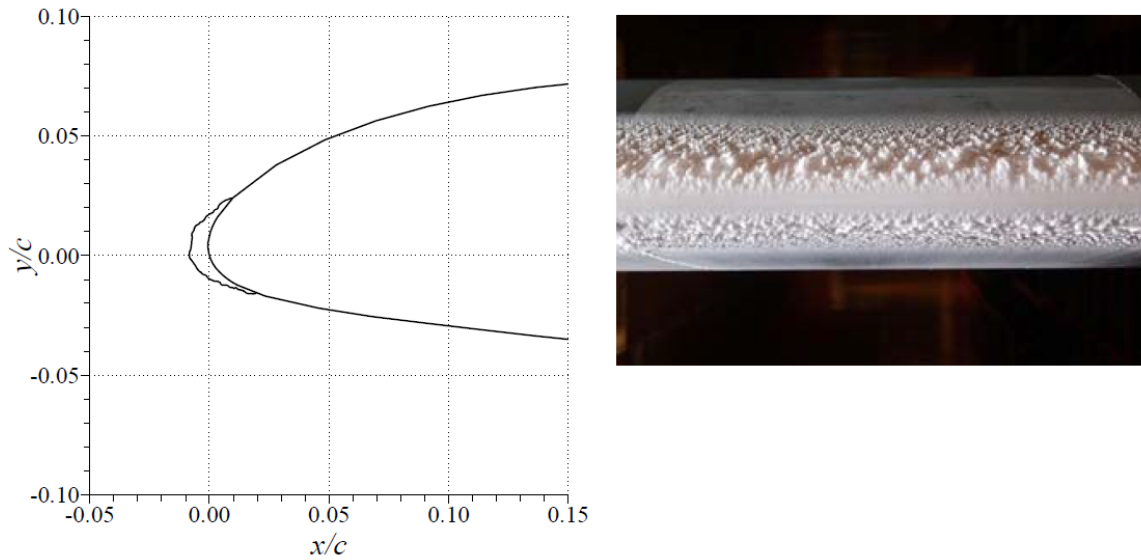
Figure 2.7: Airfoil section with an example of streamwise icing and the corresponding 2D cross section. [8]
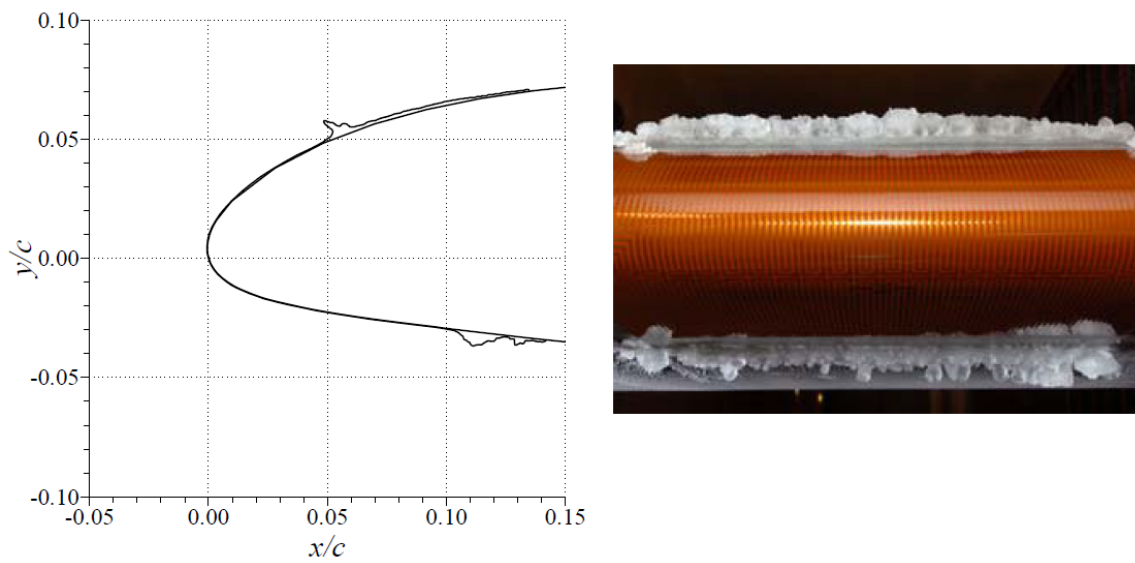
Figure 2.8: Airfoil section with an example of spanwise-ridge icing and the corresponding 2D crosssection. [8]

impact but travel further down the airfoil.

It is not expected the icing structures in this study will fit will into any of these four categories. Though spanwise-ridge icing is known to occur with SLD, it gets its characteristic shape from the presence of de-icing mechanisms. This study will explore the the effects upon platforms without de-icing mechanisms. The structure resultant from streamwise is also improbable since formation comes immediate freezing upon droplet impingement at very cold temperatures. At low exposure times, it is likely that roughness icing will occur. It is the most general of classifications are merely requires that enough ice be on the airfoil to create separated flow areas. It is possible that horn-like structures may occur because of the large accumulation volume and near-freezing temperatures. The make up of an icing cloud associated with glaze icing, however, differs from a SLD cloud. Small diameter droplets at high LWC will have different impingement characteristics from large diameter droplets at moderate LWC. The methods that have been used to characterize the icing geometry will be important in mapping the geometries found in the study and the likely aerodynamic effects.

2.3   Ice Accretion Models

NASA's ice accretion program, LEWICE, is a staple in icing research, is reasonably easy to use, and has a high number of experimental comparisons available in literature. The two-dimensional code calculates the flow field around an aircraft body, droplet impacts, freezing ratios, and ice shapes within a given time. [18] The three-dimensional code, LEWICE3D, uses a three-dimensional fluid flow and trajectory analysis model coupled with a two-dimensional ice growth model. The results of an accretion simulation study comparing LEWICE with another model, ONERA, are shown in Figure 2.9.

NASA has undergone extensive studies for ice accretion with the Lewis Icing

a) horn case (ED0735)   b) streamwise case (ED00730)
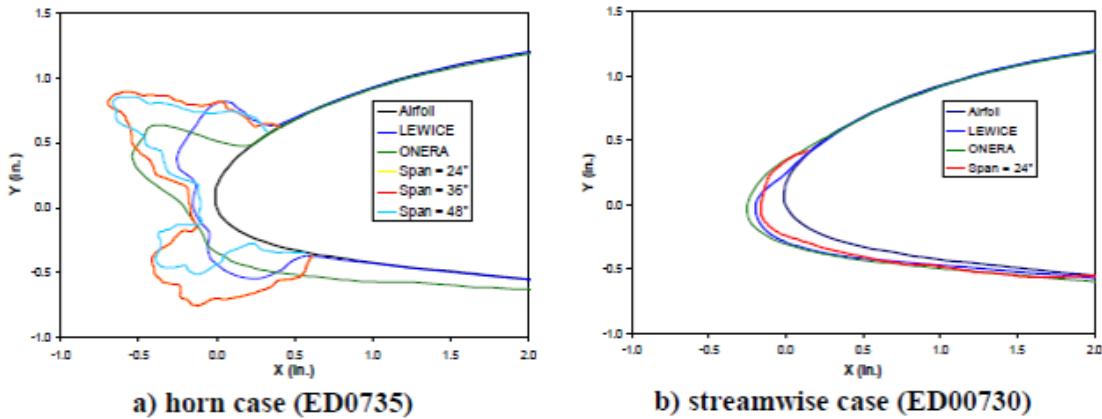
Figure 2.9: Computation simulation results. [2]

Research Tunnel, including studies simulating icing on a general aviation aircraft [1]. This study was chosen because the conditions run for this general aviation study are approaching the type of glaze icing conditions anticipated for UAS icing. In order to gain a greater understanding of accretion behavior simulated with LEWICE, it is compared with tunnel experiments under set conditions. Figure 2.10 shows the results of the simulation at full accretion time compared to the icing tunnel experimental results. Table 2.2 outlines the conditions set for the icing tunnel and used in the LEWICE simulation.

The predicted geometry was able to get the general size of the upper horn and the length of the lower horn. Though the simulation does err in the thickness across the stagnation line, the geometry is impressively close considering the significant flow field complexities with the existing horns. The size and velocity of this study is still more than half of the upper limit of that expected for SUAS.

2.4   Cylinder Accretion Models

"The icing of a cylinder is a unifying theme in icing research because it represents a simple, well-defined icing problem for which a solution can be used to predict icing

18

	Maximum Ice Thickness	
	Upper	Lower
42" Tracing	27.4 mm (1.08")	24.4 mm (0.96")
36" Tracing	25.4 mm (1.00")	22.1 mm (0.87")
30" Tracing	27.7 mm (1.09")	24.4 mm (0.96")
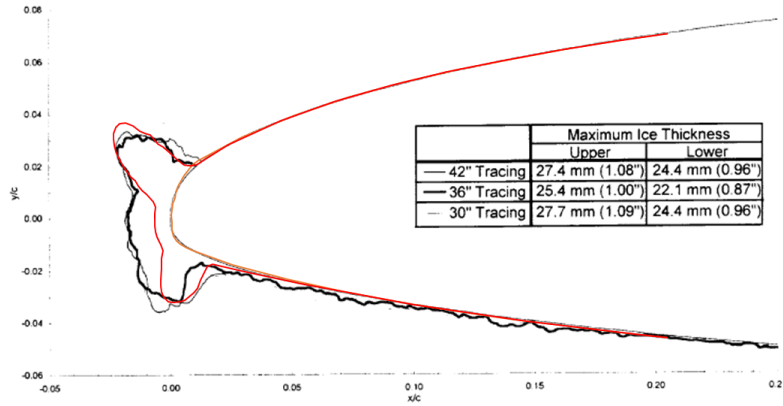
Figure 2.10: LEWICE icing simulation for a general aviation aircraft compared to past experimental study in an icing tunnel. Red line represents the simulation of the final ice accretion.

Table 2.2: General Aviation Experimental Icing Conditions[1]

Static Temperature	268 K
Velocity	66.9 m/s
AOA	0.3 deg
LWC	0.54 g/m3
MVD	20 um
Spray time	22.5 min
Chord	90 cm
We	1,450,000
Re	3,240,000

in more complex situations [19]." Considering cylinder icing allows the base physics to drive the model in the unexplored SUAS regime. A cylinder icing model is built of two main parts, droplet flowfield and the heat balance. The second of which has a wide variety of established approaches and is more likely is present problems at SUAS velocities. Lozowski et. al developed a comprehensive model that discusses but of these components[19].

The work done in the 1940s by Langmuir and Blodgett on droplet trajectories have been repeatedly verified and implemented in icing models [9]. Theoretical curves were generated by a differential analyzer for a range of conditions. The trajectory calculation is based on deviations from Stokes Law, which means that there should be no decrease in accuracy because of low velocity. The analyzer assumes that the droplet field consists of droplets of uniform size. Atmospheric parameters, flight velocity, and cylinder size are used to calculate Reynolds number, drag coefficient, and K, a non-dimensional coefficient developed by Langmuir et al. [9]. These are used to calculate collection efficiency at the stagnation line B_0, total efficiency E_m, and maximum collection angle θ_M. Figure 3.3 shows the curves generated for stagnation line collection efficiency, a value immediately useful for characterizing the accretion at a certain set of parameters. This work also describes geometric relations which may be used to expand of the values for the differential analyzer. This will be further discussed in the Numerical Methodology section.

Hansman et al. in 1992 did an experimental cylinder accretion study. This was done with velocity ranges from 67 m/s to 89 m/s and it horn shapes during wet ice accretion on the 2in cylinder. Additionally it was shown that the wet or glaze ice was most common close to the stagnation point [20]. Another experimental study was done by Lozowski on a smaller cylinder which showed distinctive runback but without clear horn shapes, [3].
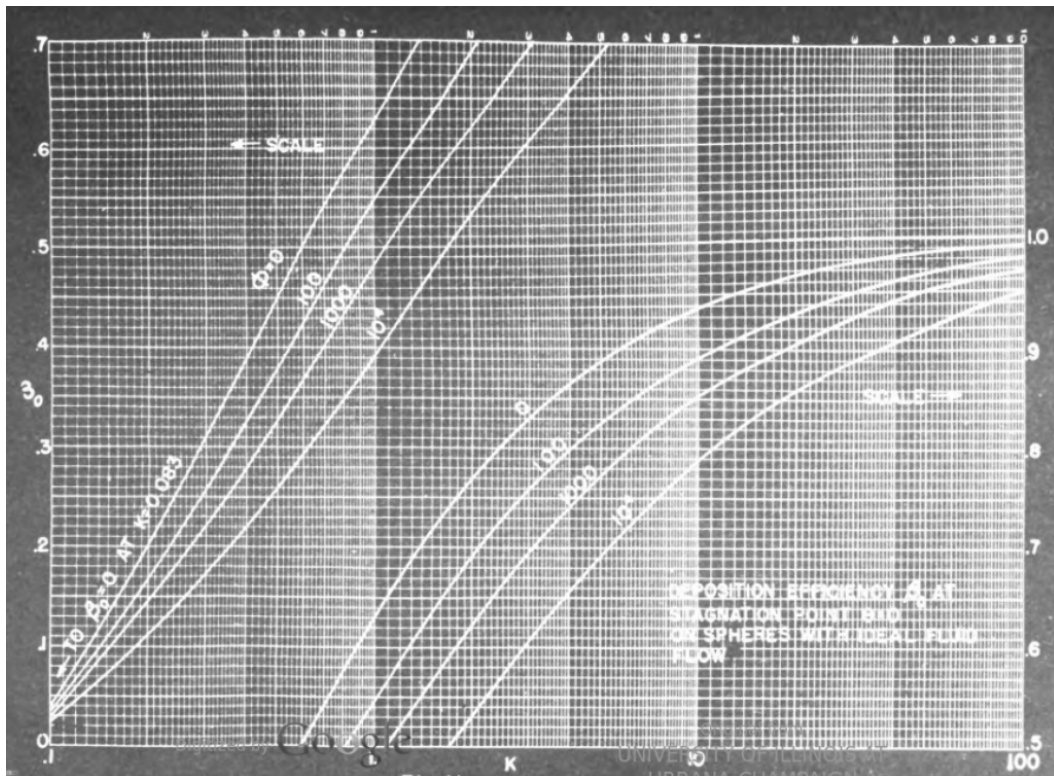
Figure 2.11: Set of curves for stagnation line efficiency generated by the DA used by Langmuir et. al. [9].
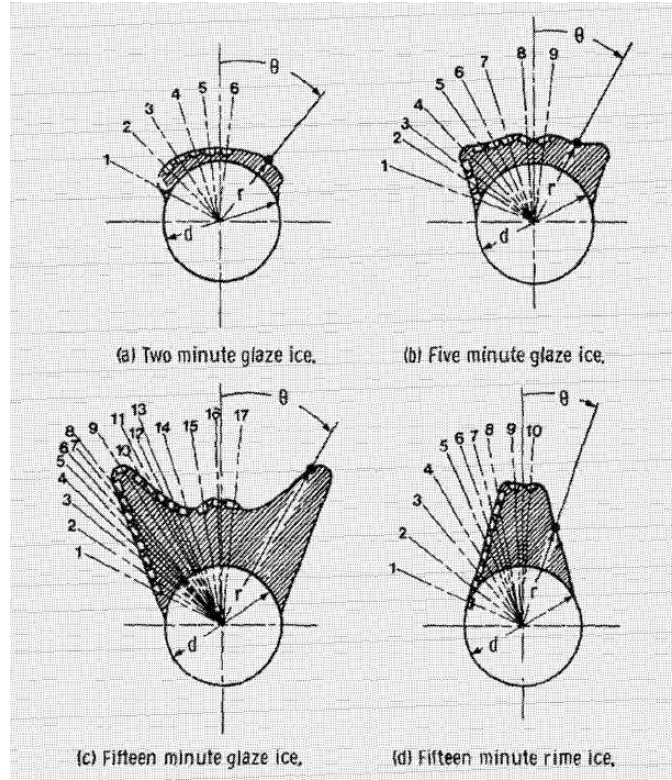
Figure 2.12: The ice accretion shapes used for heat transfer analysis. [10]

2.4.1 Heat Transfer

It is apparent that the icing models are heavily subject to changes with changes in heat transfer distribution. Stagnation region heat transfer with variable roughness is a difficult problem to address. Past experimental studies provide insight into the heat transfer coefficient study presented in this dissertation. Dukhan et al. were able to get consistent results in measuring heat transfer on ice roughened surfaces. As roughness is increased, there is greater heat transfer up to a certain level. Past a certain critical roughness however, heat transfer no longer changes [21]. Van Fossen et al. investigated the heat transfer distribution for a small cylinder in the NASA Lewis Icing Research Tunnel with different ice accretion shapes on the cylinder [10]. The accretion shapes use for the study are shown in Figure 2.12.

The heat transfer distributions for the cylinder and the cylinder with some accre-
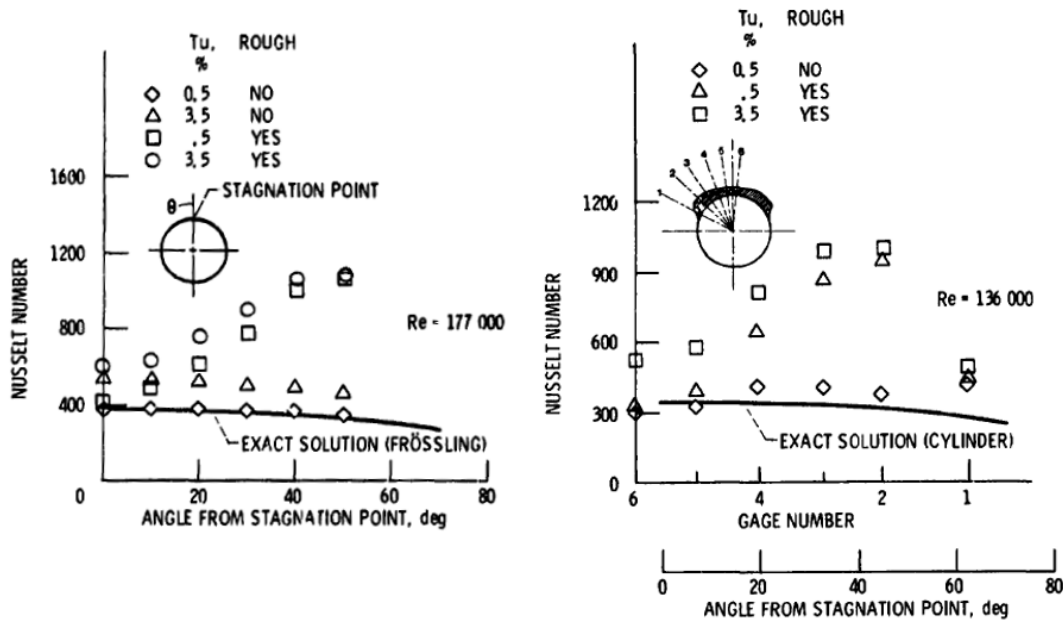
Figure 2.13: The heat transfer distribution results for a plain cylinder and a cylinder with a 2 min ice accretion. [10]

tion. The study found for both cases that with surface roughness the Nusselt number increases with angle past the stagnation point. For both the smooth cylinder and the ice shape without roughness heat transfer decreases slightly past stagnation point following the shape of the exact solution [10].

The specific parameters of the study had too high a Reynolds number and two significant a roughness for the heat transfer coefficients to be directly applicable to UAS. Newton et al. later did a heat transfer study on an airfoil mounted on the top of an aircraft, shown in Figure 2.14 [11]. The heat transfer gauge used for this study is a wing section mounted vertically on the top of the aircraft, in order that the sensor remain in clean airflow. The free stream turbulence in flight (<0.1%) is lower than that experienced in a wind tunnel(around 0.5%) , especially of NASA's icing research tunnel during spray (around 2%).

The heat flux gauges were of the same basic format as in the Fossen test though
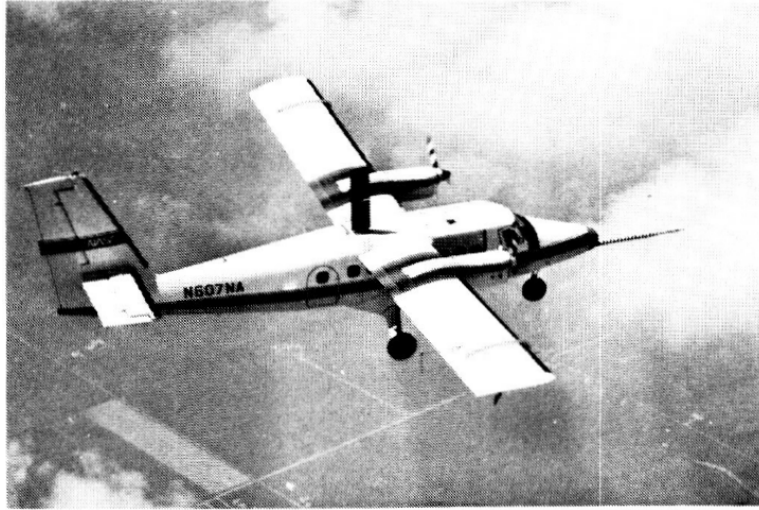
Figure 2.14: Heat transfer gauge as it was mounted on the airframe for heat flux measurements. [11]

distributed across the front of the airfoil. Figure 2.15 shows the cross section of an airfoil used for heat transfer measurements in NASA flight test.

The flight campaign consisted of flights at night to avoid heating from the sun, with different configurations of roughness. Figures 2.16 through 2.19 show the heat transfer distribution results at a few different roughness patterns. The heat transfer is presented as Frossling number, $Fr = Nu/\sqrt{Re}$, in this case the Reynolds number is a function of airfoil chord.

The results show that the heat transfer is at maximum at the stagnation point as would be expected. The Fossen study however showed that this distribution changes with roughness, this does not show in the Newton results until maximum roughness [10]. Even at high roughness the stagnation region's heat transfer is still dominated at the stagnation point. This could be due to the changes in flow from a cylinder to an airfoil, or simply a difference in the quantity of sensors in the stagnation region of the airfoil. In Achenbach's work, local heat transfer results on a cylinder were able to be be fit into functional relationships dependent on Reynolds number and
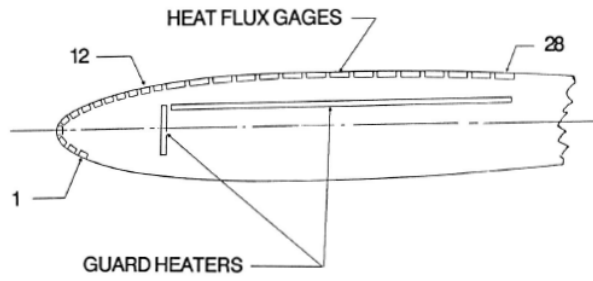
Figure 2.15: Layout of heat flux gauges inlaid into a NACA-0012 in the Newton study [11].
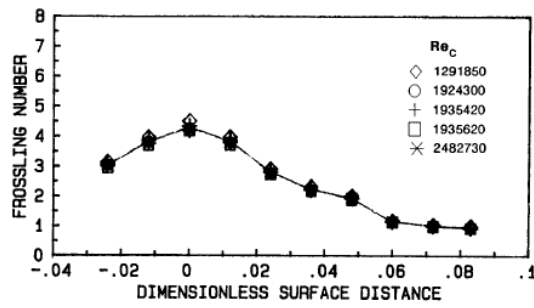
Figure 2.16: Heat transfer distribution for the smooth wing section at zero angle of attack[11].
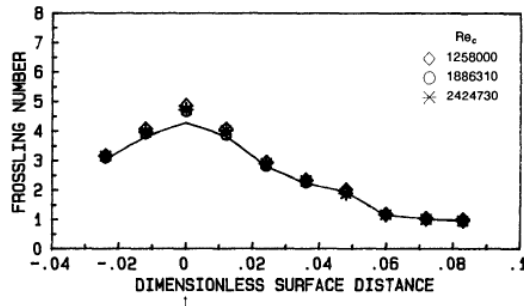
Figure 2.17: Heat transfer distribution for the wing section with leading edge roughness at zero angle of attack[11].
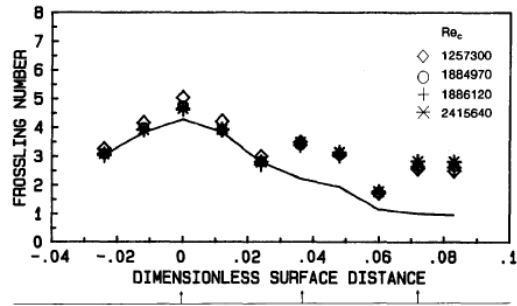
Figure 2.18: Heat transfer distribution for the wing section with sparse roughness at zero angle of attack[11].
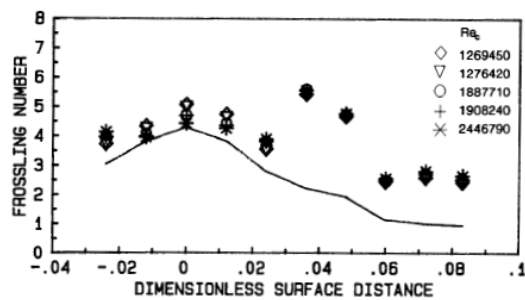
Figure 2.19: Heat transfer distribution for the wing section with dense roughness at zero angle of attack [11].
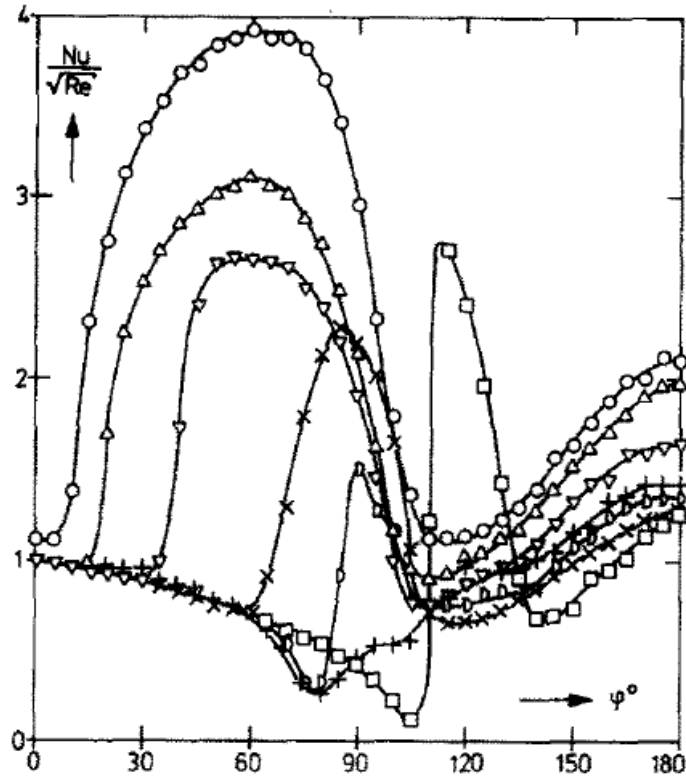
Figure 2.20: Heat transfer distributions at different Reynolds numbers plotted as a function of angle from stagnation line [10].

roughness [13].The sensor used a more narrow bar that allowed more sesitive angle measurements. Figure 3.1 shows one set of results for a low roughness case. The plot includes distributions for multiple Reynolds numbers with the highest Reynolds number reaching the highest heat transfer and the lower subsequent plots corresponding to lower velocities. Many of these distributions have maximum heat transfer past the stagnation point.

These results make it clear that the heat transfer distribution is heavily dependent on Reynolds number. Once heat transfer coefficient can be expressed as a function of angle from stagnation line, this relationship is can then be used in the steady state heat balance of the icing model. There are a few ways to approach modeling the heat balance, the most common being the one-dimensional equilibrium energy balance of
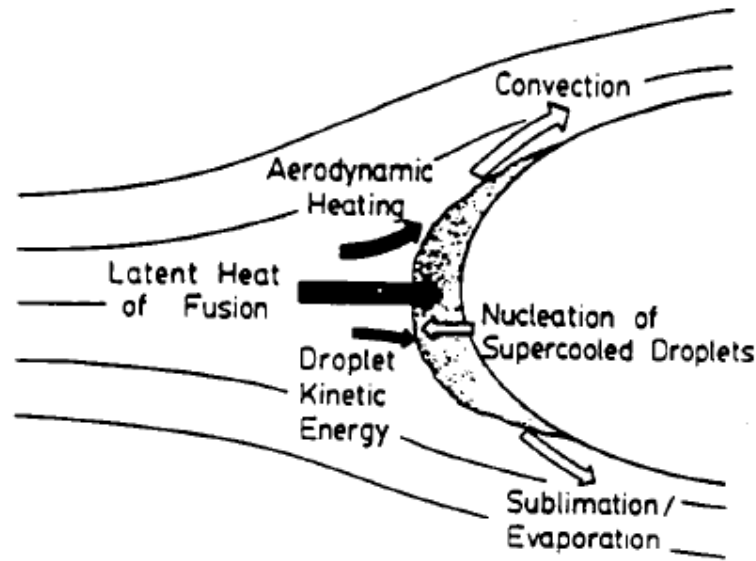
Figure 2.21: Diagram describing the heat transfer control volume [12].

the Messinger model [22]. This was designed to describe the conditions of an unheated surface exposed to icing. The governing conditions are described in Figure 2.21.

Since the Messinger model describes the equilibrium state, it is not able to accurately model ice in the transition region between wet and dry ice. There have been some improvements on the Messinger model though each resulted in a significantly more complex process. Myers uses a more complex mathematical model that considers the conduction of the ice layer and water layer separately [22]. Other models look at complex film dynamics at the surface of an airfoil [23] [24] or a flat plate [25]. It has been shown that mixed phase icing is extremely difficult to predict to erosion effects and irregular particle collection. It also common for a distinctive wedge shape to form, more closely resembling rime rather than glace icing [26]. Poots et al. developed a method for modeling glaze ice on power lines from freezing rain [27]. The rather complex heat transfer balance was used and the results suggest that wet ice is able to form even in the absence of significant aerodynamic heating as is present in manned aircraft icing.

CHAPTER 3

Analytical and Numerical Methodology

"The icing of a cylinder is a unifying theme in icing research because it represents a simple, well-defined icing problem for which a solution can be used to predict icing in more complex situations [19]." Along this theme, cylinder icing will be considered for the low velocity, small airfoil, low altitude conditions expected for UAS. A numerical model and LEWICE simulations will be compared in conjunction with past experimental studies. The fundamentals of LEWICE have been discussed in the previous work section.

3.1   Cylinder Model

In order to further the understanding of the ice accretion at the range of Reynolds numbers, a simple model will be written in MATLab specifically suited to the conditions expected. The framework of the code follows the work done by Lozowski in with the bulk of physical insight from Langmuir and Blodgett and Achenbach [19, 9, 13]. The code will calculate heat flux based on its atmospheric conditions and use empirical equations to get collection efficiency based on the flow's amount of deviation from Stoke's Law in equation below, where C_D is drag coefficient, and Re is Reynolds number.

$$C_D Re/24 = 1. \tag{3.1}$$

A circular cylinder of a prescribed diameter, D_c, is described in five degree increments numbered from the stagnation line through the top of the cylinder, $\theta_i = 5i$,

$i = 0, 1, ..., 18$ with the bottom surface assumed to be symmetric. The code will estimate collection efficiency then heat flux for every sector and from that, icing flux for every sector [19].

With atmospheric conditions (air viscosity, μ_a, and air density,ρ_a), droplet parameters (water density, ρ_s, and droplet diameter, a), and cylinder diameter, D_c, the non dimensional constants droplet Reynolds number,Re_u,, droplet "range", λ_s,, and the proportional inertia of the droplet, K, can be determined. An additional dimensionless parameter ϕ is used to ease the process of data relation.

$$Re_u = 2a\rho_a U/\mu_a \tag{3.2}$$

$$\lambda_s = (2/9)\rho_s a^2 U/\mu_a \tag{3.3}$$

$$K = (2/9)\rho_s a^2 U/(\eta D_c) \tag{3.4}$$

$$\phi = Re_u^2/K \tag{3.5}$$

Langmuir and Blodgett's results' related ϕ and K to ice accretion characteristics with particle trajectory analysis and empirical data [9]. Collection efficiency, β_0, will be determined from one of these groupings of curves plotted as a function of K along the appropriate ϕ line.

That collection efficiency is then converted to a collection efficiency as a function of angle from stagnation line with complex geometric relations and the inertial parameter, K, to become $\beta(\theta_i)$. This will be further discussed in the next section. When compounded with the fraction of total water mass flux, f, the collection efficiency can be characterized per sector. Liquid water mass flux, R_{wi}, is a function of sector collection efficiency and airstream velocity [9].

$$\beta_i = f\beta(\theta_i) \tag{3.6}$$

$$R_{wi} = \beta_i U_w \tag{3.7}$$

The steady state heat balance will be used to solve for freezing fraction and will be applied in each of the angular sections.

$$q_c + q_e + q_v + q_k + q_f + q_f^* + q_w + q_w^* + q_i + q_r = 0 \tag{3.8}$$

The terms in the heat balance are sensible heat flux between accretion and airstream, q_c, evaporative heat flux, q_e, heat flux from aerodynamic heating, q_v, conversion of droplet kinetic energy into heat, q_k, latent heat flux due to freezing water ,q_f, latent heat flux due to freezing water from runback, q_f^*, sensible heat flux between accretion and impinging, q_w, sensible heat flux between accretion and impinging from runback, q_w^*, heat flux between directly impinging water and accretion, q_i, and radiative heat flux between accretion and airstream, q_r. The last two terms will be assumed to be negligible. The heat flux will be applied in each angular section with the two runback terms factoring in the run back from the upstream section before it. Sensible heat flux, q_c, is

$$q_c = h(t_a - t_s) \tag{3.9}$$

where h is the heat transfer coefficient and t_a and t_s are freestream air temperature and accretion surface temperature. Transfer of latent heat due to evaporation or sublimation from surface, q_e, is given by

$$q_e = h(\frac{Pr}{Sc})^{0.63}\frac{\epsilon l_v}{Pc_p}(e_a(t_a) - e_s(t_s)) \tag{3.10}$$

where ϵ is the ratio of molecular weights of water vapor and dry air, P is the static pressure in freestream, c_p is the specific heat capacity of dry air, e_a and e_s are the

31

saturation of vapor pressure of moist air at t_a and t_s, and l_v is the latent heat of vaporization. Aerodynamic heating, q_v, is defined by

$$q_v = \frac{h r_c U^2}{2 c_p} \tag{3.11}$$

where r_c is the local recovery factor and is defined as $r = 0.75 + 0.25 \cos 2\theta t$. Kinetic energy flux, q_k, is

$$q_k = 1/2 R_w U^2 \tag{3.12}$$

where it is assumed that droplets impinge at freestream velocity and all kinetic energy is converted to heat. Latent heat flux due to freezing of impinging water, q_f, is given by

$$q_f = R_w l_{fs} n \tag{3.13}$$

where l_{fs} is latent heat of freezing at t_s and n is the fraction of the accreted mass, $n = 1$ if t_s is less than zero. Sensible heat flux between accretion and impinging, q_w, is defined by

$$q_w = R_w c_w (t_a - t_s) \tag{3.14}$$

where $c_w = 4.27(10^3) \frac{J}{kgK}$. The heat transfer coefficient, h, is a function of θ and is described by the Nusselt number, $Nu(\theta)$, and the thermal conductivity of the airstream, k_a.

$$h = h(\theta) = \frac{k_a}{D_c} Nu(\theta) \tag{3.15}$$

Achenbach's work in '77 is used to find the relationship of Nusselt number to Reynolds number and θ. The heat transfer behavior tends to fit functions within certain ranges of roughness and Reynolds number. For our range of Re, the flow is not
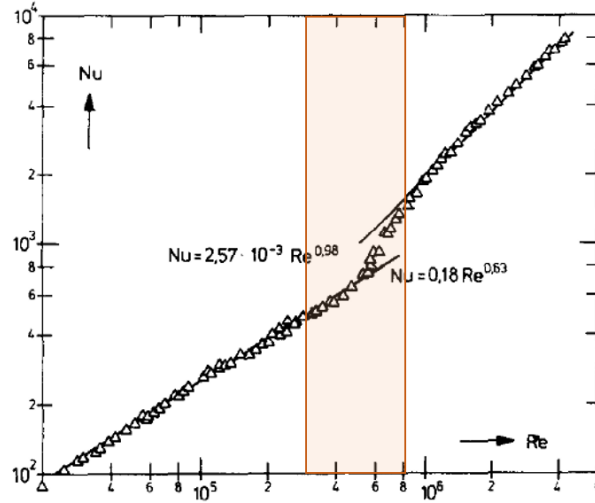
Figure 3.1: Total heat transfer experimental results from Achenbach at the lowest roughness parameter studied in the experiment, $k_s/d = 75x10^{-5}$. The Reynolds number for the SUAS study is highlighted in red. [13]

yet transcritical. For certain roughnesses it does contain the critical unpredictable range of results. Figure 3.1 shows the range at which we are looking on a plot of experimental roughness data [13].

If it assumed that the cylinder for this model has a low roughness, even with some icing, the Nusselt number can be approximated by the pre-critical expression, Equation 3.16. Since Nusselt number is uncertain, experimental testing was undertaken to gage a realistic range of convective heat transfer. Sensors and test plan will be addressed in a later section.

$$Nu(\theta) = Re_c^{0.5}[1 - (\frac{2\theta}{\pi})^3] \tag{3.16}$$

A quick examination of the heat balance at SUAS conditions marks the significant change in dominating parameters. Namely, aerodynamic heating, is significantly reduced, and latent heat removed by freezing in the dominate warming component. Figure 3.2 shows this difference.

33
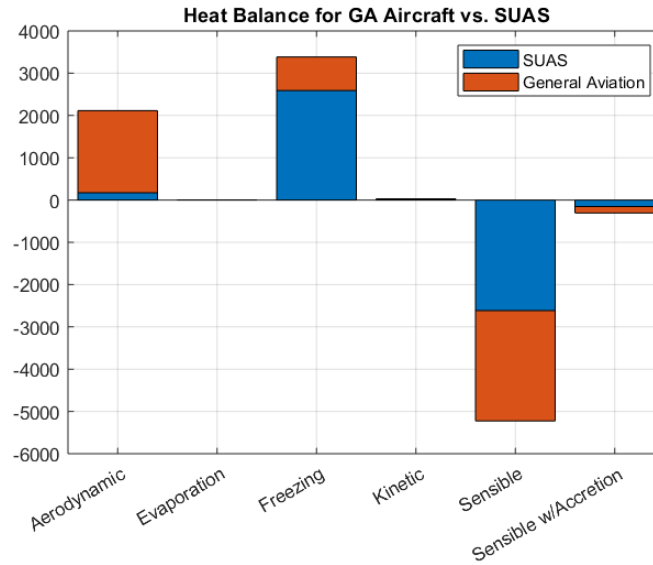
Figure 3.2: Heat balance comparison between an approximation for a general aviation case and a SUAS case.

The heat balance then becomes a nonlinear equation to be solved numerically within each cylinder section. Depending on whether the icing is characterized by wet or dry icing, the heat balance will be solved differently. Dry ice or rime ice occurs when there is no latent heat remaining in heat transfer of the impinging droplets. This simply means there is no melting and no runback in these cases and freezing fraction is one. The heat balance in this case is straightforward and is solved numerically for surface temperature then ice thickness.

$$h(t_a - t_s) + h(\frac{Pr}{Sc})^{0.63}\frac{\epsilon l_v}{Pc_p}(e_a(t_a) - e_s(t_s)) + q_v + q_k + q_f + R_w c_w(t_a - t_s) = 0 \quad (3.17)$$

As discussed in Chapter 2, wet or "glaze" ice is more difficult to model. Because this study is focused on an unexplored velocity range, wet ice will be modeled in a simple heat balance similar to those used by Hansman et al. and Lowzoski et al. [28] [19]. Surface temperature will be assumed to be zero and the heat balance will be solved for freezing fraction. In wet icing there will be melting therefore the runback

34

terms are important and will be replaced in the heat balance. The first section will have no runback as it is the leading edge of the cylinder. The second section has half the runback from section 1 since the other half will run under the cylinder. Sections 3 through 13 will include the runback from the section preceding it.

$$q_c + q_e + q_v + q_k + R_w l_{fs} n + q_w + R_w^* l_{fs} n + q_w^* = 0 \tag{3.18}$$

Icing flux, R_i, and consequently local thickness, th_i, will be calculated after freezing fraction is determined. Ice density is ρ_i and time change, δt, must be small enough that the airflow is not significantly altered [19].

$$R_i = n_i(R_{wi} + R_{wi}^*) = n_i(\beta_i U_w + (\beta_i U_w)^*) \tag{3.19}$$

$$th_i = \frac{2R_i \frac{\delta t}{\rho_I}}{1 + (1 + \frac{4R_i \delta t}{\rho_i D_c})^{0.5}} \tag{3.20}$$

3.1.1 Collection Efficiency

Collection efficiency is a clearly a driving parameter in the heat balance and the local icing thickness. Numerically derived curves for collection efficiency at the stagnation line have been used consistently and reliably for over 50 years. Langmuir et. al also describes a geometric procedure(but does not solve mathematically) to give collection efficiency with respect to angle. This procedure however is complex and other studies chose to derive this functions empirically. Since the velocity range under consideration is largely unstudied, this was not a possibility. Instead the geometric procedure was investigated and solved. The theoretical curves give three values deposition efficiency, the ratio of droplet deposited per unit length at stagnation, $E_{M,}$, collection efficiency, the rate of accumulation at stagnation, $\beta_{0,}$, and the angle at which no more deposition occurs, θ_M. Theorems I and II give the following relations:

$$x_a = sec(\theta_M) \tag{3.21}$$

$$\beta_0 = \frac{x_a + x_b}{x_a + 1} \tag{3.22}$$

$$E = y_0 \tag{3.23}$$

These a give the coordinates to build the geometric apparatus described, this is shown in Figure 3.3. The cylinder diameter is normalized to unity and the values y_0, and γ change with θ. The point x_c describes the center of the grey circle is needed to fully define the system and can be realized by fixing the system at $\theta = \theta_M$, and $y_0 = E_M$.

Once the system is fixed, y_0 can be solved with respect to θ. This requires a series of trigonometric equations. The first two relations are from the law of sines, and the third is a result of the law of cosines. The variables L, φ_1, φ_2, α, and γ are described
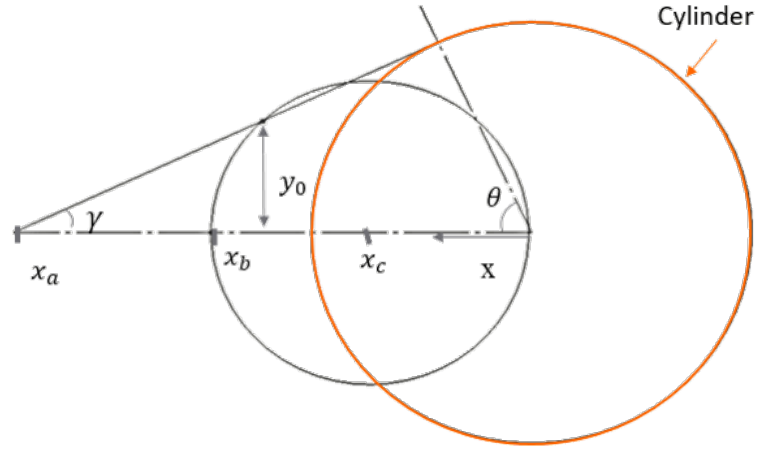
Figure 3.3: System of shapes described by Langmuir et. al, and derived in this study.
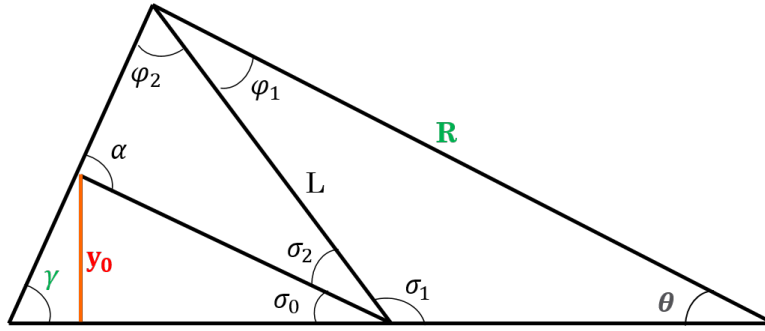
Figure 3.4: Trigonometric relations used to solve for deposition efficiency.

in Figure 3.4.

$$\frac{sin(\theta)}{L} = \frac{\varphi_1}{x_c} \tag{3.24}$$

$$\frac{sin(\alpha)}{L} = \frac{\varphi_2}{x_b - x_c} \tag{3.25}$$

$$L^2 = R^2 + x_c^2 - 2Rx_c cos(\theta) \tag{3.26}$$

$$y_0 = (x_b - x_c)sin(\alpha - \gamma) \tag{3.27}$$

Since deposition efficiency $E = y_0$ and collection efficiency $\beta_0 = dE/d\theta$, collection efficiency can be solved by taking the derivative of the equation $E(\theta)$. For simplification, the equation is broken down into equations 3.28- 3.38 with equation 3.28 serving as the root equation and the following nine equations are components that also vary with θ. These are solved in conjunction with equation 3.28 at every degree θ from stagnation line to θ_M.

$$\beta_0 = \frac{dE}{d\theta} = \frac{dy_0}{d\theta} = (x_b - x_c)cos(\alpha(\theta) - \gamma(\theta))\left(\frac{d\alpha}{d\theta} - \frac{d\gamma}{d\theta}\right) \tag{3.28}$$

$$\alpha(\theta) = sin^{-1}\left(\frac{Lsin(\varphi_1)}{x_b - x_c}\right) \tag{3.29}$$

$$\frac{d\alpha}{d\theta} = \left(1 - \left(\frac{Lsin(\varphi_1)}{x_b - x_c}\right)^2\right)^{\frac{1}{2}}\frac{1}{x_b - x_c}\left(\frac{dL}{d\theta}sin(\varphi_2(\theta)) + Lcos(\varphi_2(\theta))\frac{d\varphi_2(\theta)}{d\theta}\right) \tag{3.30}$$

$$\varphi_1 = sin^{-1}\left(\frac{x_c}{L}sin(\theta)\right) \tag{3.31}$$

$$\frac{d\varphi_1}{d\theta} = \frac{x_c(cos(\theta)L - \frac{dL}{d\theta}sin(\theta))}{L^2}\left(1 - \frac{x_c}{L}sin^2(\theta)\right)^{-\frac{1}{2}} \tag{3.32}$$

$$\varphi_2 = \pi - \gamma - \theta - \varphi_1 \tag{3.33}$$

$$\frac{d\varphi_2}{d\theta} = -\frac{d\gamma}{d\theta} - \frac{d\varphi_1}{d\theta} - 1 \tag{3.34}$$

$$\gamma = tan^{-1}\left(\frac{sin(\theta)}{x_a - cos(\theta)}\right) \tag{3.35}$$

$$\frac{d\gamma}{d\theta} = \frac{sin^2(\theta) + cos(\theta)(x_a - cos(\theta))}{(x_a - cos(\theta))^2}\left(1 + \left(\frac{sin(\theta)}{x_a - cos(\theta)}\right)^2\right) \tag{3.36}$$

38

$$L = \sqrt{R^2 + x_c^2 - 2Rx_c cos(\theta)} \qquad (3.37)$$

$$\frac{dL}{d\theta} = Rx_c sin(\theta) \left(R^2 + x_c^2 - 2Rx_c cos(\theta) \right)^{-\frac{1}{2}} \qquad (3.38)$$

Looking back to Figures 3.3 and 3.4, it is helpful to consider the geometric implications of the equation B_0. As the angle θ changes to cover the area impacted by droplets, the non-dimensional length, y_0, changes also. As smaller angles θ the changes are the largest and the derivative gets very small at large angles. This is consistent with logical thought for how droplets would deposit on a cylinder moving in a uniform field of droplets.

3.2 Numerical Weather Modeling

It is understandably difficult to seek out and study different forms of atmospheric conditions. As such numerical weather modeling is often used to simulate flight conditions. The existing atmospheric icing flight data is for higher altitudes and manned aircraft. Cloud Model 1, CM1, was used to estimate the breadth of icing conditions that may occur in low altitude conditions. WRF is another commonly used numerical prediction software; its physics chart is shown in Figure 3.5. Its uses some atmospheric data as opposed to the purely physics based CM1.

CM1, a three-dimensional, non-hydrostatic, non-linear, time-dependent numerical model designed for idealized studies of atmospheric phenomena was used to generate the data used in the evaluations[29]. The latest available version of CM1 was used – revision 18.3 – for these simulations [29]. Standard cases for a supercell and squall line were utilized to provide data for the OSSEs using the 1/4 circle and 1-km weak-shear case, respectively [30] [31]. Simulations were performed on the Oklahoma State University High Performance Computing Center *Cowboy* supercomputer. Cowboy consists of 252 standard compute nodes, each with dual Intel Xeon E5-2620 Sandy
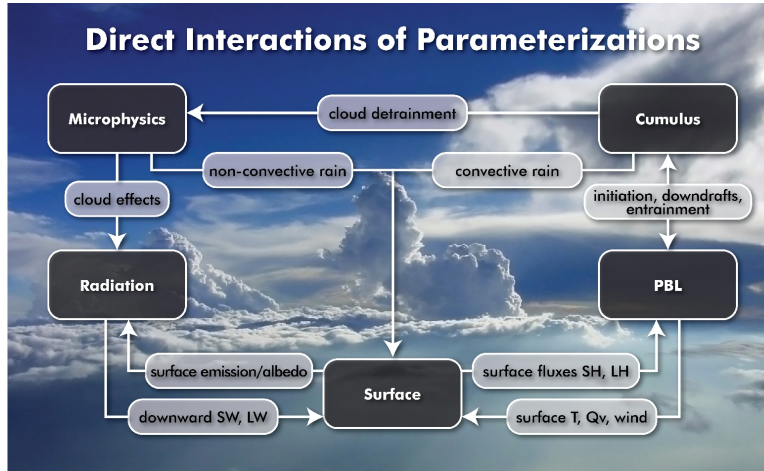
Figure 3.5: WRF process for processing atmospheric data at simulation logic. [14]

Bridge hex core 2.0 GHz CPUs, with 32 GB of 1333 MHz RAM and two fat nodes each with 256 GB RAM and an NVIDIA Tesla C2075 card. Cowboys' aggregate peak speed is 48.8 TFLOPs, with 3048 cores and 8576 GB of RAM. Simulations were run on a single node.

For the supercell simulations, the grid spacing is 1 km in the horizontal and 500-m in the vertical, with resolutions sufficient to resolve storm-scale features, such as the mid-level updraft structure and low-level mesocyclogenesis, but are not generally considered sufficient to accurately represent tornadogenesis. The domain is 120 km by 120 km by 17.5 km, with each simulation extending out through 2 hours. The squall line simulations have a more narrow domain of 300km by 60km by 40km and the same grid spacing. These two sets of simulations were done to explore the effectiveness of using the software for icing conditions and getting an estimation of the breadth of icing conditions that may occur. The complexity of the software itself did not lend to easy alteration for creating winter storms. The standard cases, however, were easy to run and allowed for icing possibility analysis. Icing possibility analysis was performed on a small set of high moisture systems using both supercell and squall line cases.

CM1 can provide an idea of the weather systems that may provide icing conditions

and provide likely parameters in those circumstances. Liquid water content and temperature are the two parameters that determine the possibility of icing. The simulations allow these parameters to be sought within the entire domain of the supercell and squall line simulations. The air temperature must be below zero and there most be water content in the clouds. Most examples of icing occur when the liquid water content is between 0.2 and 1.8 g/m^3). Icing possibility was isolated by identifying locations where the temperature and LWC are both within the desired spectrum. MatLAB was used to analyze the CM1 results. For every location was measured for a positive or negative icing possibility. These results are then summed in horizontal chunks for visual appraisal with a higher result for a higher concentration of positive icing results.

CHAPTER 4

Experimental Methodology

In order to characterize the heat transfer at the flight conditions, wind tunnel tests, and driven ground tests were completed. This consisted of tests focusing on the heat transfer coefficients for a smooth and a low roughness cylinder. Additionally, an icing flight campaign was completed using SUAS. A full characterization of the icing environment was not feasible for the scope of this project. However, lightly instrumented ice accretion flights were used to obtain basic meteorological data and qualitative ice data.

4.1   Heat Transfer Experiment

LEWICE's uses cylinder heat transfer equations for the region close to the stagnation line and flat plate equations away from the stagnation line [11].Thus, it is helpful in the cylinder model and future airfoil accretion model to have a physical understanding of cylinder heat transfer at SUAS conditions. The heat transfer measurements were made on a cylinder comparable to the leading edge of a SUAS wing. The data was used in a set of runs of the cylinder code and could serve as an additional input into the LEWICE simulations. The heat transfer measurements were made by heat flux gauges contained in a cylinder mounted in the free stream.

4.1.1   Heat Flux Gauge

The heat transfer sensor consists of four heat flux gauges placed in the flow side of the cylinder. Figure 4.1 shows the heat transfer sensor with the gauges as they

placed on the cylinder. The body of the sensor was 3D printed out of formlabs rigid resin. It was chosen for its high strength, rigidity, and heat resistance. Each gauge consists of a small copper plate fitted with a thermocouple and a foil heater. In Figure 4.2 the thermocouple and heater positions are shown. The copper pieces are 2.0 in long spanwise, 0.25 in wide in the flow direction, and 0.25 in deep. Figure 4.3 shows the dimension and gauge placement on the cylinder. Each gauge uses a self adhesive, fast response, type E, surface thermocouple. Since the copper had the ability to short the thermocouple, most of the backing remained on the unit except a small area removed so that the thermocouple junction could be placed on the surface of the copper tacked there by the self-adhesive. Each thermocouple and wire was then more firmly fixed to its unit with cement and tape. The set of thin inexpensive polymide flexible foil heaters obtained had a pressure sensitive self-adhesive face used to fasten on the cylinder. Once assembled, the cylinder was stuffed with insulation. The insulation, thermal resistance of the 3D printed material, and the relatively low operating temperature eliminated the need for guard heaters.

For certain tests, some roughening elements were added to the face of the cylinder to achieve a small degree of roughness. A hot glue gun was used to put a pattern of roughness between the copper bars. This was meant to reflect only a small amount of surface roughness as would be contributed by initial stages of icing. Because the dominate geometry is still cylindrical, the test plan and data reduction was not altered for this set of experiments.

The foil heaters used were uncharacterized at the time of purchase. As such, the temperature response under certain voltages and currents were unknown. A variable power supply was used to to gain a rough understanding of the heater requirements before the sensor was assembled. The heaters were attached to their copper plates before testing. Each thermocouple was also tested to be operational with standard DAQ before sensor integration.
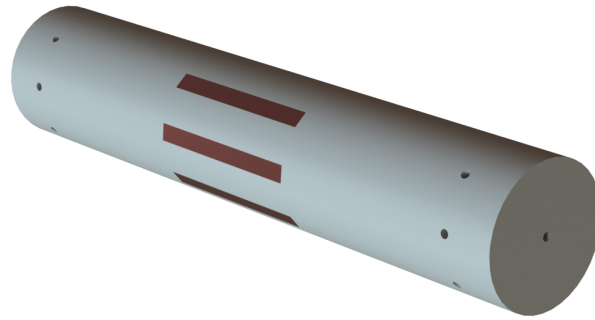
Figure 4.1: Heat flux gauge design from front. Copper plates embedded in the face of the cylinder.
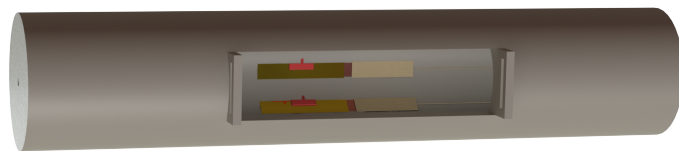
Figure 4.2: Heat flux gauge design from back. Foil heater and thermocouples have been attached to copper plates.
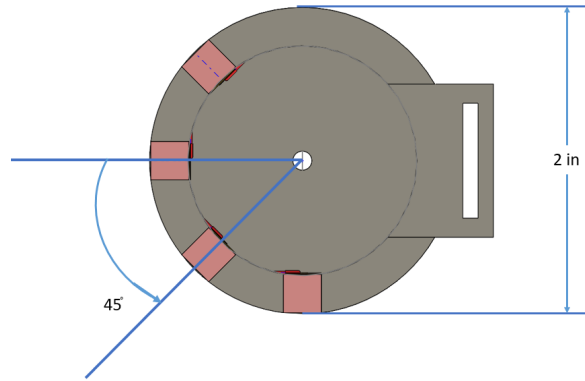
Figure 4.3: Heat flux gauge design center cut view. Cylinder dimension and gauge placement is shown.

Sensor function and data collection was controlled by an ArduinoMega microcomputer. Thermocouple voltages were run through thermocouple amplifiers that communicated directly with the microcontroller. The heaters were operated at a constant voltage and current fixed by a Castle BEC. A solenoid power relay was used to control power input to the heater to maintain constant temperature. The relay has four channels and gauge was controlled separately. The temperature was recorded every second as well as the amount of power added to the system.

The heaters each operated at a slightly different deficiencies. The heaters reached the goal temperature at different rates. However, the heaters were able to maintain the temperature with very little difference in power input both in stagnate flow and low velocities. The ground tests were accomplished by attaching the cylinder to a T-slot aluminum bar held out of a moving vehicle into the free-stream. On the other side of a vehicle was a meteorological ground station which provided air temperature and effective wind direction. The tests were conducted before sunrise to prevent radiative interference.

The bulk of heat transfer experimentation was done with a small, low turbulence wind tunnel. Based on past studies, it is estimated that this wind tunnel has free
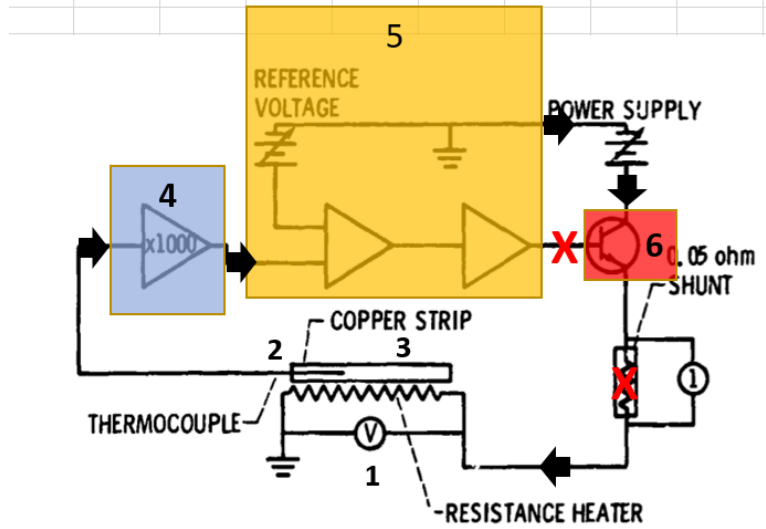
Figure 7. - Schematic of automatic heat flux gage temperature controller.

Figure 4.4: Heat transfer sensor circuit design.[11]

stream turbulence of about 0.5. Figure 4.5 shows the tunnel with the cylinder set up on the inside and Figure 4.6 shows a closer view if the gauge in the tunnel.

4.1.2 Data Reduction

The heaters were run at a consistent power that switched on and off to maintain a temperature of 40 degree C. Electric power, Q_{EI}, is then calculated is a fraction of voltage X current based on the percentage of time that the power is applied at steady state conditions. The local convective heat transfer coefficient is then calculated with equation 4.1, where A is the surface area exposed to the flow and T_w and T_t are the heated wall temperature and total temperature of the flow, respectively. Radiation heat loss, Q_{rad} is estimated by equation 4.2, where σ is the Stefan-Boltzman constant and ϵ is the surface emissivity of the copper bars. The variable Q_{gap} accounts for the glue filled spaces between the heated bars and the more thermally robust material. The equation estimating losses from the gaps use the process outlined by Fossen[10].
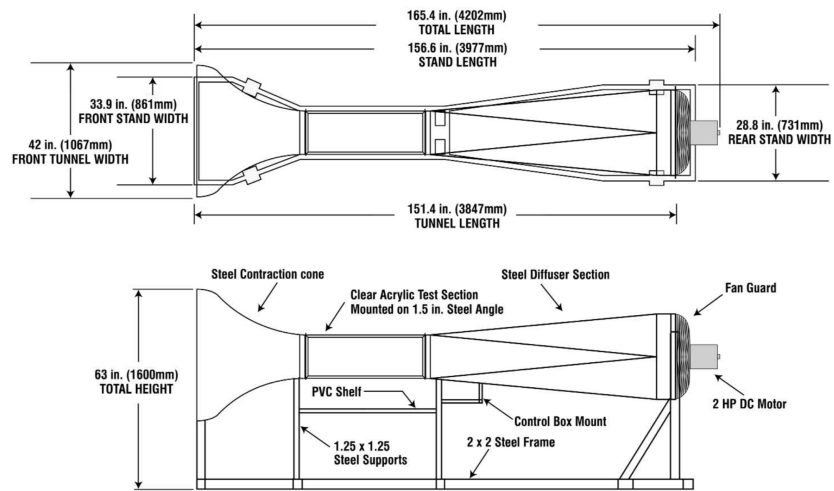
Figure 4.5: Small wind tunnel used to conduct heat transfer experiments.
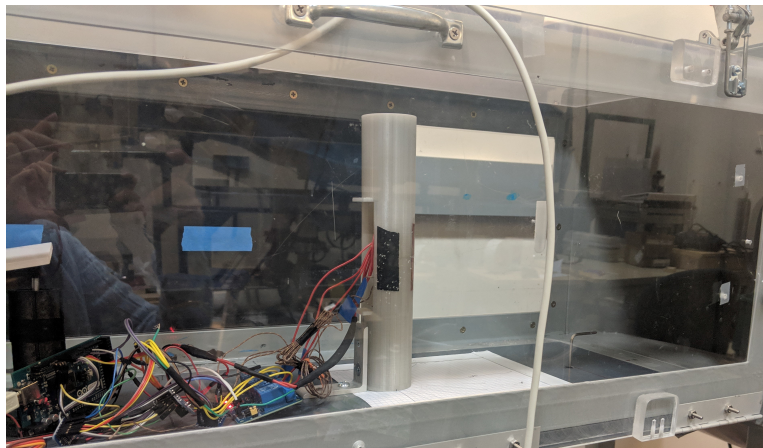
Figure 4.6: Heat flux gauge setup in the wind tunnel.

$$h_{con} = \frac{Q_{EI} - Q_{rad} - Q_{gap}}{A(T_w - T_t)} \qquad (4.1)$$

$$Q_{rad} = \sigma A \epsilon (T_w^4 - T_t^4) \qquad (4.2)$$

4.2 Icing Accretion

Throughout the winter months, the weather was monitored to ascertain the probability of low altitude icing conditions. Since COAs do not allow for in-cloud icing flight, the sensored fixed wing aircraft was flown just below cloud level on cold days will heavy moisture until the aircraft experienced decreased performance or icing conditions diminished. The UAV was not allowed to be flown in a cloud and out of sight. Thus, the conditions were required to include low thin moisture or actual freezing rain. When below freezing temperatures coincided with a chance of precipitation, an icing flight was attempted.

The flight test plan was simple and the flight platform was outfitted with inexpensive instrumentation best capable of mapping the icing cloud. A simple flight profile is shown in Figure 4.7. This flight profile for the sensored aircraft was made to be adaptable to sudden changes in performance or data collection. The Believer, an off-the-shelf foam airframe, was chosen for the icing flights because of its payload capacity and ease of use. Figure 4.8 shows the aircraft in its launch stage.

The sensors flown aim to characterize the icing environment. The data requirements prescribed by the FAA was reviewed earlier and was used to develop the instrumentation list. The sensors on manned aircraft for LWC and MVD are much too large for a small UAS. On the smaller end of the spectrum, the MVD sensor weighs about 20 lbs and the LWC probes are integrated into systems of similar weight. Since options for the MVD sensor both large and expensive, it will not be a part of the flown sensor suite. Instead, a variety of simulations were run, assuming standard
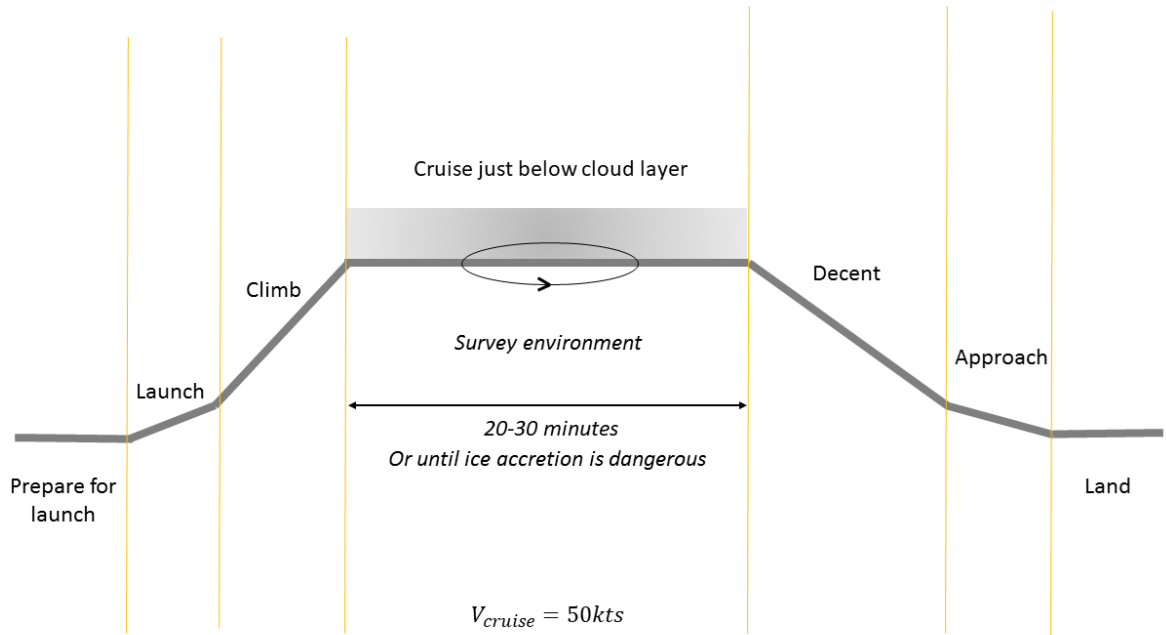
Figure 4.7: UAS ice accretion flight profile.

Figure 4.8: Launch system for the Believer aircraft.

Table 4.1: On-board sensors

Sensor	Data
iMet XF	Temperature, Wing surface temperature, Pressure, Humidity
Dropsonde	Temperature, Pressure, Humidity, GPS
Pitot	Airspeed
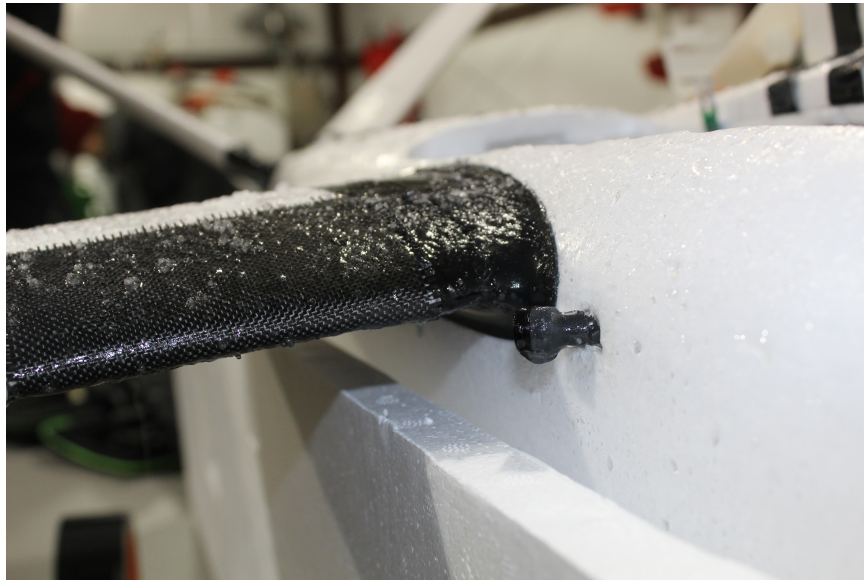
Figure 4.9: IR sensor and wing surface patch

cloud droplet diameter and a set of variable LWC for the conditions ascertained by the on-board sensors, which are listed in Table 4.1.

The iMet XF sensor package includes an IR surface temperature sensor. This was especially valuable to gather data on the temperature differential between the free stream and the wing surface. This data was compared directly to the temperature differential solved when the cylinder model operates in the dry ice growth regime. A piece of composite carbon fiber was expoyed to a small section of the leading edge of the wing, as shown in Figure 4.9. The carbon patch allowed the sensor to track the surface temperature with higher fidelity than the foam surface.

The presence of ice, or lack thereof, on the vehicle under expected icing condi-

tions was an important parameter of information gleaned from the icing flights. Any ice accrued was photographed immediately after landing and the ice thickness was approximated with a ruler on hand. Two icing spray flights were attempted but, as neither resulted in accretion, the details of those attempts will not be presented here.

CHAPTER 5

Experimental Results

The results for the experimental heat transfer investigation and the flight test campaign are presented next because these results are then used in the numerical model. The icing flights give a range for realistic atmospheric values and give a qualitative experimental ice accretion. The heat transfer results will be used in the steady state heat balance in the SUAS ice accretion model.

5.1   Heat Transfer Coefficients

At the time that the wind tunnel tests were run, two of the heat flux gauges were working properly. The cylinder was rotated so that the working gauges saw a variety of angles with respect to the stagnation line. The results here are presented in terms of the Nusselt number, $Nu = \dfrac{hD_c}{k}$. The coefficients for a power law relationship $Nu = ARe^B$ were calculated for at four of the tested angles closest to the stagnation line. Though the magnitude of the Nusselt number change with angle, the shape of function does not significantly alter. Therefore B, the exponent, may be averaged and applied to the heat flux distribution. Past results at a higher range of Reynolds numbers were able to collapse their cylinder results to equation 5.1. The powerlaw relationships in this study suggest that B=0.38 instead of 0.5.

$$Nu(\theta) = Re_c^{0.5}[1 - (\frac{2\theta}{\pi})^3] \tag{5.1}$$

As long as the temperature was maintained around either 1.5 °C above or below 40
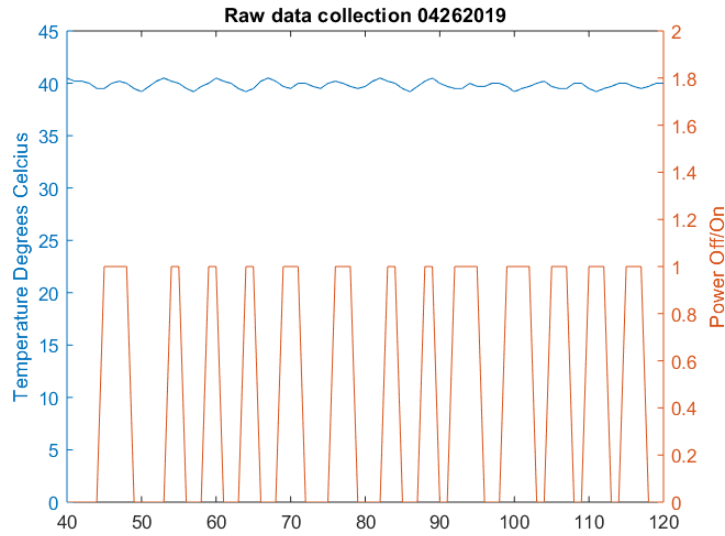
Figure 5.1: Raw temperature and power data sample from wind tunnel testing.

°C, the Q_{EI} value was simply calculated from the power input to the heater. Steady state power patterns were usually reached within 15 seconds of steady velocity. At this point, the tunnel would be run for another 90 seconds and the number of seconds in which power was applied served as a ratio of power. This ratio was then used with the voltage and current to compute final electrical power required. A sample of raw temperature and power data is shown in Figure 5.1.

The heat transfer results closest to the stagnation point were used to gather a power function. A power law fit was done for each angular set of data and while the scalar multiplier 'A' changed with each data set, the power fits converged well both for the cylinder with and without roughness elements. Figure 5.2 shows the plot of the power fit and the corresponding data points.

Figures 5.3 through 5.5 give the heat transfer results for the wind tunnel tests done with no added roughness elements. The gauges have flat surfaces, so the cylinder is not perfectly smooth, but the roughness was very low. The figures also show a plot of the Nusselt number as would be expected for a smooth cylinder but with the powerlaw coefficient adjusted for the results of these tests. The bias error and resulting error

53
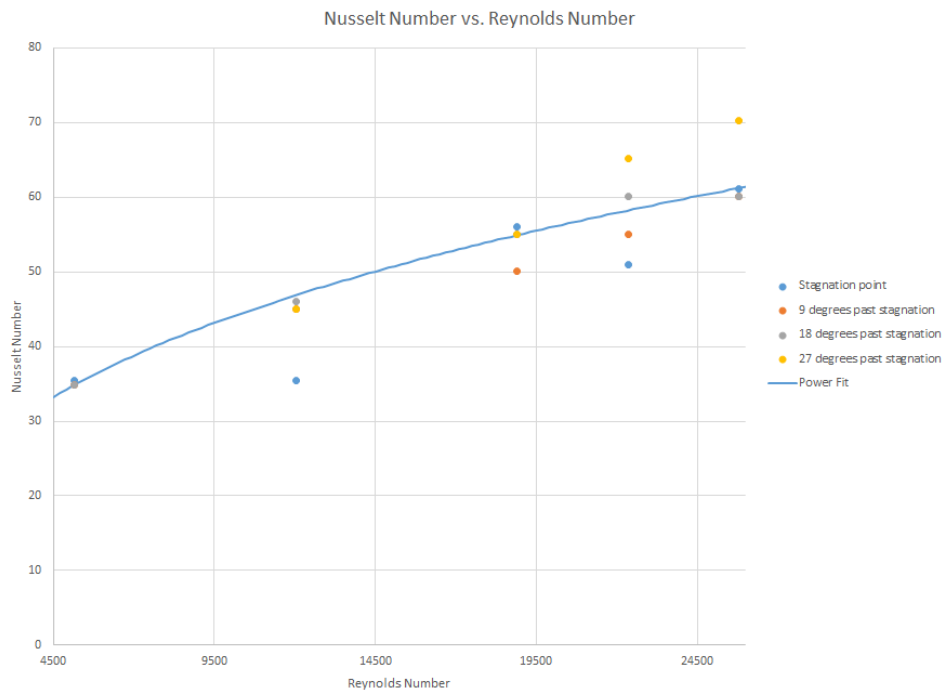
Figure 5.2: Nusselt numbers plotted with respect to Reynolds number, also showing the power fit curve.
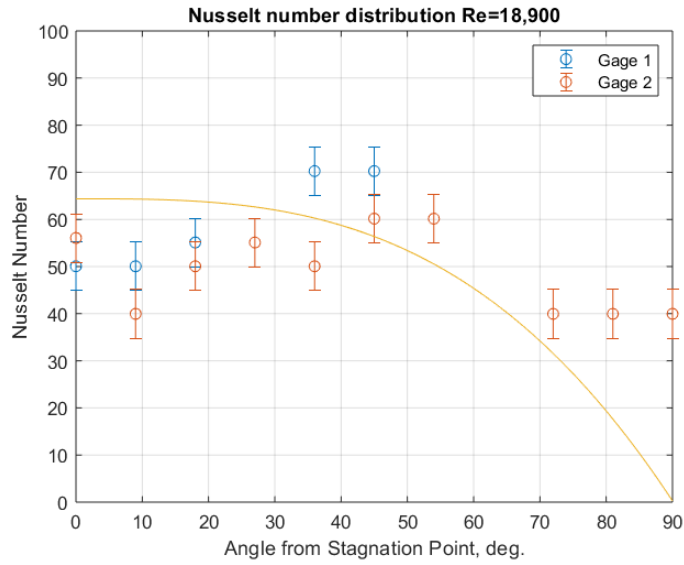
Figure 5.3: Heat transfer distribution for the cylinder with no added roughness elements at 11m/s.

bars were calculated from analyzing sets of data from different days and velocity tests [32]. This consisted of breaking the two minute data sets into 30 second segments and using the fractional differences in power input. The median difference was one power input difference with a maximum of two units for Gauge 1 and three for Gauge 3.

It can be seen from the plots that the heat transfer distribution with respect to angle past stagnation point does not follow the shape expected. The distribution instead follows the behavior from a high roughness test. It must be expressed, however, that the results here are of significantly lower Reynolds numbers than have been studied in the past. Each of the Reynolds numbers show that maximum heat transfer occurs at about 45 degrees and the lowest Nusselt number is within 30 percent of the Nusselt number at the stagnation point. Since these data sets will direct the heat transfer equations used in the model, an attempt was made to fit a function to the data. Following the a trigonometric style fit like equation 5.2, the coefficients were

Figure 5.4: Heat transfer distribution for the cylinder with no added roughness elements at 13m/s.
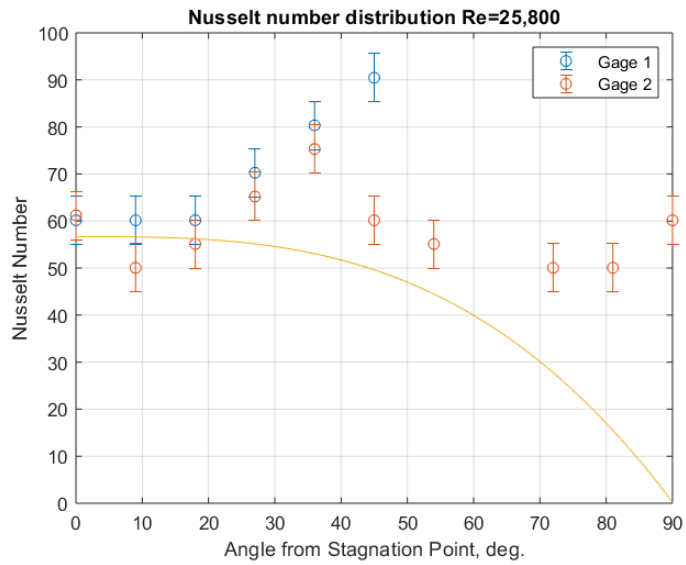
Figure 5.5: Heat transfer distribution for the cylinder with no added roughness elements at 15m/s.
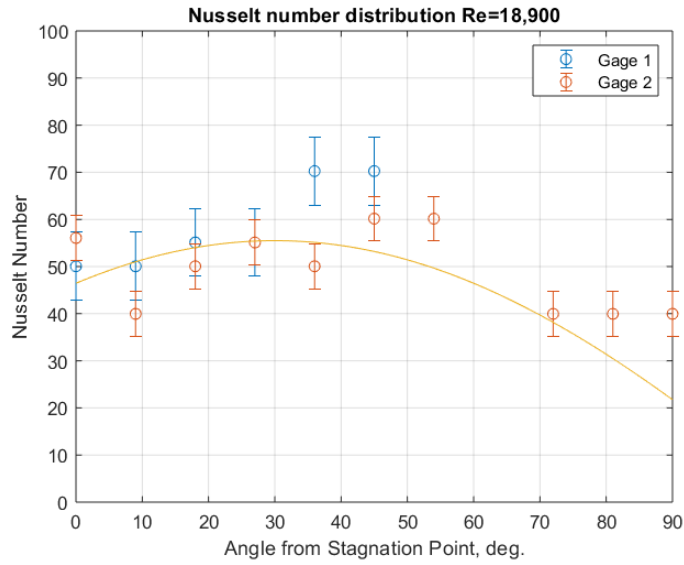
Figure 5.6: Heat transfer distribution for the cylinder with no added roughness elements at 11m/s and the fitted curve.

iterated until the final fit equation of 5.3. Figures 5.6 through 5.8 show the data plotted with this distribution function.

$$Nu(\theta) = ARe_c^{0.38}[B\theta + C] + D \tag{5.2}$$

$$Nu(\theta) = 1.6Re_c^{0.38}[\theta + 60] - 12 \tag{5.3}$$

Figures 5.3 through 5.5 give the heat transfer results for the wind tunnel tests done with the added roughness elements. The power law procedure was repeated for the roughness tests to get B=0.46. Interestingly enough, the distributions here are more consistent with the expected shape of a smooth cylinder.

The maximum heat transfer is past the stagnation point but, the maximum is closer to stagnation line results and the minimum is further from them. At this juncture, an further attempt has not been made to fit the results into a functional form with respect to angle. Instead, the more established equation 5.1 will be used
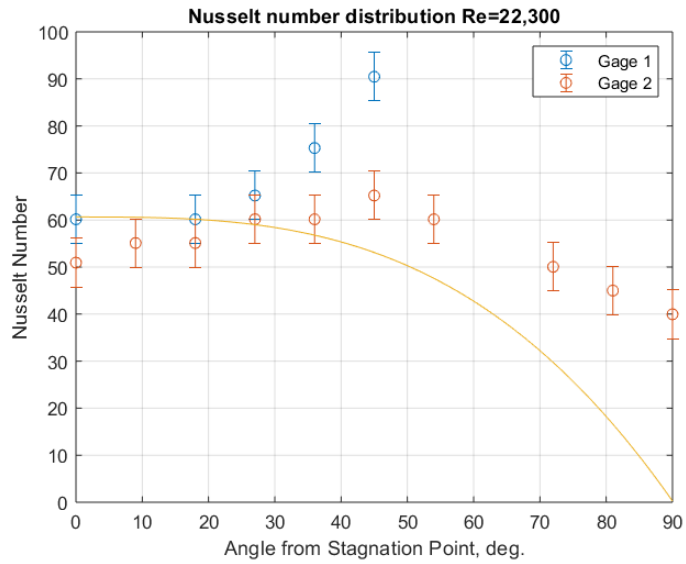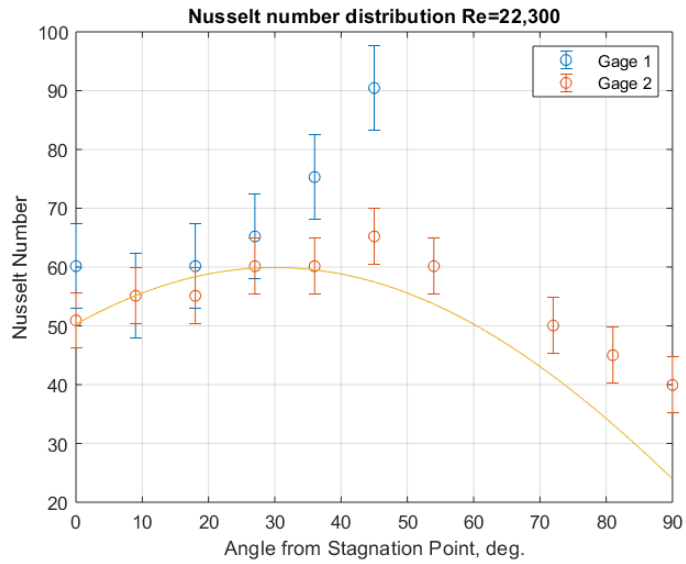
Figure 5.7: Heat transfer distribution for the cylinder with no added roughness elements at 13m/s and the fitted curve.
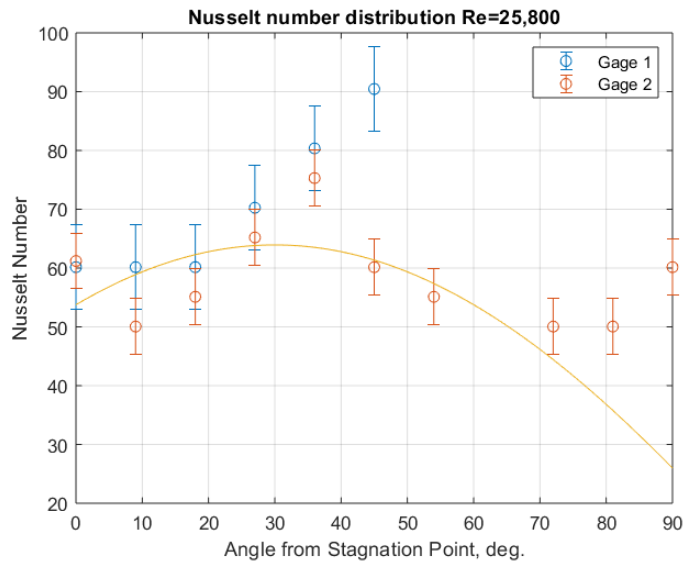
Figure 5.8: Heat transfer distribution for the cylinder with no added roughness elements at 15m/s and the fitted curve.
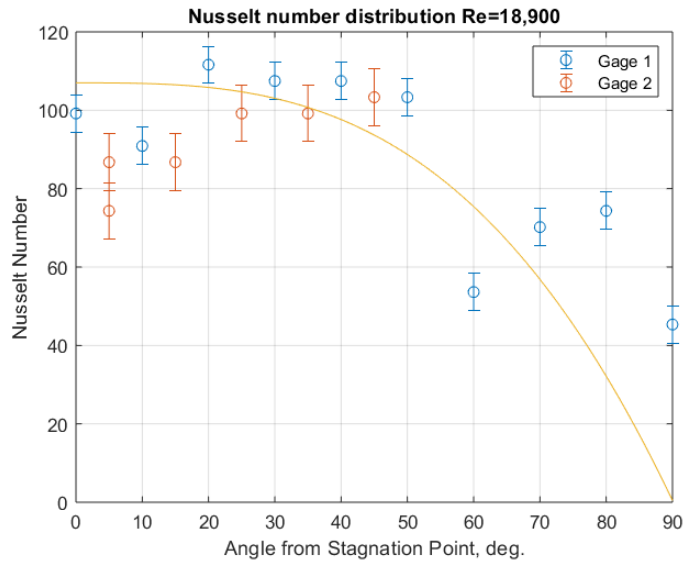
Figure 5.9: Heat transfer distribution for the cylinder with added roughness elements at 11m/s with the adjusted power smooth cylinder distribution.
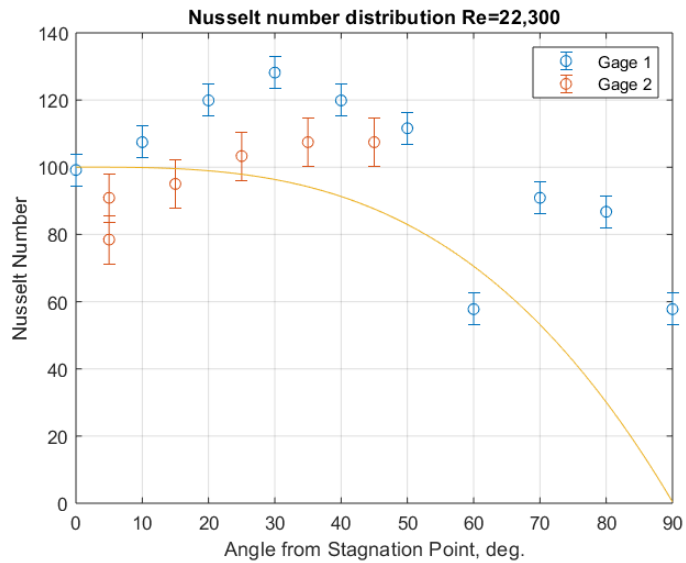
Figure 5.10: Heat transfer distribution for the cylinder with added roughness elements at 13m/s with the adjusted power smooth cylinder distribution.
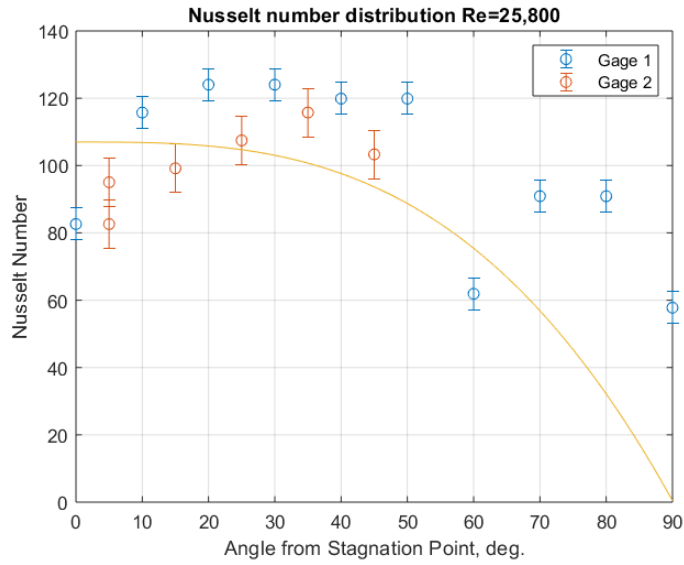
Figure 5.11: Heat transfer distribution for the cylinder with added roughness elements at 15m/s with the adjusted power smooth cylinder distribution.

in the model with the power law adjustment. Figure 5.12 shows the results from the car tests. The buffeting of the cylinder structure does not allow a high level of confidence with respect to the angles presented. There are not enough results to make functional conclusions, but the extended range of velocities tested does enable a level of confidence on projected heat transfer values for SUAS. The results are also within a reasonable extrapolation range from the tests done in the wind tunnel.

5.2 Icing Flights

The goal of the icing flight test campaign was to prove that ice does form on SUAS at low altitude and to characterize the type of atmospheric environment. Because of limited sensors and flight safety considerations at this stage, the accretion amount was too limited for accretion characterization. Instead, the flights were characterized by whether there was an ice presence and basic meteorological parameters. Of the three winter weather flights, two resulted in a positive ice presence. The data for these
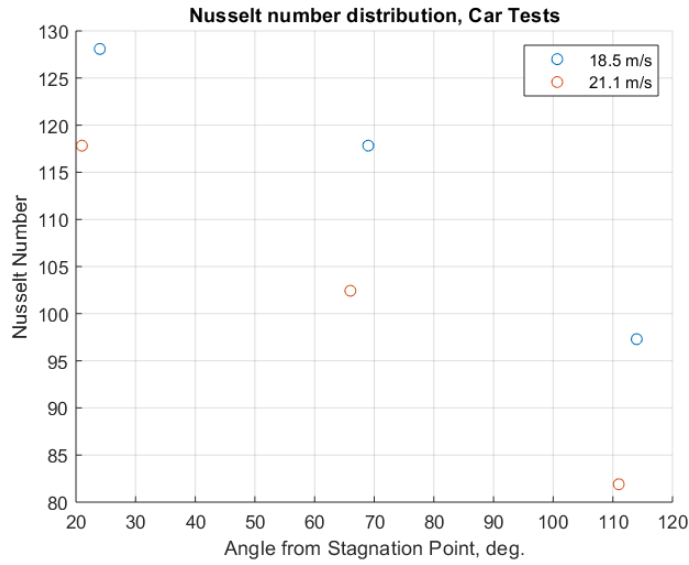
Figure 5.12: Heat transfer distribution for the cylinder during car tests. Error bars are not represented here because of the inconsistency of the test.

three are presented and discussed. Due to a lack of cloud characterization sensors, water content was not able to be ascertained and the moisture content needed for ice accretion is uncertain.

5.2.1 Flight 1: Ice Accretion

The first flight with ice presence occurred with a low altitude freezing fog on January 3, 2019. Figures 5.13 and 5.14 show the ice on the foam airframe flown. Three consecutive flights were executed following the same flight path and only the last one resulted in ice accretion.

The flight paths flown are shown in Figure 5.15 with a color bar representing temperature. The SUAS was flown in a primarily circular ascending pattern. It can be seen that the temperature raises with altitude to a temperature range too warm for icing. Since a high percentage relative humidity is likely to indicate a cloud, it can be assumed from Figure 5.16 that there was a significant moisture both the upper altitude of the flight as well as the lower.

Figure 5.13: Iced wing from first ice accretion flight.

Figure 5.14: Close view of icing on the wing and around the Pitot tube.
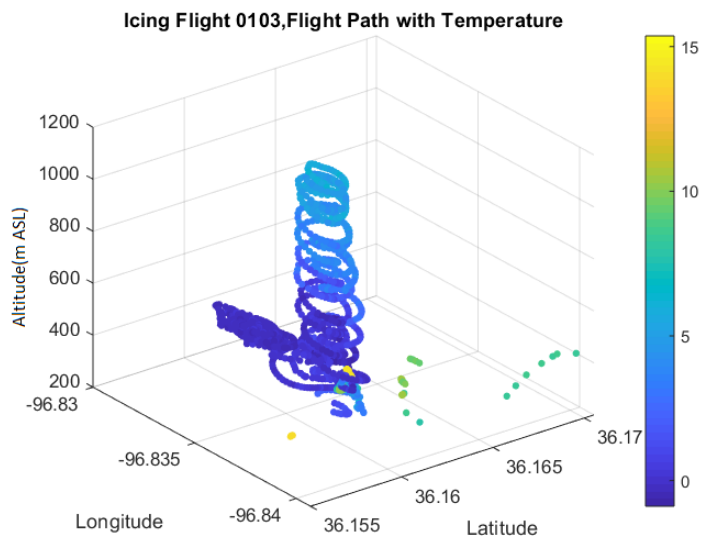
Figure 5.15: Flight path and temperature distribution plot for the Icing Flights 0103.
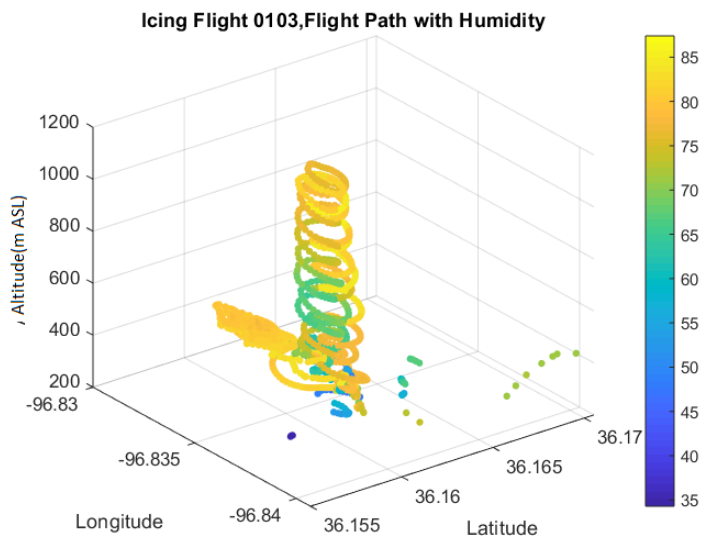
Figure 5.16: Flight path and humidity distribution plot for the Icing Flights 0103.
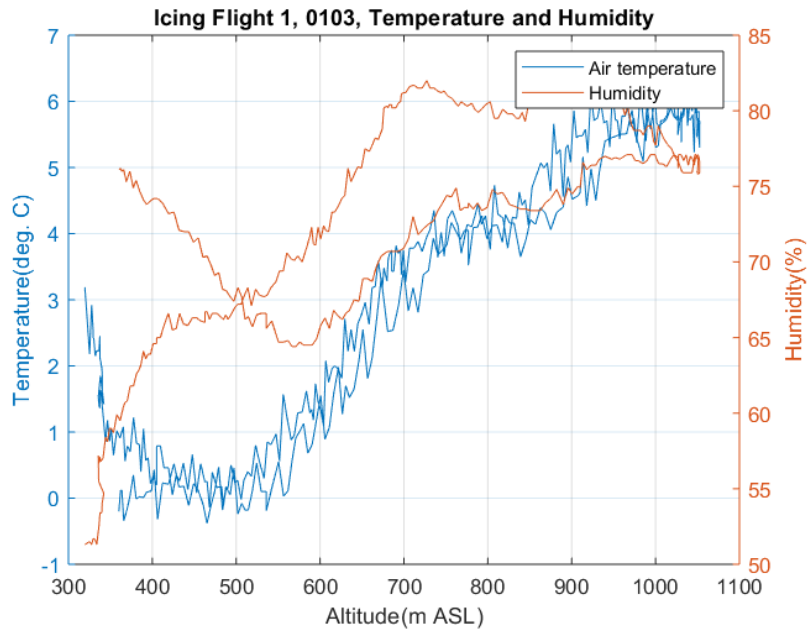
Figure 5.17: Humidity and temperature distribution plot for the first flight.

Figures 5.17, 5.18, and 5.19 show the temperature and humidity of the flights as a function of altitude. The first two show that high humidity did not occur with below zero temperature. In the third flight, the aircraft flew through an area with temperatures just below zero and high moisture. Combining the information from Figure 5.19 and Figure 5.16, it can assumed that the icing look place in the lower altitude moisture mass. This plot corroborates this conclusion by confirming the simultaneous presence of freezing temperature with high humidity at an altitude of 300ft-500ft. The data taken at this time was isolated and there was a temperature range of 0.5 to -0.6 degrees Celsius.

5.2.2 Flight 2: No Accretion

The second winter weather flight did not result in any visible icing. The conditions were significantly colder and there appeared to be visible clouds, the moisture content may have been too low at the low altitude reasonable for SUAS flight. The flight

64
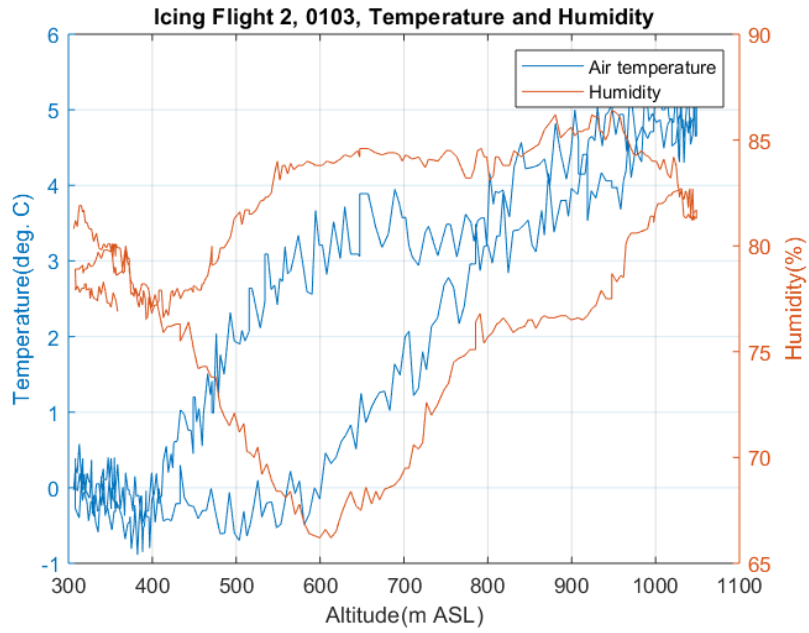
Figure 5.18: Humidity and temperature distribution plot for the second flight.
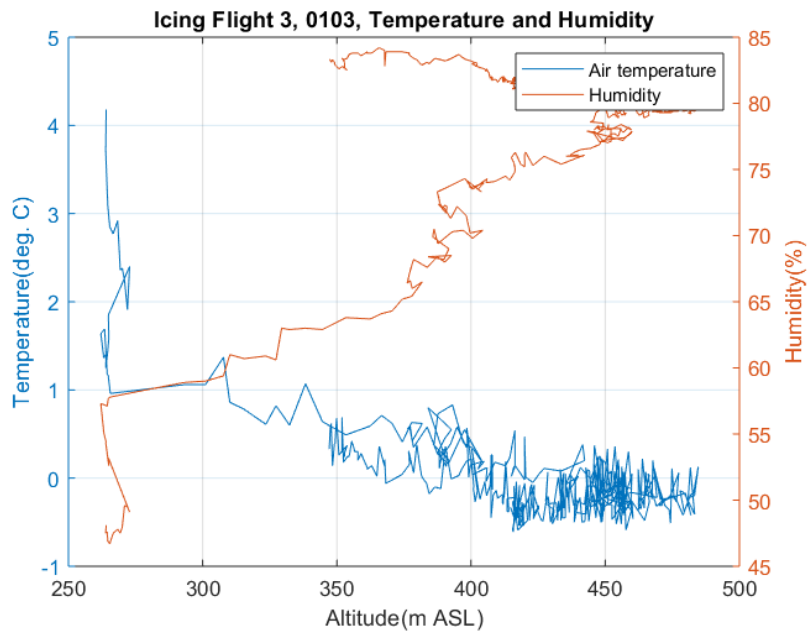
Figure 5.19: Humidity and temperature distribution plot for the first flight.
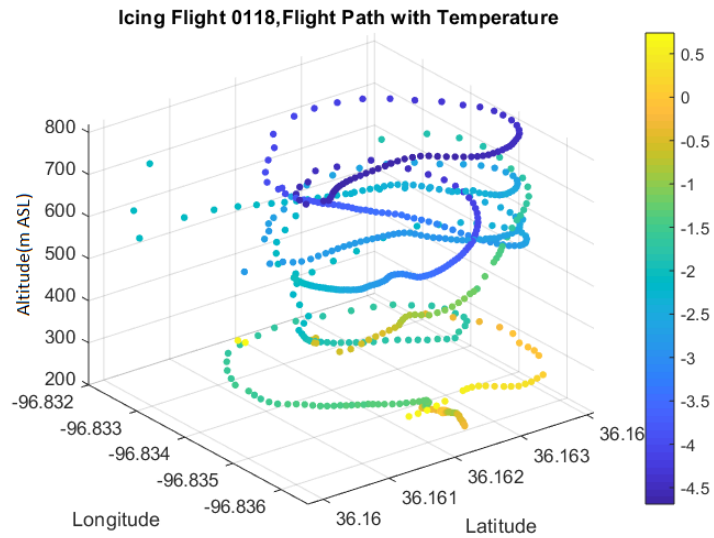
Figure 5.20: Flight path and temperature distribution plot for Icing Flight 2.

path follows the same ascending pattern but was executed at a higher rate because of difficult pilot conditions. The path is shown in Figure 5.20 with the temperature range. The flight was almost in entirely below freezing conditions.

Figure 5.21 shows the distribution of temperature and humidity as a function of altitude. Since the temperature was very favorable, it was only be assumed that the air mass did not contain enough moisture for SUAS icing. The maximum humidity measured hovered around 82 percent, rather than the 85 percent seen during the January 3 flight. Humidity is not a direct indicator of LWC, but the lower humidity levels in this flight did coincide with lack of ice accretion.

5.2.3   Flight 3: Ice Accretion

The third flight in the campaign resulted more significant ice than that of the first. Not only was there an ice presence but, the accretion showed greater thickness at the leading edge and the top of the wing. This is consistent with icing patterns driven by the flow field. In Figure 5.22 the ice layer can be seen on the top side of the wing. Figure 5.23 shows the ice at the leading edge terminate as it reaches the underside of

66
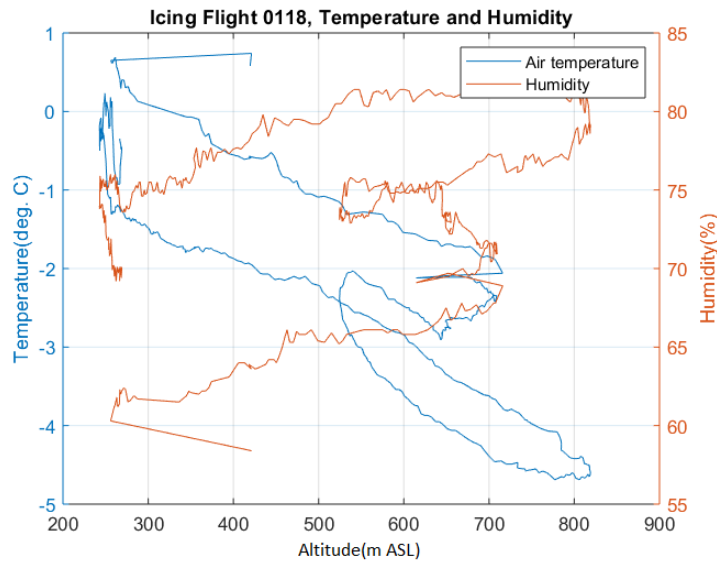
Figure 5.21: Relative humidity and temperature distribution plot for Icing Flight 2.

the wing.

Like Icing Flight 2, this flight was almost entirely in freezing temperatures. Figure 5.24 shows this temperature range on the flight path. This flight was brief due to early onset performance degradation and therefore did not follow the standard circular ascending pattern. It can be seen in Figure 5.25 that there was a moist region that spanned a large altitude. It can be assumed that is was this range that the icing occurred. During this period, the aircraft saw a temperature range of -2.5 °C to -1.0 °C. The skew T plot from the flight can be seen in Figure 5.26

In addition to the standard sensors, an IR surface temperature sensor was flown. This measurement was especially valuable in comparing temperature differential values outputted by the model to those measured in flight. Figure 5.27 shows this measured value compared with air temperature in flight. The pressure is plotted also for referencing stages of the aircraft as it moved from the hangar, runway, then flight. It can be seen that the surface temperature has only a small amount if variation from ambient temperature. This is consistent with the output from the model, and will be further discussed in the next section.

Figure 5.22: Photograph of aircraft wing for Icing Flight 3.
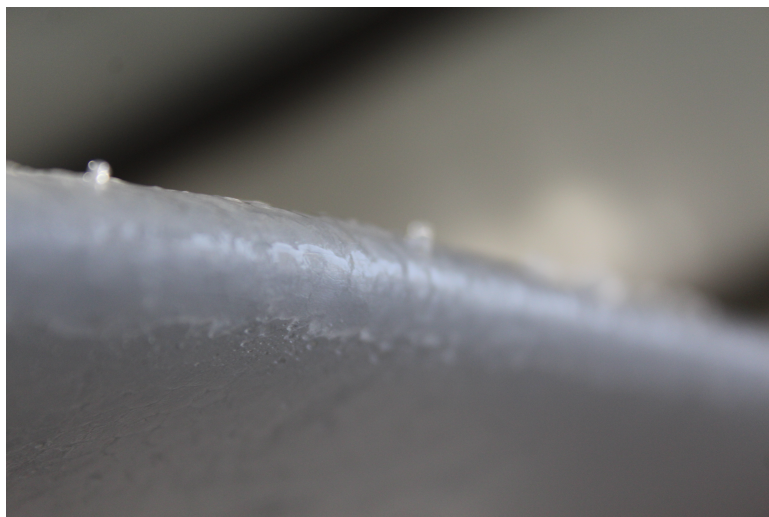
Figure 5.23: Photograph of aircraft wing for Icing Flight 3.
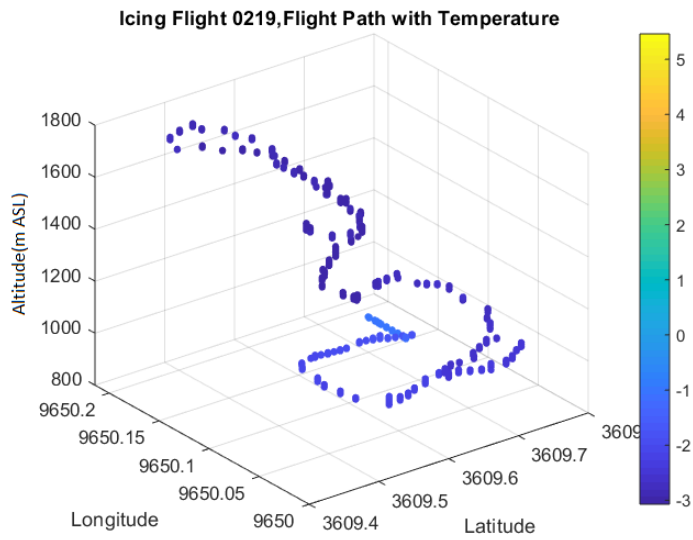
Figure 5.24: Flight path and temperature distribution plot for Icing Flight 3.
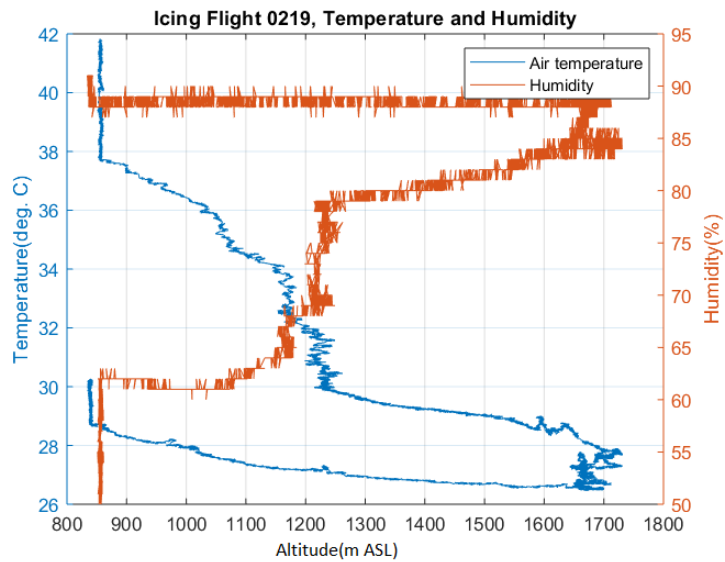
Figure 5.25: Humidity and temperature distribution plot for Icing Flight 3.
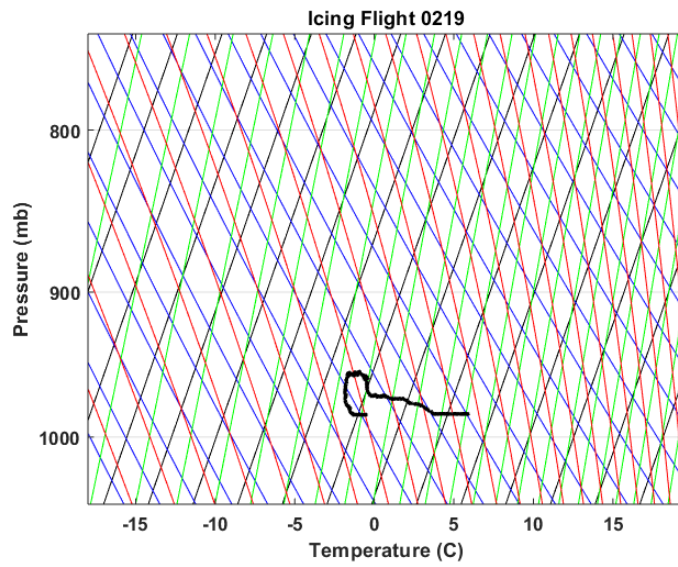
Figure 5.26: Skew T plot for Icing Flight 3.
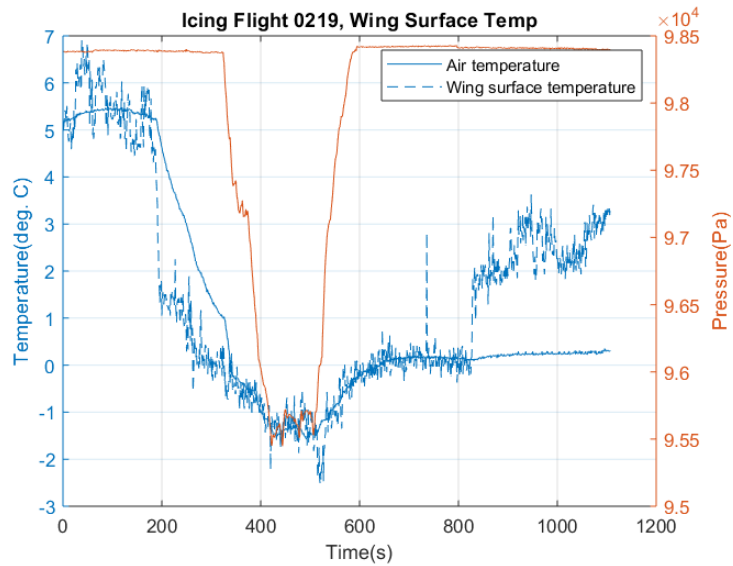
Figure 5.27: Ambient and skin temperature plot for Icing Flight 3.

CHAPTER 6

Numerical Results

Cloud model 1 has been used to explore weather pattern that may have potential for aircraft icing. LEWICE has been explored in its capacity to serve as a reliable software within the study's parameters. In order to gauge an expectation for icing accumulation under low Reynolds numbers, a number of past studies will be reexamined with varied velocities and airfoil size. This includes a pressure study after ice accretion, and icing structure behavioral trends for varying atmospheric conditions and Reynolds numbers. Cylinder ice accretion is major component this and future stages of work and will serve to increase understanding and validate LEWICE results. Most significantly, the cylinder accretion code has simulated results based on droplet trajectories, collection efficiency's, and experimental heat transfer results.

6.1   Ice Accretion Model

In order to further the understanding of the ice accretion at the range of Reynolds numbers, a accretion model was written in MATLab specifically suited to the conditions expected. The following simulations were run with this accretion model with either the dry ice and wet ice heat balance solvers used based on the heat balance results at each angle from stagnation line to 90 degrees. Each case used an icing time of 5 minutes. This was time based on the estimations from the icing possibility analysis in an earlier section. The heat transfer was calculated from the functional relationship of past studies and the power law derived from experimental testing, equation 6.1.
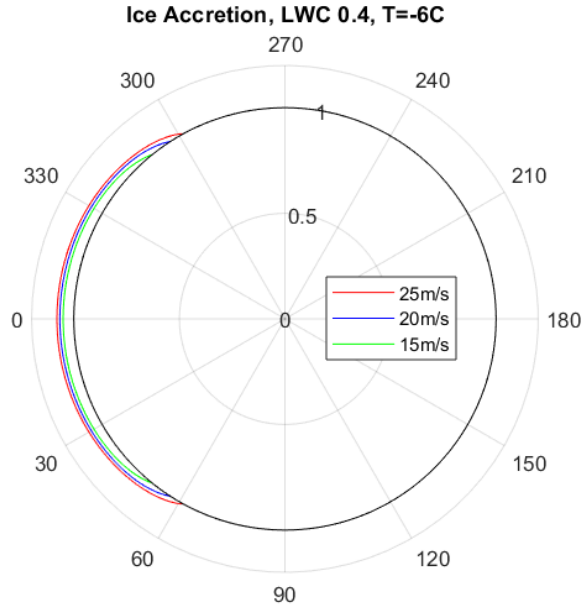
Figure 6.1: Ice accretion simulation with T= -6 °C and LWC= 0.4 g/m^3.

$$Nu(\theta) = Re_c^{0.38}[1 - (\frac{2\theta}{\pi})^3] \tag{6.1}$$

Figures 6.1 and 6.2 give the simulation results from the 0.4 g/m^3 cases at -6 °C and -3 °C respectively. At these two low LWC cases, there is no remaining latent heat in the balance and the accretion is purely dry accretion. With dry ice, the accretion is purely based on the efficency of droplets as they are collected on the face of the cylinder. Thus, there is no difference in the -6°C and the -3°C cases.

In Figure 6.3 the simulations also show dry accretion; this is the case run at -6 °C and a moderate LWC of 0.8 g/m^3. The higher content of water in the air gives a higher ice thickness. The case run at -3 C and g/m^3, Figure 6.4, some wet icing occurs around the stagnation point in the two higher velocity simulations. In the 25 m/s case the runback flows just past 45 degrees and there is a slight dip in thickness at stagnation point. The 20 m/s case shows similar behavior but with a smaller amount of melting. The runback reaches 30 degrees past stagnation point and the thickness change is more difficult to discern. The slow velocity case of 15 m/s remains in the
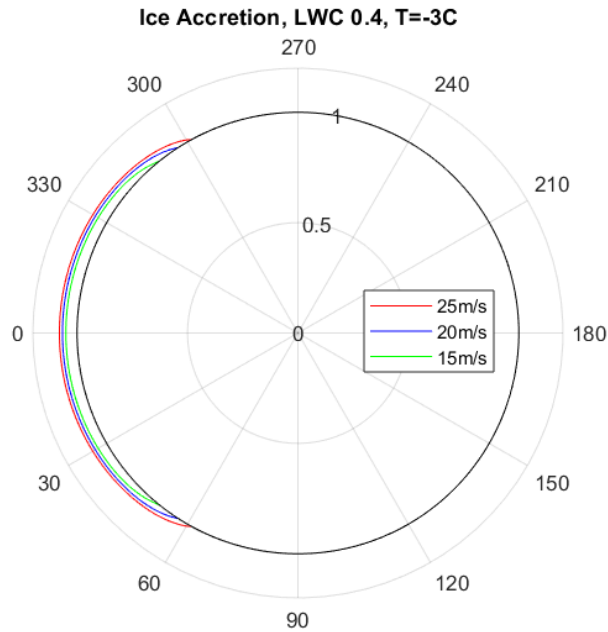
Figure 6.2: Ice accretion simulation with T=-3°C and LWC=0.4 g/m^3.

dry icing regime. The last of aerodynamic heating the the heat balance makes it difficult for melting via latent heat except for flows with high LWC.

Even at the the high LWC simulations run, the colder air temperature of -6 °C allows only dry ice accretion as seen in Figure 6.5. The higher velocity run has the highest ice thickness found in the SUAS simulation set, because there is no thinning around stagnation due to melting. Arguably, the most interesting set of SUAS simulations occur at the 1.2 g/m^3. Each of the cases has some runback and larger ice volumes. The 25m/s case has some rippling around the stagnation point and has runback that almost reaches the maximum collection angle. This rippling is commonly seen in ice accretions due to stages of melting and refreezing in the runback. The 20 m/s and 15 m/s cases also present with noticable runback though less significant thinning at stagnation.

After further inspection of the heat transfer results, some simulations were completed using a function more closely fitted to the heat transfer behavior seen in this
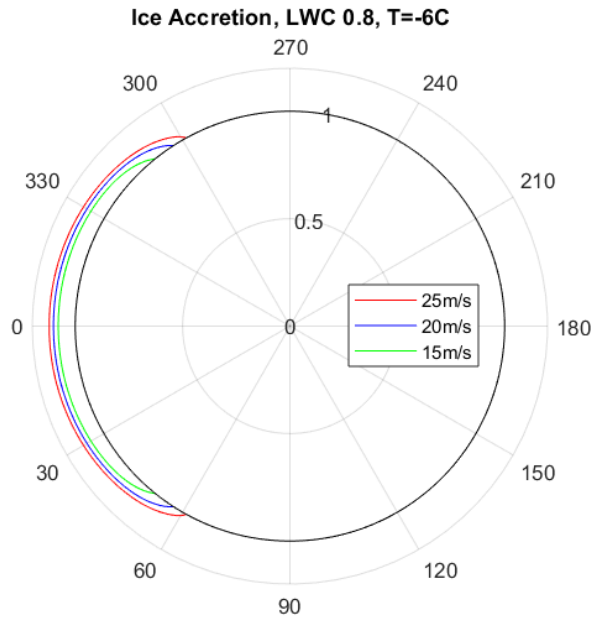
Figure 6.3: Ice accretion simulation with T=-6°C and LWC=0.8 g/m^3.
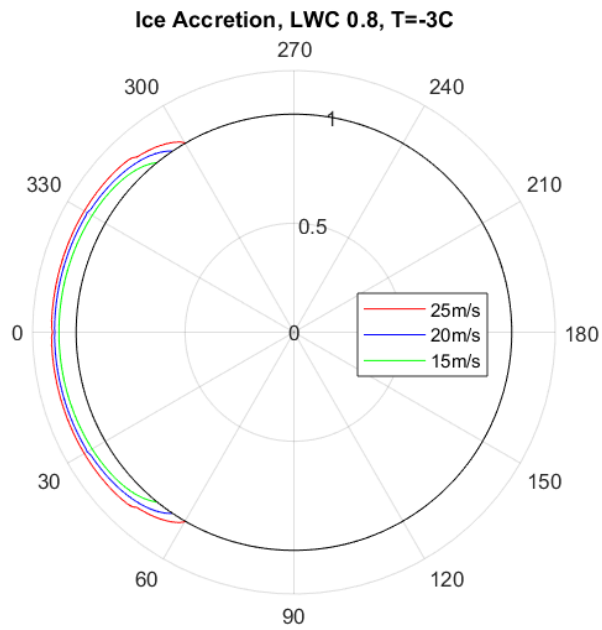
Figure 6.4: Ice accretion simulation with T=-3°C and LWC=0.8 g/m^3.
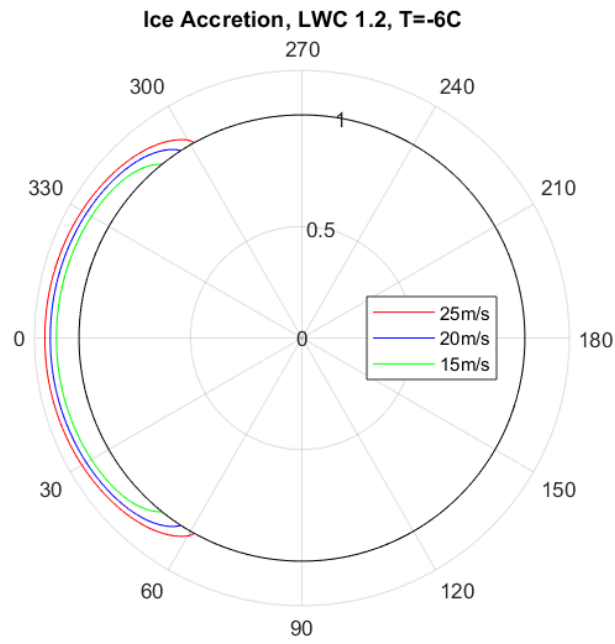
Figure 6.5: Ice accretion simulation with T=-6°C and LWC=1.2 g/m^3.
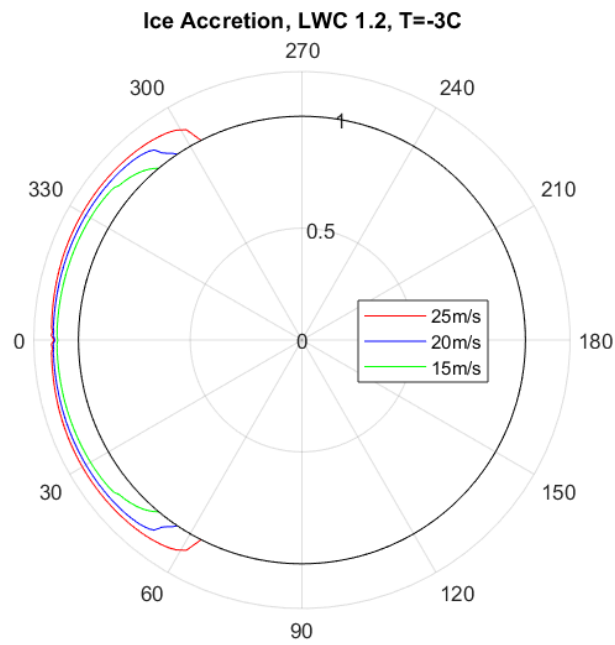
Figure 6.6: Ice accretion simulation with T=-3°C and LWC=1.2 g/m^3.
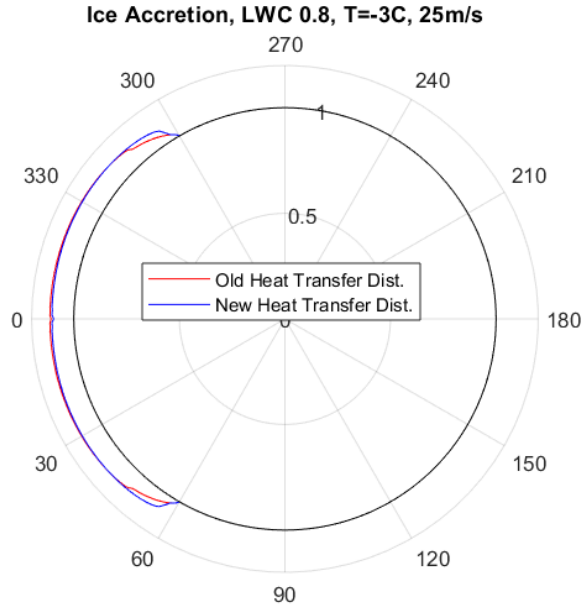
Figure 6.7: Ice accretion simulation with U=25m/s, T=-3°C, and LWC=0.8 g/m^3.

study. Specifically the heat transfer as it changes with angle past stagnation. This function is shown in equation 6.2.

$$Nu(\theta) = 1.6 * Re_c^{0.38} sin(\theta + 60) - 12 \tag{6.2}$$

The simulations that showed noticeable differences with the two different heat transfer equations are shown in Figures 6.7 through 6.10. The dry ice accretions showed very little difference, except for almost negligible runback at stagnation. This was not visible in the plots but was seen in the numerical outputs at the lower speed cases with T=-3 °C, LWC = 0.8 g/m^3.

The two heat transfer distributions did not incur significant volumetric changes but the runback distribution was notably altered. In the simulations with the new heat transfer distribution ice was shown to form past maximum angle of droplet collection. This phenomenon is often seen in experimental cases due to runback with higher travel.
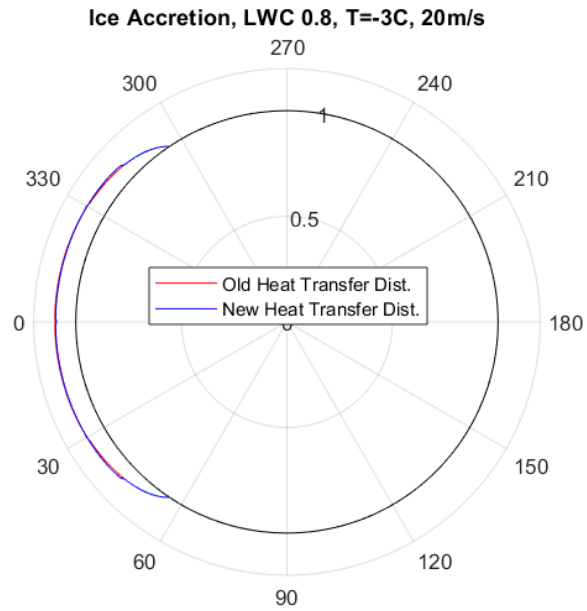
Figure 6.8: Ice accretion simulation with U=20m/s, T=-3°C, and LWC=0.8 g/m^3.
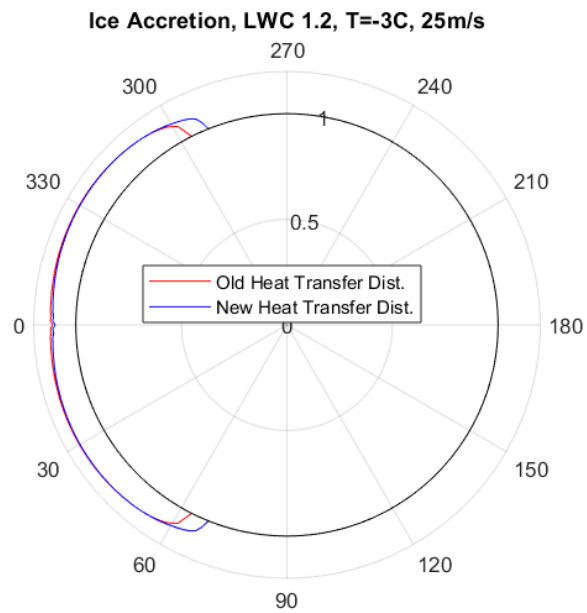
Figure 6.9: Ice accretion simulation with U=25m/s, T=-3°C, and LWC=1.2 g/m^3.
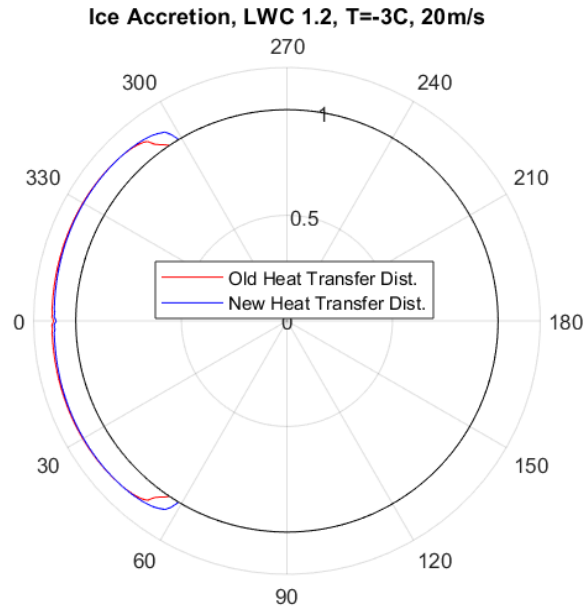
Figure 6.10: Ice accretion simulation with U=20m/s, T=-3°C, and LWC=1.2 g/m^3.

The results in this section are a culmination of the SUAS icing investigations completed. It is helpful to consider these results against the physics explored to create them. The collection efficiency relationship derived carries the bulk of the determination of ice thickness on the face of the cylinder. The nature of the ice that occurs is determined by the heat balance driven by empirical relationships. When this tests were run with past experimental relationships, it was not possible for the simulation to predict wet icing. Past studies were done at significantly higher Reynolds numbers and the higher power law exponents suggested that the energy removed from the system would not allow for any melting at SUAS conditions.

6.2 LEWICE

Though it was determined that LEWICE was unverified at UAS conditions, a foray into LEWICE was completed at the outset of the study as a baseline for icing accretion modeling. LEWICE was used to build an understanding of established ice prediction
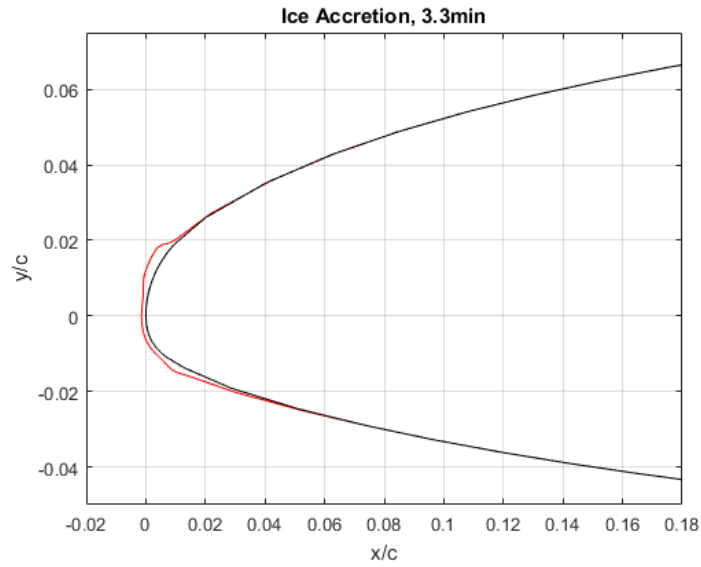
Figure 6.11: LEWICE simulation with ice accretion and Cp plot for a general aviation aircraft after 3.3 minutes.

and resultant aerodynamic consequences.

A brief view of pressure distribution after ice accretion is given using past data. Experimental results were taken from a general aviation aircraft study because it is the closest to SUAS conditions. With only a small amount of ice accretion on the airfoil, LEWICE shows significant changes in the surface pressure. Figure 6.12 shows the accretion after 3.3minutes and the resulting pressure plot, both results pulled directly from LEWICE output; Figure 6.11 shows a more detailed image of the ice. The black line is the airfoil without any icing and the red line shows the outer icing line and changed pressure.

The accretion shape is relatively minor at this step and the geometry could be characterized as streamwise icing or roughness icing. The aerodynamic effect, therefore, should be relatively small without a separation bubble. The geometry was run in XFOIL in order to compare pressure distributions between the two software. Figure 6.13 shows the XFOIL pressure coefficient result compared to the Cp values directly from LEWICE. The XFOIL pressure result is in blue. Since the aerodynamic effect is
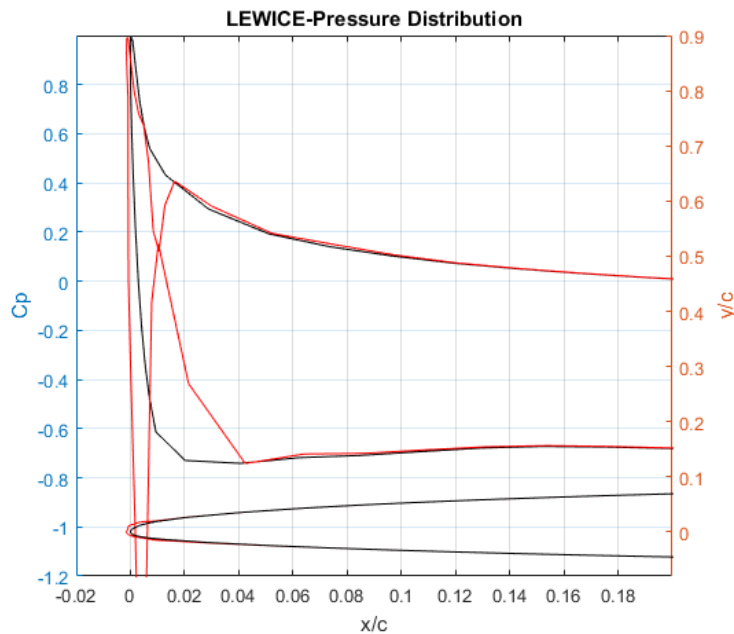
Figure 6.12: LEWICE calculated pressure distribution(red) compared with XFOIL results for airfoil after accretion.

shown to be significant with both software, the icing is closer to moderate roughness icing rather than streamwise icing. However, the XFOIL results in that case are less reliable due to likely leading edge separation.

Figure 6.14 has both the results from the 40s accretion and after 11.5 minutes. This is shown by the green line and has extreme negative pressure spikes pushing back to 0.1 of the chord. At this later time step, the ice accretion has developed into the horn shape. The resultant separation bubble explains the extreme behavior seen in the pressure coefficients. The NASA study for the general aviation conditions does not have an experimental result for pressure coefficients.

Though rime icing is outside the conditions expected for this UAS icing study, NASA conducted a useful study for rime icing that included measured coefficient of pressure values after tunnel experiments with a simulated ice shape at the Ohio State University wind tunnel [2]. The experimental results of the pressure distribution can
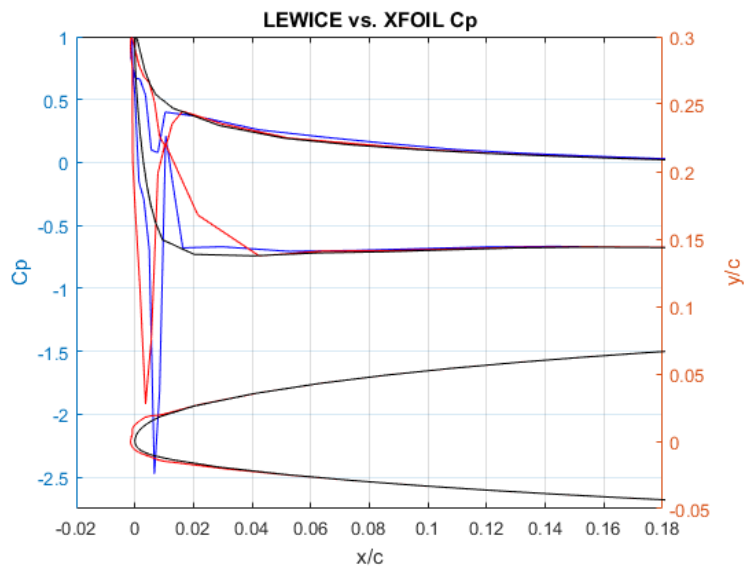
Figure 6.13: LEWICE ice accretion pressure distribution compared to the pressure distribution result from XFOIL for a general aviation aircraft after 3.3 minutes.
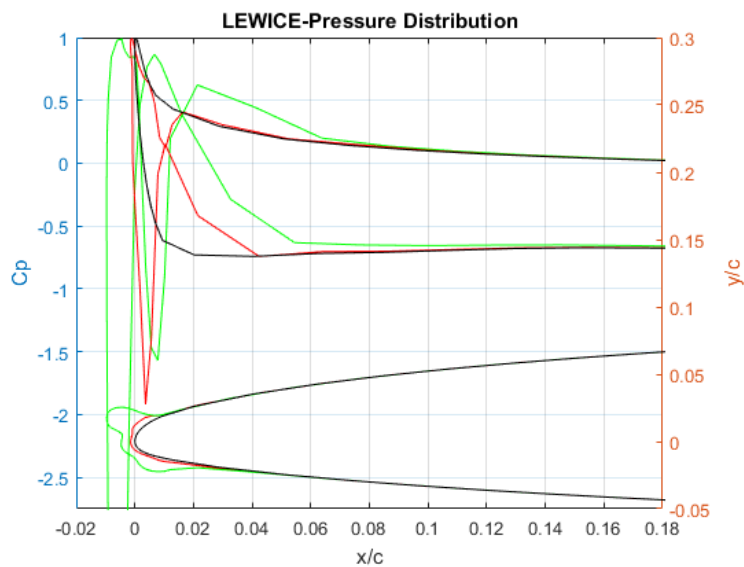
Figure 6.14: LEWICE icing simulation and corresponding pressure distribution for a general aviation after 11.5 minutes.

Table 6.1: Rime Study Experimental Tunnel Conditions[2]

Reynolds Number	3,000,000
Mach Number	0.40
AOA	1 deg
Airfoil	NACA 65A413
Icing time	8 min

Table 6.2: Rime Study LEWICE Icing Conditions

Static Temperature	257 K
Velocity	127.4 m/s
AOA	1 deg
LWC	0.25 g/m3
MVD	15 um
Chord	54.3 cm

support the validity of the Cp behavior predicted in LEWICE. For the experimental tests, NASA used the NACA 65A413 airfoil; for the LEWICE simulations, the similar NACA 64215 airfoil was used. The experimental conditions are shown in table 6.1. The atmospheric conditions resulting in the experimental ice shape were not specified. Fifteen simulations were run while varying temperature, liquid water content (LWC), and median volume diameter (MVD) within rime icing conditions. Table 6.2 shows the simulation with the results that best fit experimental ice shape. Figure 6.15 shows the leading edge of both airfoils with with tunnel ice shape and the LEWICE shape. There are some discrepancies between the two, but they both fall into the streamwise icing category as is expected in rime icing. The thickness of the ice geometry is large enough that a separation bubble may occur, though not as significant a bubble as would occur in horn icing.
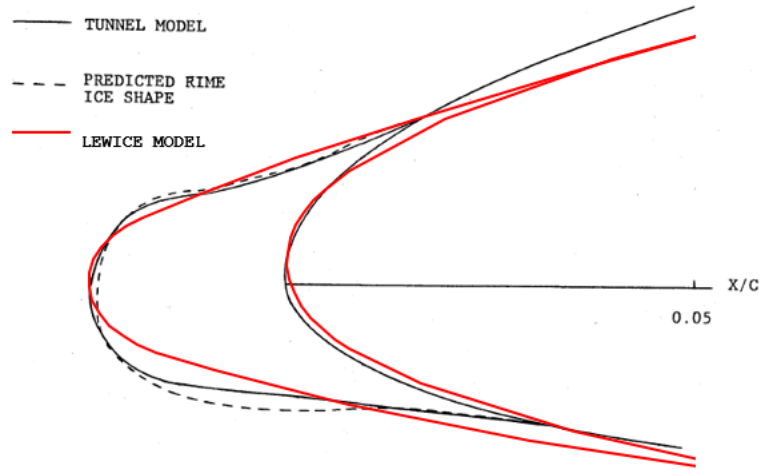
Figure 6.15: LEWICE icing simulation overlain with the experimental airfoil and simulated ice shape.

Figure 6.16 shows the experimental results from the NASA study [2]. The pressure distribution shows changes in Cp for both surfaces after the initial trend from the leading edge. This is also shown in Figure 6.17 in the LEWICE simulation. The pressure behavior matches well enough to support the pressure results from LEWICE at least under streamwise conditions.

6.2.1 Icing Behavioral Trends

The aerodynamic impact can show distinctive patterns and trends in the physics behind the ice shape. Viewing trends in airfoil pressure distribution with icing will give an initial basis for flow as the icing conditions approach UAS icing conditions. The simulations were run with an accretion of time of two minutes and on an airfoil of comparable thickness and camber. The simulations for liquid water content is shown in Figure 6.18.

The simulation results are reasonable, the ice thickness is greater with a higher water content. The simulations for varying temperature are in Figure 6.19. The
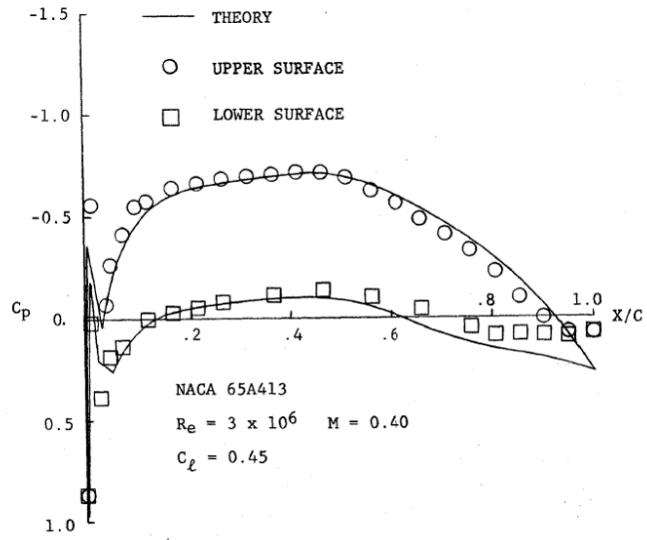
FIGURE 44. THEORETICAL AND EXPERIMENTAL PRESSURE
DISTRIBUTION FOR THE NACA 65A413 AIRFOIL
WITH SIMULATED RIME ICE

Figure 6.16: Experimental results for coefficient of pressure with the added ice shape [2]
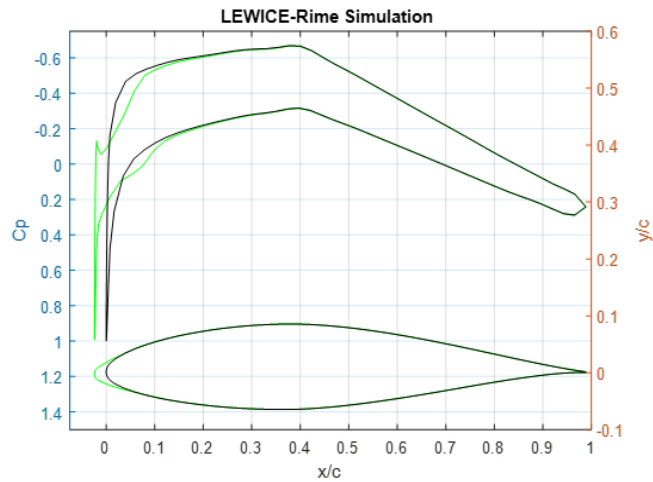
Figure 6.17: LEWICE results for coefficient of pressure and the simulated added ice shape.

84
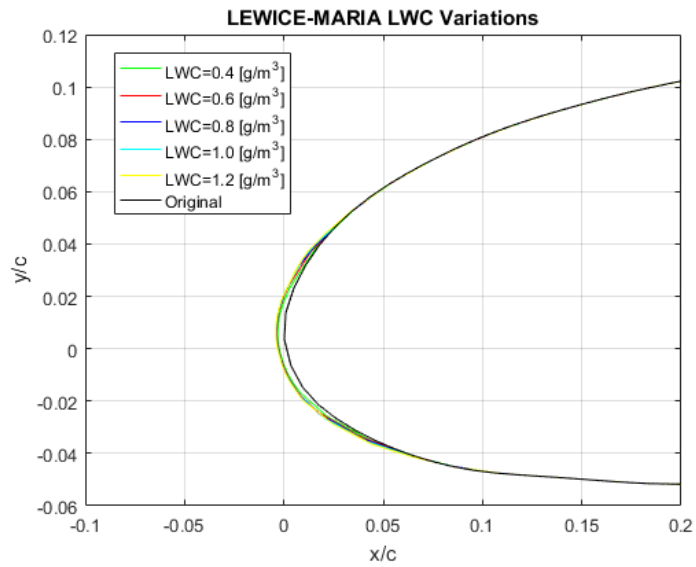
Figure 6.18: Simulation results with variable liquid water content, T=268K.
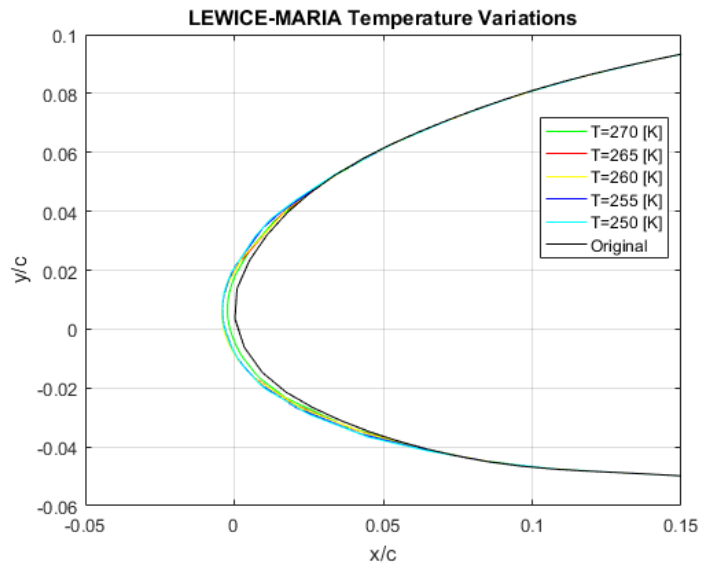
Figure 6.19: Simulation results with variable temperature, LWC=0.54 g/m^3.

increase in thickness is more noticeable as temperature decreases than the simulations where liquid water content were increased. The accretions in these simulations are all representative of streamwise icing. As the study continues, parameter ranges will be broadened to fully characterize the conditions that may result in different types of icing. Extended accretion times as well as SLD droplet simulations should give a larger variety of results.

6.2.2 LEWICE, Accretion Model, and Experimental Comparison

LEWICE was not designed for cylinder flow so it is not expected that the results are reasonable under all icing conditions. However, it is useful to see how LEWICE compares with experimental data because it is part of the scant amount of studies done in the lower spectrum of Weber and Reynolds numbers. The experimental results are a part of the cylinder icing study done with the National Research Council of Canada [3]; the experiments were done in their icing wind tunnel in the Low Temperature Laboratory. A 2.54 cm diameter bakelite cylinder was used. This is much smaller that the airfoils to be used in the UAS simulations, but the results will give a representation of the ability of LEWICE to predict accretion on the small scale. The experimental cases were run at a variety of LWC, temperatures, and velocities. Table 6.3 details the cases which were run in LEWICE and repeated for the accretion model. The experimental data is represented in a comparison plot with the SUAS Accretion code. However, the quality of the image was poor from which experimental data was derived. Thus, there are expected to have some intrinsic errors.

For low volume accretions the LEWICE result matches the experimental case relatively well. Figure 6.20 shows the case with the lowest speed and smallest accretion volume; both the maximum ice thickness and the spread of the ice match well in this case. These results are also predicted well in the accretion model. In the next two cases, Figures 6.21 and 6.22 both show LEWICE results that under predict volume

Table 6.3: National Research Council of Canada icing experiments [3]

Case	Temp. (°C)	Airspeed (m/s)	LWC (g/m^3)
1	-5	30.5 m/s	0.40
2	-5	30.5 m/s	0.78
3	-5	30.5 m/s	1.20
4	-5	61.0 m/s	0.46
5	-5	61.0 m/s	0.78
6	-5	61.0 m/s	1.25
7	-15	30.5 m/s	0.40
8	-15	30.5 m/s	0.82
9	-15	30.5 m/s	1.23
10	-15	61.0 m/s	0.46
11	-15	61.0 m/s	0.77
12	-15	61.0 m/s	1.23
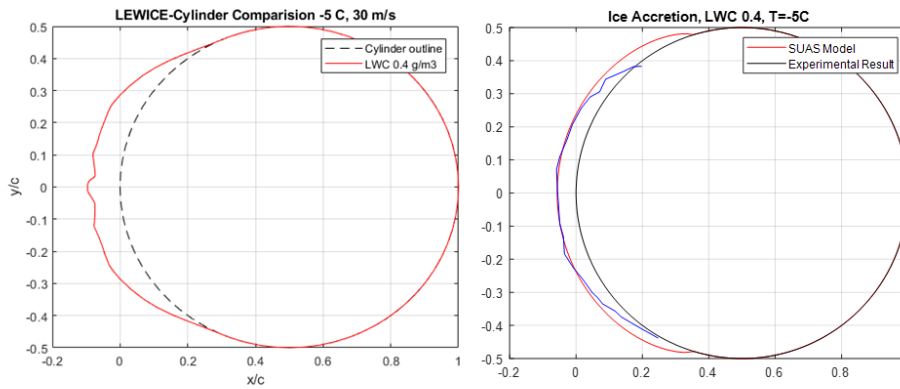
Figure 6.20: Case 1 simulation results compared with experimental case at -5°C, 30 m/s, 0.40 g/m^3 for 5 minutes.

and show an accretion shape much more narrow than the experimental results. This is more likely due to LEWICE's inability to predict flow around the cylinder once ice builds up past a certain degree from the leading edge. The accretion model slightly over-predicts the volume, because it has under-predicted the amount of runback. Figure 6.22 does show a slightly higher volume of ice than 6.21 which is consistent with the experimental results and logic since the LWC is higher. Runback is better predicted in the accretion model though does not flow back past the maximum collection angle as is seen in the experimental result.

Case 4-6 simulations were run for the same set of conditions but at the experimental higher speed. For the first two the accretion shapes look much the same as cases 2 and 3, under-predicting volume and failing to show and accretion towards the top and bottom of the cylinder. In case 6 shown in Figure 6.23, however, the prediction

Figure 6.21: Case 2 simulation results compared with experimental case at -5°C, 30 m/s, 0.78 g/m^3 for 5 minutes.
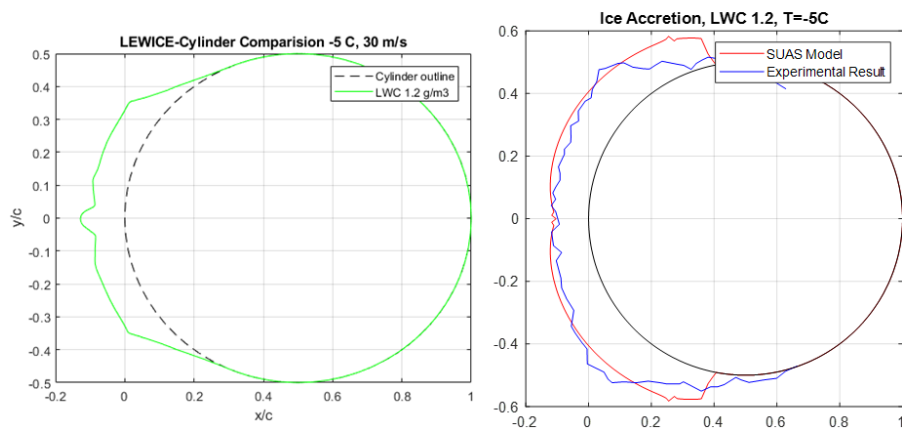
Figure 6.22: Case 3 simulation results compared with experimental case at -5°C, 30 m/s, 1.20 g/m^3 for 5 minutes.
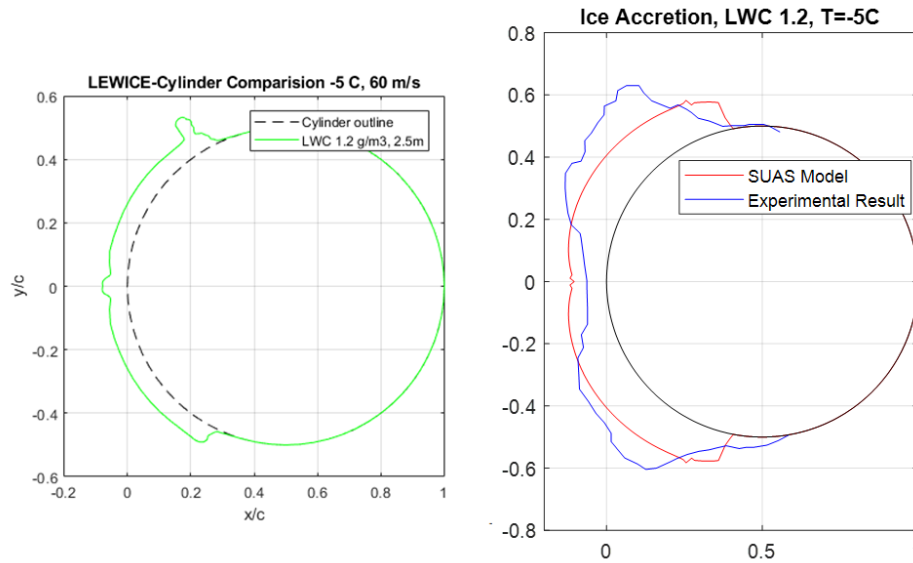
Figure 6.23: Case 6 simulation results compared with experimental case at -5°C, 61 m/s, 0.46 g/m^3 for 4 minutes.

while still off attempts to produce the wedge shape that is seen in the experimental result. While the geometry of the wedge shapes are off, the thinning at stagnation and the distance of the runback are well predicted in the accretion model.

The next set of experimental conditions were done at a colder temperature. This should decrease runback and result in accretion shapes with the volume primarily in front of the cylinder. This behavior is seen in Figure 6.24. Of the set of cases run, the simulations best match the experimental accretion shape with almost perfect matching except a small discrepancy where the ice shape ends.

In the next two cases, 8 and 9, the ice depth up-stream is well predicted but the result fails with respect to the lack of continuity in the outer mold line. If the cylinder is described by angle from the stagnation line, LEWICE has errors in its solution of the accretion past 30 degrees. The accretion code predicts well for case 8
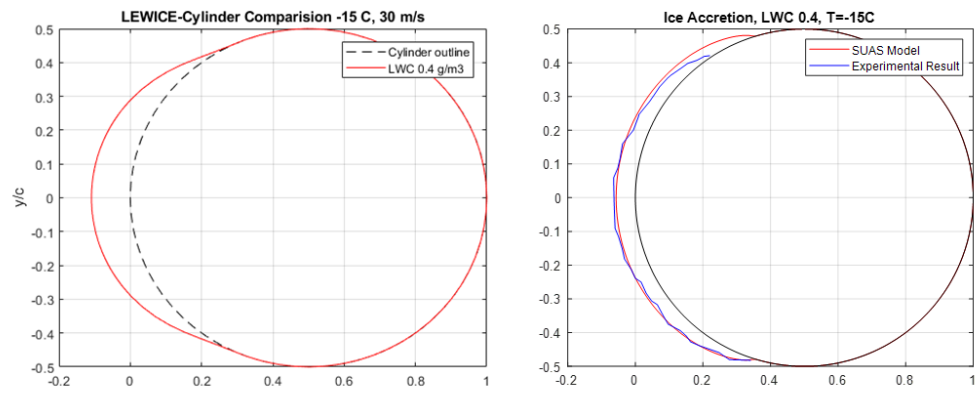
Figure 6.24: Case 7 simulation results compared with experimental case at -15°C, 30 m/s, 0.40 g/m^3 for 5 minutes.
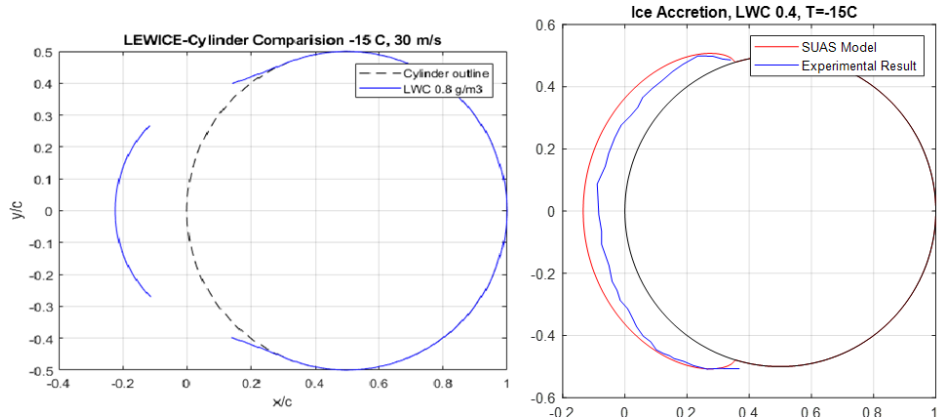
Figure 6.25: Case 8 simulation results compared with experimental case at -15°C, 30 m/s, 0.83 g/m^3 for 5 minutes.

but has significant errors in case 9. This is due to the large accretion volume and the temperature complexities that come from high ice thickness.

Though LEWICE is robust in its ability to adapt to large accretions and a large range of meteorological conditions, it is unsuited for first level SUAS icing investigation. The software is not open and it is difficult to manipulate the physical drivers with the changeable namelist files. Cylinder investigation specifically is unsuited for LEWICE because of the substantial difference in flow.

6.3   Cloud Model 1

CM1 was able to provide an idea of the weather systems that may provide icing conditions and provide likely parameters in those circumstances. Composite reflectivity near the start and end of the simulation is shown in Fig. 6.27 (shown in dBZ). Fol-
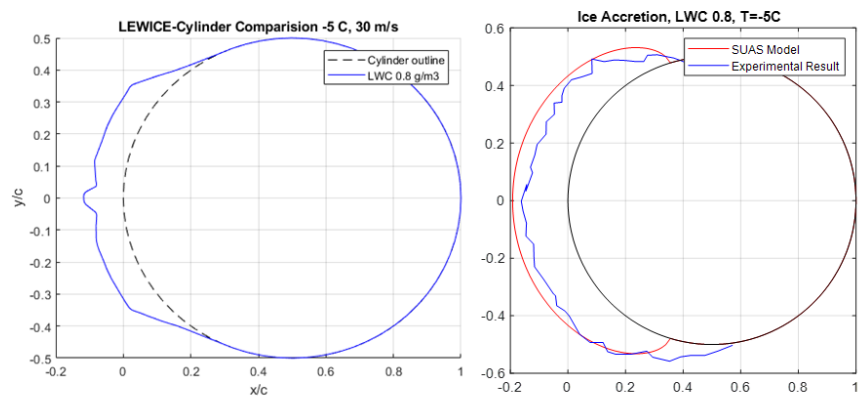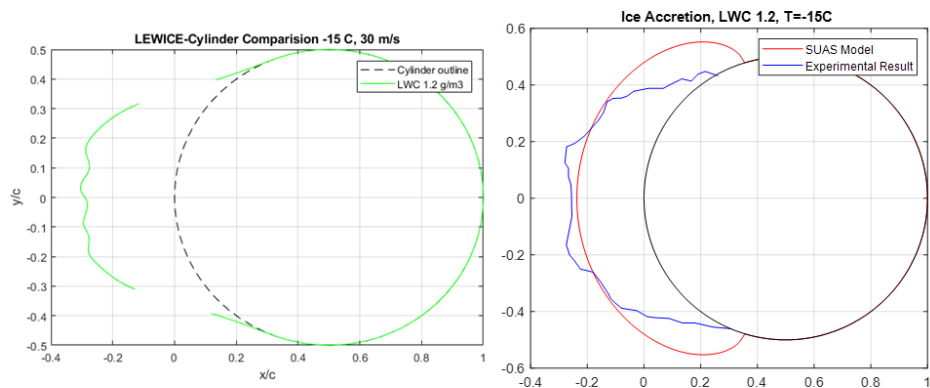
Figure 6.26: Case 9 simulation results compared with experimental case at -15°C, 30 m/s, 1.23 g/m^3 for 5 minutes.
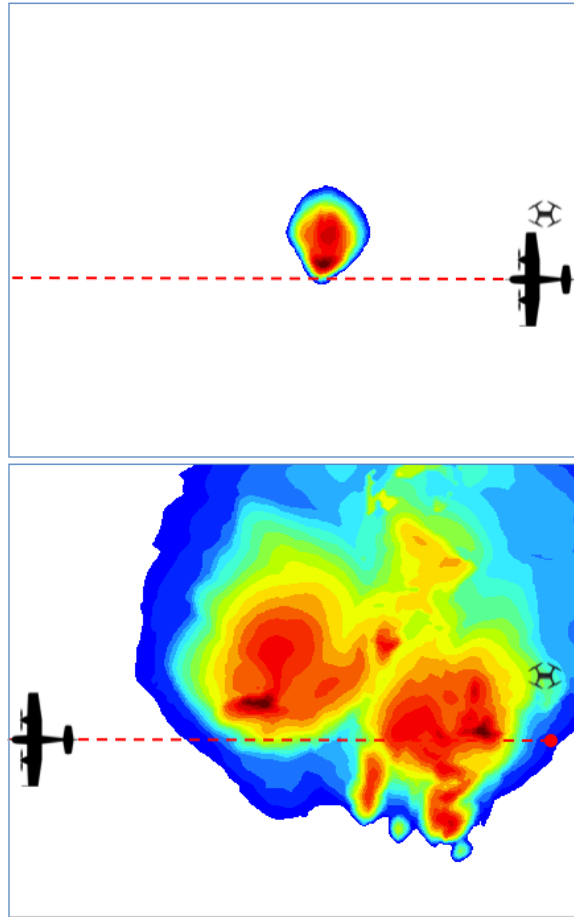
Figure 6.27: Composite reflectivity for CM1 simulation of supercell with location of UAS for the OSSE at the start (left) and end (right) of the simulation, corresponding with the development of the supercell.

lowing the approach of Keeler and Houston, UAS are placed within the simulation domain at specific locations and times to provide the OSSE data, in this case for LEWICE.Notional aircraft with representative paths for a fixed wing (OSU MARIA) and a rotary wing (3DR Solo) are shown with potential representative mission profiles for each.

Liquid water content and temperature are the two parameters that determine the possibility of icing. The temperature most be below zero. Most examples of icing occur when the liquid water content is between 0.2 and 1.8 g/m^3). Figures 6.28 and
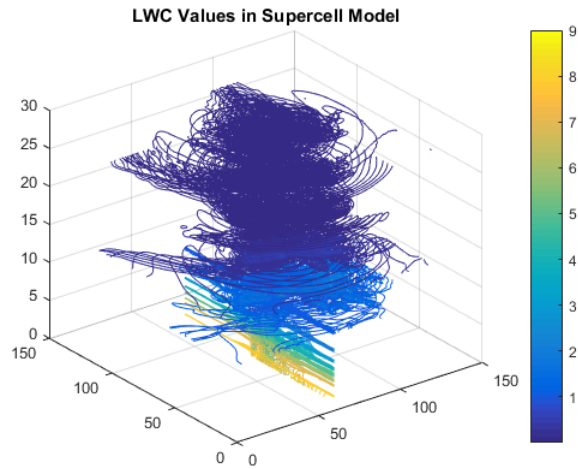
Figure 6.28: Temperature values from the supercell simulation.

6.29 show the distribution of those values is a supercell system.

Icing possibility is isolated by identifying locations where the temperature and LWC are both within the desired spectrum. In order to visualize this easily, the points with positive icing possibilities are added in the horizontal direction. The areas with zero value have no possibility for icing across the entire thickness of the system and the highest values represent the greatest area of icing possibility. Figure 6.30 gives the icing spot analysis for this storm.

It can be seen that the icing area is a thin band within the storm with even smaller spots that have a high chance of icing. More types of weather system would need to be analyzed in order to ascertain the conditions in a true icing weather system.
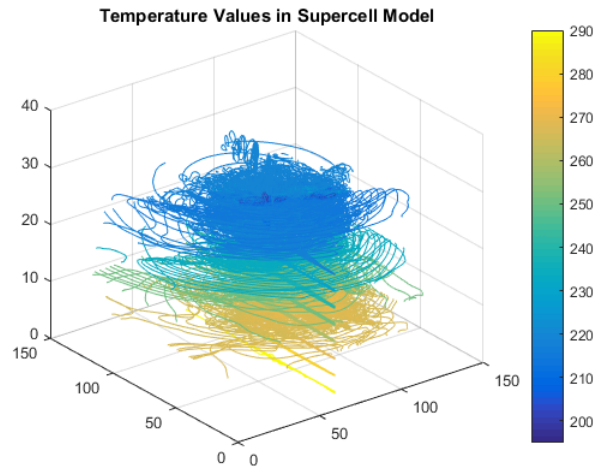
Figure 6.29: Liquid water content values from the supercell simulation.
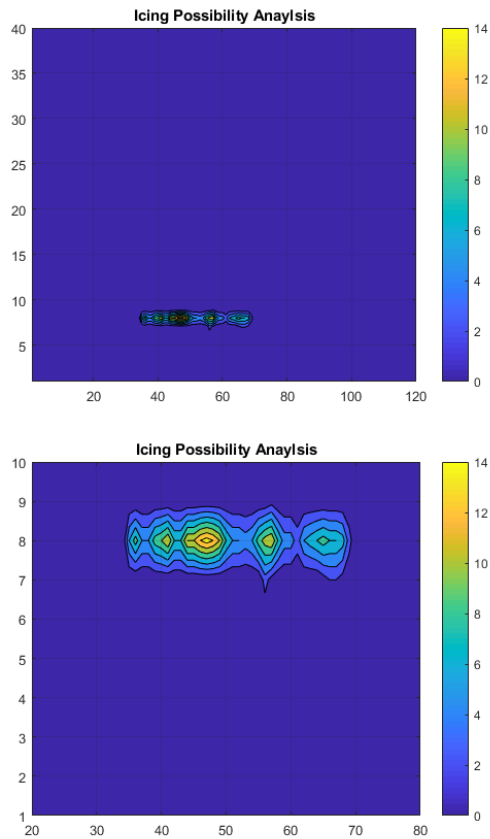
Figure 6.30: Icing spot analysis for the supercell system. Above is overall system; below is closer view of icing area.

CHAPTER 7

Conclusion

In the various experimental and numerical investigations completed, this study has shed significant insight on SUAS icing. Flight test and a atmospheric model were used to look into flight conditions. Experimental heat transfer results were used in conjunction with a numerical ice accretion program written to suit SUAS. Figure 7.1 give on overview of way in which these two elements come together to model the icing problem.

The flight test campaign was able to positively ascertain the presence of ice accretion on small aircraft moving slowing at low altitude, Figure 7.2. Furthermore, one of the flights resulted in an ice geometry driven by a flight flow field. This is important because it demonstrates that low velocity accretion physics is altered by the wing's pressure distribution. The meteorological data gathered during the flight campaign and the CM1 storm system analysis were able to give an expected range of conditions for icing.

The bulk of significant work supported the cylindrical icing accretion program. Extending the work done by Langmuir et al., a method was derived for determining droplet collection efficiency, B_0, as a function of angle past stagnation point. The geometric representation of this function is shown in Figure 7.3; the derivative of y_0 is $B(\theta)$.

A heat flux gauge was built and used to experimentally determine heat transfer behavior in the SUAS Reynolds number range. The resulting model was able to simulate ice accretion for both wet and dry icing conditions; an example is shown in

Figure 7.1: A diagram of the SUAS icing problem and the ways in which it was addressed.

Figure 7.2: Photograph of aircraft wing for Icing Flight 3.
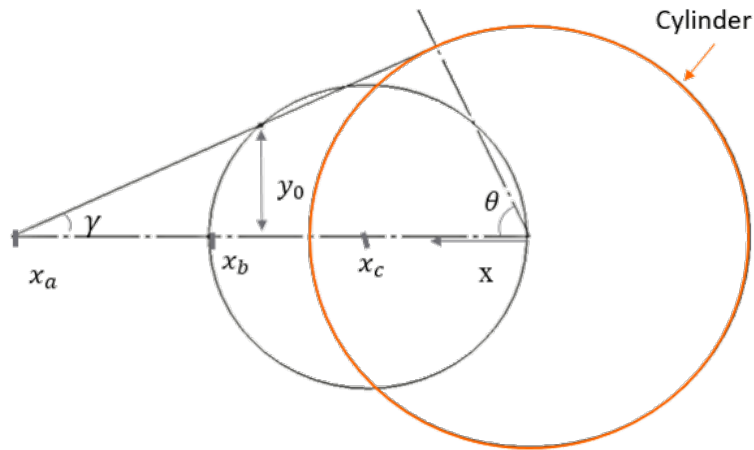
Figure 7.3: System of shapes developed in this study, described by Langmuir et. al. [9].

. Because of some of the simplifications made in the ice thickness calculation, the resultant geometries are expected to have some error. The work done with collection efficiency and heat transfer advocate an accurate determination of the amount wet vs. dry icing on each simulation. The results of the simulations show that in low velocities a low level of accretion is likely. Wet icing will only form at temperatures close to zero and relatively high liquid water contents. Even when wet icing is present notable horn shapes are unlikely.

7.0.1 Future Work

There are some immediate goals for this research that will take place in the next few months. These include extending the heat transfer tests on a vehicle with a robust setup. Additionally, but this apparatus and the wind tunnel will be characterized for free-stream turbulence. Once the environments are fully characterized, tests can be completed under a finer range of angles past stagnation line.

Experimental verification should be undergone for the SUAS simulations presented. An icing wind tunnel would be the first step since SUAS cloud particle
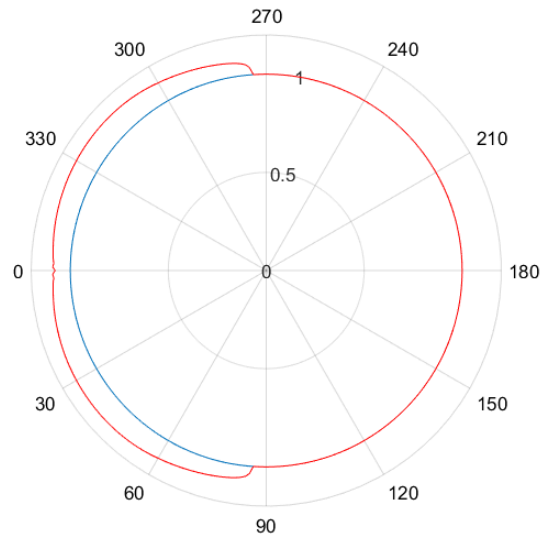
Figure 7.4: Ice accretion example at T=-2 C, 25m/s, and 1.2 g/m^3.

instrumentation is currently unavailable. Such little experimentation has been done at low Reynolds numbers that some physical baseline should be determined. The next step would be model improvement including an improvement on the Messinger heat balance method and an update making the model capable of greater icing times.

BIBLIOGRAPHY

[1] M. P. Brian Berkowitz and B. Namdar, "Experimental ice space and performance characteristics for a multi-element airfoil in the nasa lewis icing research tunnel," *NASA Technical Memorandum 105380*, 1991.

[2] M. B. Bragg, "Rime ice accretion and its effect on airfoil performance," *NASA Contractor Report*, no. 165599, 1982.

[3] J. R. S. E. P. Lozowski and P. F. Hearty, "The icing of an unheated, nonrotation cylinder. part i: A simulation model," *Journal of Climate and Applied Meteorology*, vol. 22, pp. 2063–2074, 1983.

[4] N. Czernkovich, "Understanding in-flight icing," *Transport Canada Aviation Safety Seminar*, 2004.

[5] www.britannica.com/science/weather

[6] M. Belo-Pereira, "Comparison of in-flight aircraft icing algorithms based on ecmwf forecasts," *Meteorological Applications, Royal Meteorological Society*, 2015.

[7] M. K. Politovich, "Aircraft icing caused by large supercooled droplets," *Journal of Applied Meteorology*, vol. 28, pp. 856–868.

[8] M. B. Bragg and A. P. Broeren, "Airfoil ice-accretion aerodynamics simulation," *NASA Technical Memorandum*, no. 214830, 2008.

[9] I. Langmuir and K. Blodgett, "A mathematical investigation of water droplet trajectories," *Army Air Forces Technical Report*, 1946.

[10] G. J. V. Fossen and R. J. Simoneau, "Heat transfer distributions around nominal ice accretion shapes formed on a cylinder in the nasa lewis icing research tunnel," *NASA Technical Memorandum*, no. 83557, 1984.

[11] J. E. Newton and G. J. VanFossen, "Measurement of local convective heat transfer coefficients from a smooth and roughened naca-0012 airfoil: Flight test data," *NASA Technical Memorandum*, no. 100284, 1988.

[12] M. S. Kirby and J. R. John Hansman, "Experimental measurements of heat transfer from an iced surface during artificial and natural cloud icing conditions," *AIAA*, no. 1352, 1986.

[13] E. Achenbach, "The effect of surface roughness on the heat transfer from a circular cylinder to the cross flow of air," *International Journal Heat Mass Transfer*, vol. 20, pp. 359–369, 1976.

[14] D. T. Center, "Nwp workshop on model physics with an emphasis on short-range prediction," *https://dtcenter.org/events/workshops11/mm$_p$hys$_1$1/*.

[15] A. G. for Aerospace Research and Development, "Agard advisory report 334," 1997.

[16] M. K. Politovich, "Response of a research aircraft to icing and evaluation of severity indices," *Journal of Aircraft*, vol. 33, no. 2, pp. 291–297, 1996.

[17] L. A. B. M. B. Bragg, A. P. Broeren, "Iced-airfoil aerodynamics," *Progress in Aerospace Sciences*, vol. 41, pp. 323–362, 2005.

[18] M. G. Potapczuk, "A review of nasa lewis' development plans for computational simulation of aircraft icing," *AIAA*, no. 0243, 1999.

[19] J. R. S. E. P. Lozowski and P. F. Hearty, "The icing of an unheated, nonrotation cylinder. part i: A simulation model," *Journal of Climate and Applied Meteorology*, vol. 22, pp. 2053–2062, 1983.

[20] K. B. R. Jphn Hansman and D. Hazan, "Close-up analysis of aircraft ice accretion," *NASA Technical Memorandum*, no. 105952, 1993.

[21] J. Nihad Dukhan, G. James Van Fossen, K. C. Masiulaniec, and K. J. DeWitt, "Convective heat transfer from castings of ice roughened surfaces in horizontal flight," *NASA Technical Memorandum*, no. 107109, 1995.

[22] T. G. Myers, "Extension to the messinger model for aircraft icing," *AIAA*, vol. 39, no. 2, pp. 211–218, 2001.

[23] A. P. Rothmayer, "Scaling laws for water and ice layers on airfoils," *AIAA*, no. 1217, 2003.

[24] O. d. M. S. Guilherme Araujo Lima da Silva and E. J. G. de Jesus Zerbini, "Integral analyses of the convective heat transfer around ice protected airfoil with non-isothermal surfaces," *International Symposium on Advances in Computational Heat Transfer*, 2008.

[25] M. S. M. M. R. Moore and D. Papageorgiou, "Ice formation within a thin flilm flowing over a flat plate," *Journal of Fluid Mechanics*, vol. 817, pp. 455–489, 2017.

[26] P. T. A. Baumert, S. Bansmer and P. Villedieu, "Experimental and numerical investigations on aircraft icing at mixed phase conditions," *International Journal Heat Mass Transfer*, vol. 123, pp. 957–978, 2018.

[27] G. Poots and P. L. I. Skelton, "Rime- and glaze- ice accretion due to freezing rain falling vertically on a horizontal thermally insulated overhead line conductor," *International Journal of Heat and Fluid Flow*, vol. 13, no. 4, pp. 390–398, 1992.

[28] R. J. H. Jr. and M. S. Kirby, "Comparison of wet and dry growth," *Journal of Thermophysics*, vol. 1, no. 3, pp. 215–221, 1987.

[29] G. H. Bryan and J. M. Fritsch, "A benchmark simulation for moist nonhydrostatic numerical models.," *Monthy Weather Review*, pp. 2917–2928, 2002.

[30] G. H. Bryan and J. M. Fritsh, "A benchmark simulation for moist nonhydrostatic numerical models," *Monthly Weather Review*, vol. 130, pp. 2917–2928, 2002.

[31] J. M. Keeler, "Assimilation of uas-supercell datasets in osse framework," *American Meteorological Society*.

[32] S. Kline and F. Mcclintock, "Describing uncertainties in single-sample experiments," *Mechanical Engineering*, vol. 75, pp. 3–8, 1953.

[33] G. D. Greenwade, "The Comprehensive Tex Archive Network (CTAN)," *TUG-Boat*, vol. 14, no. 3, pp. 342–351, 1993.

[34] J. Harold E. Addy, "Ice accretion and icing effects for modern airfoils," *NASA/TP*, no. 210031, 2000.

[35] B. C. Bernstein and C. L. Bot, "An inferred climatology of icing conditions alot, including supercooled large drops. part ii: Europe, asia, and the globe," *Journal of Applied Meteorology and Climatology*, vol. 48, pp. 1503–1526, 2009.

[36] T. Cebeci and F. Kafyeke, "Aircraft icing," *Annual Review Fluid Mechanics*, vol. 35, pp. 11–21, 2003.

[37] G. A. I. Stewart G. Cober and J. W. Strapp, "Characterizations of aircraft icing environment that include supercooled large drops," *Journal of Applied Meteorology*, vol. 40, pp. 1984–2002, 1984.

[38] H. M. Minghui Diao, George H. Bryan and J. B. Jensen, "Ice nucleation parameterization and relative humidity distribution in idealized squall-line simulations," *Journal of the Atmospheric Sciences*, vol. 74, pp. 2761–2787, 2017.

[39] M. Drela, "Xfoil: An analysis and design system for low reynolds number airfoils," *Low Reynolds Number Aerodynamics. Springer-Veriag Lec. Notes in Eng. 54.*, 1989.

[40] J. Hemmerdinger, "New standard for operating in icing conditions from faa," *Flight International*, p. 14, 2014.

[41] R. Kreeger and W. Wright, "The influence of viscous effects on ice accretion prediction and airfoil performance predictions," *AIAA*, no. 1373, 2005.

[42] P. R. Lowe, "An approximation polynomial for the computation of saturation vapor pressure," *Journal of Applied Meteorology*, vol. 16, pp. 100–103, 1976.

[43] S.-C. W. Michael Papadakis, Arief Rachman and H.-W. Yeong, "Water droplet impingement on simulted glaze, mixed and rime ice accretions," *NASA Technical Memorandum*, no. 213961.

[44] M. K. P. David J. Serke, Andrew L. Reehorst, "Supercooled large drop detection with nasa's icing remote sensing system," *Remote Sensing of Clouds and the Atmosphere XV.*

[45] J.-C. T. M. V. Peter M. Struk, Andy P. Broeren and W. B. Wright, "Fundamental ice crystal accretion physics studies," *NASA Technical Memorandum*, no. 217429, 2012.

[46] K. Szilder and E. P. Lozowski, "Novel two-dimensional modeling approach for aircraft icing," *Journal of Aircraft*, vol. 41, no. 4, pp. 854–861, 2004.

[47] R. M. R. Gregory Thompson and K. Manning, "Explicit forecasts of winter precipitation using an improved bulk microphysics scheme. part i: Description and sensitivity analysis," *Monthly Weather Review*, vol. 132, pp. 519–542, 2004.

APPENDIX A

Appendix

A.1   Rotary Wing Test

Before the SUAS flight campaign was undertaken, minor icing was encountered on a routine atmospheric sounding with a 3DR Solo. The airframe was carrying two iMET XQ sensors and was is estimated to have been in icing conditions for approximately 4 minutes. The icing on the blade is shown in Figure A.1 and flight details are shown in Figure A.2. Unfortunately, it is impossible to know the parameters of the ice accretion since the airframe was only carrying basic atmospheric sensors.

The icing flight campaign resulted in ice accretion in times of measured high humidity and low temperature. The temperatures seen during successful accretion range from -0.5 C to -4.5 C. The humidity levels at the time of accumulation were over 80. Though humidity is not a direct signifier of LWC, the correlation is consistent and logical.

The results of the simulations are shown in Figure A.3. It can be seen that the simulations have a distinct horn structure that was not seen on the actual propeller blade. This could be due to to intrinsic fragility of the horn on such a small airfoil, or it could simply be an error in atmospheric estimation. It is encouraging, however, that the lower surface of the airfoil has a smooth ice structure for each of the runs. This is evidenced in the photograph of the blade with the visible striations in a pattern consistent with a rotating propeller blade. Additionally, the ice appears on the trailing edge instead of under the leading edge. The simulation was run with an alpha of 6 deg. which is the largest stable angle of attack in LEWICE. The propeller
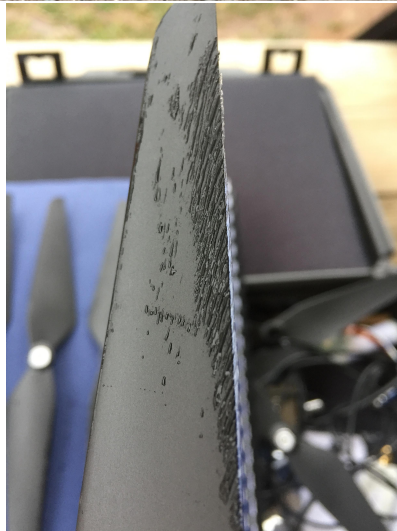
Figure A.1: Ice accretion on a Solo quadcopter with closeup of blade after flight.
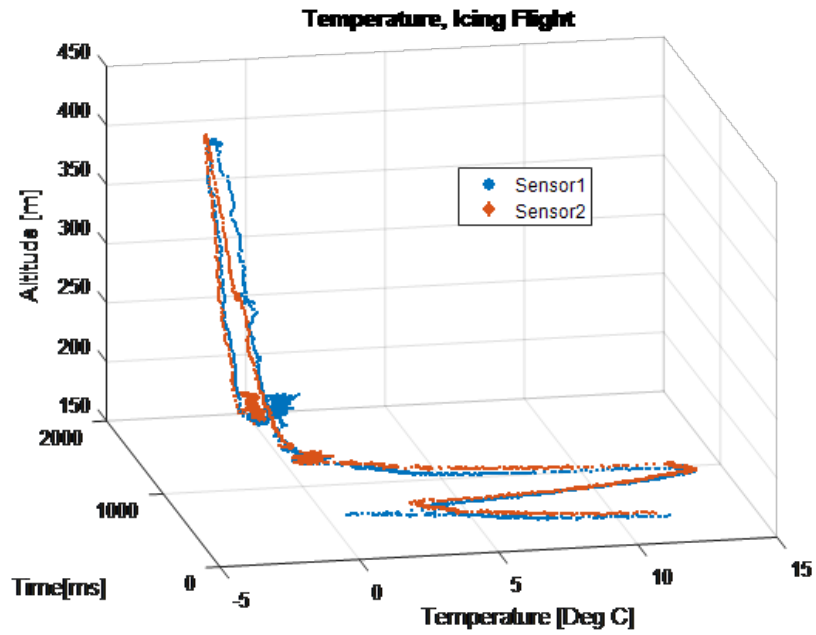
Figure A.2: Altitude and temperature data for the icing flight.
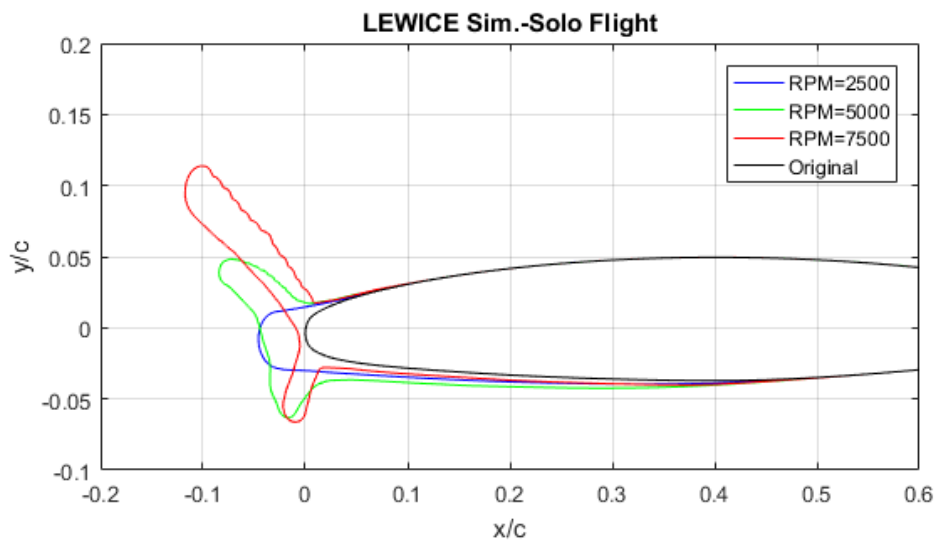
Figure A.3: Simulation representative of the icing encountered the Solo flight.

blade however is at a higher pitch angle that varies extensively throughout the flight, particularly in the climb and descent phases. Since it is not known at which portion of the flight the icing occurred, we can only use the aggregate results for comparison with the simulations.

A.2   Heat Transfer Data Reduction

```
%Seperate and Anaylze Wind Tunnel Runs 04/26/2019

Area=0.625*(0.0254^2);      %sqin to m2

d=2*0.0254;                 %m

mu_a= 1.81*10^-5; %viscosity [kg/(m. s)]

voltage=5;                  %V

current=1.4;                %amps

omega=5.6704*10^-8;         %Wm^-2K_2

Tw=40+273;                  %K

Tt=24+273;                  %K

Ttc=Tt-273;

em=0.5;                     %emisivity

rho_a=1.225; %air density [kg/m^3]

P0=6.3*10^4;  %kg/(ms^2)

Z=6.35*10^-3;

b=Z/4;

r=0.319^0.5;

Qrad=omega*em*Area*(Tw^4-Tt^4);

%% Station 0


%figure

%plot(T1S0)
```

```matlab
t0=NaN(length(timeS0),6);

for i=1:316

    t0(i,:)=datevec(timeS0(i));

end


VS0=[3,7,11,13,15];      %m/s

Re0=NaN(5,1);

Tad=NaN(5,1);

for i=1:5

   Re0(i)=rho_a*(d/2)*VS0(i)/mu_a;

   Ps=P0-0.5*rho_a*(VS0(i)^2);       %static pressure

   C=0.2*(rho_a*VS0(1))^2*(286.91/(1.4*9.81));

   Ts=(-1+(1+4*C*Ttc/(Ps^2)))/(2*C/(Ps^2));

   Tad(i)=Ts+r*(Ttc-Ts);

end


runt0=NaN(5,6);

    for i=1:5

        runt0(i,:)=datevec(rt0(i));

    end


Temp1S0=NaN(23,5);

Temp3S0=NaN(23,5);

Q10=NaN(23,5);

Q30=NaN(23,5);


for j=1:5
```

```
    k=1;
for i=1:length(timeS0)
    if t0(i,4)>=runt0(j,4) && t0(i,5)>=runt0(j,5) && t0(i,6)>=0
        Temp1S0(k,j)=T1S0(i);

        Temp3S0(k,j)=T3S0(i);

        Q10(k,j)=Q1S0(i);

        Q30(k,j)=Q3S0(i);

        if k == 23

            break

        end

        k=k+1;

    end

end
end


sum1=zeros(5,1);

sum3=zeros(5,1);

fr01=NaN(5,1);

fr03=NaN(5,1);

for j=1:5

    for i=1:23

        sum1(j)=sum1(j)+Q10(i,j);

        sum3(j)=sum3(j)+Q30(i,j);

    end

    fr01(j)=sum1(j)*2/58;

    fr03(j)=sum3(j)*2/58;

end
```

```matlab
QEI1=NaN(5,1);

QEI3=NaN(5,1);

h01=NaN(5,1);

h03=NaN(5,1);

Nu01=NaN(5,1);

Nu03=NaN(5,1);

Nu01_R=NaN(5,1);

Nu03_R=NaN(5,1);

h1=NaN(11,5);

h3=NaN(11,5);


for i=1:5

    QEI1(i)=voltage*current*fr01(i);

    QEI3(i)=voltage*current*fr03(i);

end
con=0.370;          %W/mK

Qgap=zeros(5,1);
 for i=1:5

     for j=1:10

         h1t=round(h01(i),2);

    h01(i)=(QEI1(i)-Qrad-Qgap)/(Area*(Tw-Tt));

    h03(i)=(QEI3(i)-Qrad-Qgap)/(Area*(Tw-Tt));

    h3(1,i)=h03(i);

    h1(1,i)=h01(i);

    Nu01(i)=d*h01(i)/con;

    Nu03(i)=d*h03(i)/con;
```

```matlab
    Nu01_R(i)=Nu01(i)/(Re0(i)^0.5);

    Nu03_R(i)=Nu03(i)/(Re0(i)^0.5);

        if h1t ==round( h01(i),2)

            break

        end

        a=0;

        for i=1:10000

            a=a+0.01;

            if round(h03(i)/(1000*con))==round(a*tan(a*Z),2)

                break

            end

        end

    Qgap=2*h01(i)*(40-Tad)*0.0508*(tan(a*Z)*tanh(a*b))/((a^2+x1^2)*Z+x1);

     end

end


-Code repeated for each station 0-10-

%%

Nu_R1=NaN(6,5);

Nu_R3=NaN(11,5);

for j=1:11

    for i=1:5

       % Nu_R1(j,i)=(d*h1(j,i)/con)/(Re0(i)^0.5);

        %Nu_R3(j,i)=(d*h3(j,i)/con)/(Re0(i)^0.5);

        Nu_R3(j,i)=(d*h3(j,i)/con);

    end

end
```

```
 for j=6:11

    for i=1:5

        Nu_R1(j-5,i)=(d*h1(j,i)/con);

       % Nu_R3(j,i)=(d*h3(j,i)/con)/(Re0(i)^0.5);

    end

end

%angle1=[45; 36; 27; 18; 9; 0; 9; 18; 27; 36; 45];

angle1=[ 0; 9; 18; 27; 36; 45];

angle2=[0; 9; 18; 27; 36; 45; 54; 63; 72; 81; 90];


figure

scatter(angle1, Nu_R1(:,3));

hold on

scatter(angle2, Nu_R3(:,3));

hold on

plot(deg,re3)

axis([0 90 0 100])

grid on

title('Nusselt number distribution Re=18,900');

xlabel('Angle from Stagnation Point, deg.')

ylabel('Nusselt Number')

legend('Gage 1','Gage 2')


figure

scatter(angle1, Nu_R1(:,4));

hold on

scatter(angle2, Nu_R3(:,4));
```

```
hold on

plot(deg,re2)

axis([0 90 0 100])

grid on

title('Nusselt number distribution Re=22,300');

xlabel('Angle from Stagnation Point, deg.')

ylabel('Nusselt Number')

legend('Gage 1','Gage 2')


figure

scatter(angle1, Nu_R1(:,5));

hold on

scatter(angle2, Nu_R3(:,5));

hold on

plot(deg,re1)

axis([0 90 0 100])

grid on

title('Nusselt number distribution Re=25,800');

xlabel('Angle from Stagnation Point, deg.')

ylabel('Nusselt Number')

legend('Gage 1','Gage 2')
```

A.3   SUAS Ice Accretion Code

```
%Steady State Heat Balance

%qc+qe+qv+qk+qf+qfr+qw+qwr=0


%% Inputs from dy0 code
```

```matlab
 Theta=71.1604;

 theta_m=Theta*(pi/180);

 Beta_0=0.7653; %fractional collecton efficienct

 Em=0.6471;

 Ej=Em;

 pi=3.1459;

 R=1;
%

 x_a=sec(theta_m);

 x_b=x_a-Beta_0*(x_a-1);

% %from solidworks

% %x_c=0.73464;

 x_c=0.7326;

 R2=x_b-x_c;


%% To get beta

Betai=zeros([90 1]);

angle=zeros([30 1]);

dth=theta_m/30;

i=1;

th=0;


while i<=90


    if th<theta_m

    gamma=atan(sin(th)/(x_a-cos(th)));

    dgamma=((1+(sin(th)/(x_a-cos(th)))^2)^-1)*(cos(th)*(x_a-cos(th))-(sin(th)^2))/((x_
```

```matlab
    %gamma=0;

    phi=pi-gamma-th;

    dphi=-dgamma-1;
l=sqrt(R^2+x_c^2-2*R*x_c*cos(th));

dl=((1/2)*(R^2+x_c^2-2*R*x_c*cos(th))^(-1/2))*(2*R*x_c*sin(th));

phi_1=asin(x_c*sin(th)/l);

dphi_1=((1-((x_c/l)*sin(th))^2)^(-1/2))*x_c*(cos(th)*l-sin(th)*dl)/(l^2);

alfa=asin(l*sin(phi-phi_1)/R2);

dalfa=((1-((1/R2)*l*sin(phi-phi_1))^2)^(-1/2))*(1/R2)*(dl*sin(phi-phi_1)+l*cos(phi-ph

dy_0=R2*cos(alfa-gamma)*(dalfa-dgamma);

    else

        dy_0=0;

    end
%th=th*180/pi;


angle(i)=th*180/pi;

Betai(i)=real(dy_0);

th=th+pi/180;

i=i+1;

end


figure

plot(angle, Betai)

% title('Deposition Efficiency on Cylinder, Case 1 ')

% xlabel('Theta(degrees) from Stagnation Line')

% ylabel('B_{theta}')

% grid
```

```matlab
%%

%Inputs
Dc=0.025;        %cylinder diameter[m]
U=30;        %freestream velocity[m/s]
ta=-4;        %freestream air temperature[Celcius]
tsi=0;        %accretion surface temperature[Celcius]
w=0.8*10^-3;        %liquid water content [kg/m^3]
rho_a=1.225; %air density [kg/m^3]
rho_I=890;        %ice density [kg/m^3]
mw=18.2/28.97;        %ratio of molecular weights of water vapos and dry air[(g/mol)/(g
lv=2.3*10^6;        %latent heat of vaporization [J/kg]
%From Addy 2000, 10 psig
P0=6.3*10^4;  %kg/(ms^2)
P=P0-0.5*rho_a*(U^2);        %static pressure of the freestream
cp=1006;        %specific heat capacity of dry air [J/(kg*K)]
lfs=3.34*10^5;        %latent heat freexing at ts [J/kg]
cw=4.27*(10^3); %average specific heat [J/(kg K)][m^2/s2 K}
ka=0.571;        %thermal conductivity of airstream [W/(mK)]
mu_a= 1.81*10^-5; %viscosity [kg/(m. s)]
Pr=(cp)*mu_a/ka;  %prandtl number
D=24*10^-6;        %mass diffusivity [m^2/s]
Sc=mu_a/(rho_a*D); %Schmidt number
tsr=0;
Re=Dc*rho_a*U/mu_a;


%Betai=Beta_0;
```

```matlab
%ea=(a0+ta*(a1+ta*(a2+ta*(a3+ta*(a4+ta*(a5+a6*ta))))))*10^-2;

ea=610.78*exp(17.625/(ta+243.04));

est=610.78*exp(17.625/(tsi+243.04));


na=ones(90,1);

lth=zeros(30, 1);

ifl=zeros(30,1);


th=0;

tsa(1)=-1;

Rwr=0;

i=0;

n=1;

limit=round(Theta/3,1);

for i=0:90

    nr=n;

if i>0

Rw=Betai(i)*w*U; %droplet mass flux

else

Rw=Beta_0*w*U;

end


%Functions of theta

rc= 0.75+0.25*cos(2*th);   %local recovery factor

%Rw(i+1)=Betai*w*U; %droplet mass flux


%Rwr=(1-nr)*(Rw+Rwr);
```

```matlab
Nu=Re^0.4*(1-(2*th/pi)^3);

h=(ka/Dc)*Nu;    %heat transfer coeff


%Flux Equations


qv=(h*rc*U^2)/(2*cp); %aerodynamic heating
qk=(1/2)*Rw*U^2;  %kinetic energy flux
        %if tsa(i+1)<0
      %  n=1;    %fraction of accreted mass, 1 if ts<0
        qf=Rw*lfs*n;    %latent hf due to freezing impinging water
        qfr=Rwr*lfs*n;
    qc=h*(ta-tsi); %sensible heat flux
    qe=h*((Pr/Sc)^0.63)*(mw*lv/(P*cp))*(ea-est); %transfer of latent heat due to eva
    qw=Rw*cw*(ta-tsi);   %sensible hf btwn accretion and impinging


     if i==0
 syms n
ns=vpasolve(qc+qe+qv+qk+Rw*lfs*n+qw==0, n, [-1 1]);
nf=double(ns);
na(i+1)=nf;
      elseif i==1
  Rwr=(1-na(i))*(Rw+Rwr);
 syms n
ns=vpasolve(qc+qe+qv+qk+Rw*lfs*n+qw+0.5*(Rwr*lfs*n+Rwr*cw*(ta-0))==0, n, [-1 1]);
nf=double(ns);
na(i+1)=nf;
      else
```

```matlab
    Rwr=(1-na(i-1))*(Rw+Rwr);

    syms n

ns=vpasolve(qc+qe+qv+qk+Rw*lfs*n+qw+(Rwr*lfs*n+Rwr*cw*(ta-0))==0, n, [-1 1]);

nf=double(ns);

        if nf > 0 && nf < 0.61

na(i+1)=nf;

        else

            na(i+1)=nf;

            break

        end

         end

end


%Icing Flux

dt=300; %seconds

for i=1:90

        if i>1

        Rw=Betai(i)*w*U; %droplet mass flux

        Rwr=(1-na(i-1))*(Rw+Rwr);

        else

        Rw=Beta_0*w*U;

        Rwr=0;

        end


        ifl(i)=100*na(i)*(Rw+Rwr);


lth(i)=2*ifl(i)*dt/rho_I/(1+(1+4*ifl(i)*dt/(rho_I*Dc))^0.5); %Local icing thickness
```

```
th=th+pi/180;
end


figure(1)
plot(lth)



ang=NaN(360,1);
ang(1)=0;
for i=2:360
ang(i)=ang(i-1)+0.0175;
end
angle=ang*180./(2*pi);
r=ones(size(angle));
xp=r.*cos(ang);
yp=r.*sin(ang);
ri=r;
scale=1;
for j=1:90
    ri(j)=r(j)+lth(j);%.*scale;
    ri(361-j)=r(j)+lth(j);
end
xi=ri.*cos(ang);
yi=ri.*sin(ang);



figure(3)
```

```
polarplot(r)

hold on

polarplot(ri,'-r')

hold off


ax = gca;

d = ax.ThetaDir;

ax.ThetaZeroLocation = 'left';

ax.ThetaColor = 'k';


saveas(gcf,'icing.png')
```

VITA

Alyssa Shearon Avery

Candidate for the Degree of

Doctor of Philosophy

Dissertation: ICE ACCRETION ON SMALL UNMANNED AIRCRAFT

Major Field: Mechanical and Aerospace Engineering

Biographical:

Education:

Completed the requirements for the Doctor of Philosophy in Aerospace Engineering at Oklahoma State University, Stillwater, Oklahoma in July, 2019.

Completed the requirements for the Master of Science in Aerospace Engineering at Oklahoma State University, Stillwater, Oklahoma in May, 2015.

Completed the requirements for the Bachelor of Science in Mechanical and Aerospace Engineering at Oklahoma State University, Stillwater, Oklahoma in May, 2013.

Experience:

Avery, A. and Jacob, J., 2018. *Cylinder Ice Accretion with Application to UAS.* Annual APS Division of Fluids Dynamics Meeting, Bulletin of the American Physical Society, Atlanta, GA.

Avery, A., Bunting, L., and Jacob, J.D. *Icing Measurements with UAS,* AMS Student Conference, Austin, TX, January, 2018.